This electronic thesis or dissertation has been downloaded from the King's Research Portal at https://kclpure.kcl.ac.uk/portal/

Towards Reliable Diffusion MRI of the In Vivo Human Heart

Von Deuster, Constantin Karl Viktor

Awarding institution:
King's College London

The copyright of this thesis rests with the author and no quotation from it or information derived from it may be published without proper acknowledgement.

END USER LICENCE AGREEMENT

This work is licensed under a Creative Commons Attribution-NonCommercial-NoDerivatives 4.0 International licence. https://creativecommons.org/licenses/by-nc-nd/4.0/

You are free to:
- Share: to copy, distribute and transmit the work

Under the following conditions:
- Attribution: You must attribute the work in the manner specified by the author (but not in any way that suggests that they endorse you or your use of the work).
- Non Commercial: You may not use this work for commercial purposes.
- No Derivative Works - You may not alter, transform, or build upon this work.

Any of these conditions can be waived if you receive permission from the author. Your fair dealings and other rights are in no way affected by the above.

Take down policy

If you believe that this document breaches copyright please contact librarypure@kcl.ac.uk providing details, and we will remove access to the work immediately and investigate your claim.

Download date: 06. Nov. 2017

Towards Reliable Diffusion MRI of the *In Vivo* Human Heart

Constantin von Deuster

A dissertation submitted for the degree of
Doctor of Philosophy
of the
University of London

Division of Imaging Sciences and Biomedical Engineering
King's College London, School of Medicine

Abstract

In vivo cardiac diffusion tensor imaging (DTI) is a non-invasive method to map the complex, three-dimensional fibre architecture of the beating heart. It allows the assessment and characterisation of the myocardium and has been employed successfully to image myocardial tissue alterations in a number of relevant diseases. Cardiac diffusion imaging has been primarily performed using stimulated echo based pulse sequences. With recent developments in magnetic resonance hardware and pulse sequence design, spin echo based approaches have become attractive alternatives.

The following work presents a comprehensive comparison of stimulated echo and spin echo based cardiac diffusion imaging approaches. Signal-to-noise ratio (SNR) and diffusion metrics in phantoms and in the *in vivo* human heart are analysed and a modification to previous diffusion encoding schemes is proposed.

In vivo cardiac DTI is implemented and applied to study dynamic fibre reorientation between heart phases in a patient population with dilated cardiomyopathy. Diffusion tensor metrics are compared relative to a healthy control group and correlated to cardiac motion parameters. To address long acquisition times, dual-slice excitation and dedicated image reconstruction are proposed and implemented in a separate study of healthy volunteers.

The impact of microvascular perfusion on the diffusion-weighted signal is investigated in a porcine model of myocardial infarction. The intravoxel incoherent motion (IVIM) model is employed to obtain perfusion metrics which are correlated to dynamic contrast enhanced perfusion measurements. A validation of the IVIM model is performed by comparing *in vivo* IVIM parameters relative to post mortem reference measurements without motion and perfusion effects. Additionally, Bayesian inference is proposed to reduce variability of diffusion and perfusion parameter estimation.

Keywords: myocardial fiber architecture, cardiac diffusion tensor imaging, stimulated echo acquisition mode, spin echo, motion compensation, signal-to-noise ratio, intravoxel-incoherent motion, simultaneous multi-slice imaging, Bayesian inference, myocardial infarction, dilated cardiomyopathy

Table of Contents

List of Figures

List of Tables

Chapter 1

Introduction

1.1 Motivation

According to the World Health Organization (WHO), more than 17 million people died from cardiovascular disease (CVD) in 2012 (1,2). With three in every ten deaths, CVDs are the primary cause of mortality and morbidity in the world which translates into an enormous financial burden to health care services (3). CVDs include diseases of the heart, the vasculature of the brain and the blood vessels. Ischemic heart disease and coronary artery disease were cause of 7.4 million deaths and cerebrovascular disease (e.g. stroke) was responsible for 6.7 million deaths in 2012 (2). Among cardiovascular diseases, the main causes are ischemia, non-ischemic cardiomyopathies and valvular diseases (4). Risk factors promoting the processes related to CVDs are smoking, physical inactivity, unhealthy diet, alcohol, hypertension, diabetes, elevated cholesterol levels, obesity, psychological factors (e.g. stress, depression), chemotherapy, and other risk factors (1).

The WHO report suggests three areas which have to be improved to address CVDs: surveillance and monitoring of epidemics of CVDs, the prevention by reducing risk factors and improved disease management by early detection and treatment (1). Imaging methods such as echocardiography or magnetic resonance imaging (MRI) can be employed for disease surveillance and management. Echocardiography is a non-invasive technique to assess cardiac function, such as ejection fraction, wall motion, flow dynamics and valvular pathology (5). It is widely used in clinical routine, due to its examination time efficiency, portability and low cost. The technique is, however, limited by acoustic window restrictions and operator dependency.

Because of its excellent soft-tissue contrast, MRI is particularly suited for medical imaging of cardiovascular morphology and function. The gold standard for functional imaging of the heart are multi-slice cine images to determine left and right ventricular muscle masses, volumes and ejection fractions. In clinical routine, the structural integrity of myocardial tissue can be characterised by late gadolinium enhancement (LGE) imaging. LGE has been used as a robust qualitative tool to map fibrotic or necrotic tissue -both hallmarks of heart disease- in cardiomyopathies and myocardial infarction. LGE, however, does not provide a parametric characterisation of tissue properties. This shortcoming can be addressed by extra cellular volume (ECV) imaging. ECV measurements use T1 mapping (6) pre- and post- contrast agent administration and a hematocrit depended scaling factor. A good spatial correlation between ECV imaging and myocardial fibrosis or edema was found (7).

However, one out of three patients with CVDs suffers from renal insufficiency requiring a contrast-free alternative for myocardial tissue characterisation (8). Hence, imaging techniques relying on endogenous contrasts are being developed and are receiving increasing attention. Promising contrast-free imaging modalities are native T1 (6,9,10), T1rho (11–13), T2 (14,15) mapping and diffusion-weighted imaging (16–19) (DWI).

DWI relies on the signal attenuation due to self-diffusion of water molecules. Successful *in vivo* measurements in the human heart were first reported by Edelman et al. in 1994 (20). The sequence proposed was an adaption of the Stejskal-Tanner diffusion sequence (21) using the stimulated echo acquisition mode (STEAM) method. Diffusion imaging allows determination of myocardial diffusion parameters including the apparent diffusion coefficient (ADC) and fractional anisotropy (FA) of tissue. A good spatial correlation between increased ADC values and fibrotic tissue identified by LGE was recently shown by Nguyen et al. (16). If diffusion encoding is performed along six or more non-collinear directions, the mean orientation of myofibres per voxel can be determined by diffusion tensor reconstruction. This approach is based on the assumption that the principal eigenvector of the diffusion tensor, i.e. the main diffusion direction, is aligned with the mean fibre orientation. The diffusion tensor model has been validated by a number of studies comparing myocardial fibre architecture derived by DTI and histology (22–26).

By means of cardiac DTI, microstructural remodelling in cardiomyopathies and myocardial infarction was observed: Structural degeneration of myocardium was accompanied with an increase in mean diffusivity and reduction in diffusion anisotropy (27–32). As *in vivo* cardiac DTI allows the non-invasive mapping of three-dimensional cardiac fibre architecture, it has the unique potential to monitor cardiac disease progression and gauge myocardial therapy on a microstructural level. In particular, novel treatment approaches such as stem cell therapy could benefit from *in vivo* cardiac diffusion imaging.

Two sequence designs for *in vivo* cardiac DTI have been established: The primary method is the STEAM technique which spans over two consecutive R-R-intervals with single-shot echo-planar imaging (EPI) readout (20). Alternatively, spin echo (SE) based imaging can be performed if motion-compensated diffusion encoding gradients are employed to address cardiac motion induced signal phase variations. Gamper et al. showed the feasibility of *in vivo* cardiac DTI using velocity-compensated diffusion gradient waveforms (33). Gradient moment nulling up to second and third order were shown thereafter by Stoeck et al. and Welsh et al. (34,35). The image readout is mainly performed by single-shot EPI or balanced steady state free precession imaging (36) in conjunction with diffusion-weighted pre-pulses.

Respiratory and cardiac motion is several magnitudes larger compared to the displacement of diffusing water molecules rendering the diffusion acquisition process very challenging. Hence, breath holding or dedicated navigator gating are necessary for STEAM imaging (37) whereas single-shot SE based DTI can be applied during free breathing. Myocardial strain during diffusion encoding can bias diffusion tensor metrics in STEAM or can cause signal cancellation in SE based imaging. These effects can be mitigated by dedicated myocardial strain correction (38), careful sequence timing (39) or the use of motion-compensated gradient waveforms in combination with high performance gradient systems (34,35). Alternatively, motion induced signal loss can be reduced by multiple signal sampling at different trigger delays and subsequent temporal maximum intensity projection filtering (40). Besides the motion sensitivity, the intrinsic low signal-to-noise ratio (SNR) of *in vivo* cardiac DTI is a major challenge which results in relatively long scan times.

The objectives of the present work are to advance and employ cardiac DTI to study diffusion and perfusion parameters in healthy and diseased hearts. Methods to accelerate image acquisition and to improve diffusion and perfusion parameter estimation are proposed.

1.2 Outline

Chapter 2 provides an introduction of cardiac anatomy, function and dysfunction. The concept of diffusion imaging is given in Chapter 3 including Gaussian and non-Gaussian diffusion models. Systematic challenges of cardiac diffusion imaging are presented in Chapter 4. Potential means to address the limitations of echo planar imaging as imaging readout are outlined. Cardiac diffusion-weighted imaging methods are presented including higher-order motion-compensated SE imaging and the STEAM approach. Chapter 5 compares SNR and diffusion metrics obtained in phantoms and *in vivo* using stimulated and spin echoes. STEAM based diffusion imaging is performed in DCM patients (Chapter 6) and in healthy humans in combination with simultaneous-multi-slice image acceleration (Chapter 7). Perfusion and diffusion parameters are presented for infarcted pig and healthy human hearts, respectively (Chapter 8 & 9). Chapter 10 concludes with a summary of this work and an outlook.

1.3 Contribution of the Thesis

In a first part, SNR and diffusion metrics are compared between STEAM and second-order motion-compensated SE in phantoms and in the *in vivo* human heart. To reduce the effect of microvascular perfusion (41) on diffusion metrics, a new diffusion encoding sampling scheme with optimized use of available gradient strength is proposed. The scan efficiency of free breathing STEAM and SE based acquisition is investigated (Chapter 5).

The second part of the thesis demonstrates an application of the STEAM sequence: Dynamic fibre reorientation between heart phases is presented in a study of dilated cardiomyopathy (DCM) patients. Additional motion parameters including strain and torsion are reported and correlated to DTI results. Structural and functional metrics are compared to age matched controls (Chapter 6). Acceleration of *in vivo* cardiac DTI by a factor of two using simultaneous multi-slice imaging is shown in a volunteer study in Chapter 7.

The third part of this work is attributed to the SE sequence: The impact of perfusion on the diffusion-weighted signal is evaluated in a pig model of myocardial infarction. Results are compared to dynamic contrast enhanced imaging and post mortem reference measurements without motion and perfusion effects (Chapter 8). Least squares fitting for diffusion and perfusion parameter estimation is compared to Bayesian inference in a volunteer study (Chapter 9).

Chapter 2

Cardiac Anatomy

2.1 Macro- and Microscopic Anatomy of the Heart

The heart is a muscular organ pumping blood through the cardiovascular system. Macroscopically, it consists of the left and right ventricles and atria. The left ventricle (LV) supplies the body with oxygenated blood (systemic circulation) and has been in the focus of research including this work. On a microscopic level, the LV consists of myocardial cells (myocytes) which contract upon electrical stimulation propagating from the sinus node. Groups of three or more myocytes surrounded by perimysial weave form myofibres (42). During contraction, a shortening of myocyte length of 13% was found in canine hearts (43) and a myofibre diameter increase of 20% was reported for rats (44). Across several mammalians, a characteristic helical pattern has been

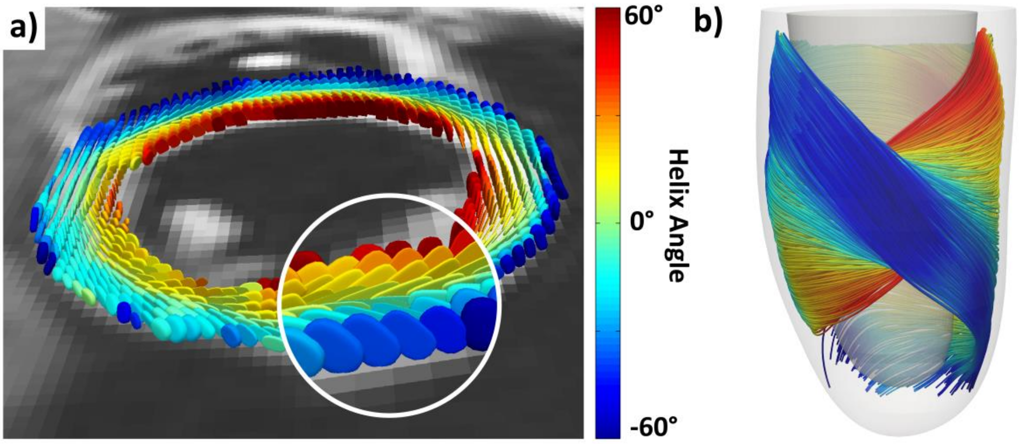

Figure 2.1 *a) Helical structure visualized by superquadric representation of the diffusion tensors in short-axis view orientation. b) 3D fibre pattern of the left ventricle based upon in vivo diffusion tensor imaging (DTI) and fibre tractography. Fibres and tensors are color-coded according to the local helix angle. The images were generated with Paraview (www.paraview.org).*

found as principal fibre orientation at sub-endo and sub-epicardial level (23,24,26,28,45–54) (**Figure 2.1**). The helix angle describes the fibre elevation angle relative to the short-axis plane. From endo- to epicardium, the helix changes continuously from right handed (positive helix angles) to left handed (negative helix angles) orientation. In the mesocardial level, myofibers follow primarily a circumferential orientation. Transmural helix angle variations in healthy human hearts determined by diffusion tensor imaging (DTI) range from -40°/-41° to 65°/66° (*ex vivo*)(18,55) and -18°/-31° to 23°/35° (*in vivo*) (37,56). DTI data confirmed histological observations of the transmural helical course (46), however, microscopically determined helix angles were found to be larger (-72° to 63°) (46,57) compared to *in vivo* DTI measurements. Differences may be attributed to partial voluming effects as the spatial resolution of the *in vivo* measurements is coarser compared to confocal microscopy.

A significant population of myofibers with a non-circumferential alignment was found in the porcine heart using *ex vivo* DTI (53). Helical angles were heterogeneously distributed within the entire left ventricle with crossing fibre paths from endo- to epicardium. This spiral fibre pattern is assumed to equalize and normalize myocardial strain and has been confirmed by other studies using histology and DTI (45,58,59).

Myocytes have a length of 50-150µm and a diameter of 10-20µm, depending on species, age and cardiac location (44,46,60). They are grouped into branching and interconnecting layers forming myocyte bundles and myolaminae. Using electron microscopy in the canine heart, Le Grice et al. (61) found a layer thickness of 48±20µm, which corresponds to three to five myocytes. Myolaminae are arranged as laminar sheets separated by cleavage planes. The term “sheetlets” has been introduced to emphasize the limited spatial extent of myolaminar sheet structures, whereas the term “sheets” might be misinterpreted as global, large scale and continuous planes (61,62).

Myocytes are surrounded by an extensive extracellular collagen matrix which provides structural organization and force transmission (61,63,64). In animal models, *ex vivo* DTI and histology revealed two dominant populations of sheetlet orientation, which were separated by approximately 90° (25,65,66). Similarly, a bimodal sheetlet population was found in the *in vivo* human heart during diastole (38).

2.2 Relationship between Cardiac Function and Structure

During embryonic development, the myocardium progresses from an isotropic, non-coordinated organization of myocytes towards a structured, anisotropic tissue. Myocytes gradually elongate and align themselves resulting in coherent fibre tracts which have been studied by *ex vivo* DTI (67). According to Mekkaoui et al., the development of fibre paths in the human heart is relatively late – approximately 2-3 months upon onset of cardiac contraction (67). Adaption of cardiac microstructure on mechanical load has been shown in chicken embryos: the formation of the characteristic helical fibre pattern is accelerated in case of increased LV pressure load produced by conotruncal banding. Similarly, reduced pressure load results in delayed structural maturation (68). These observations indicate a strong relationship between myocardial structure and the electromechanical function of the heart.

During cardiac contraction, myocardial wall thickens by 30 to 86% (69–71), however less than 50% of it can be explained by an increase in myocyte diameter (72) – the myocyte shortening in canine hearts was found to be only 13% (43). This discrepancy can be explained by sliding and shearing of myolaminae along each other. According to Le Grice et al., cellular rearrangement along myolaminar cleavage planes can account for more than 50% of systolic wall thickening (44,61,72–74). In the *in vivo* human heart, diastolic sheetlet orientation was found to be more longitudinally orientated compared to systole (38).

Besides systolic wall thickening, the left ventricle follows a torsional motion during one cardiac cycle (**Figure 2.2 a)**, **b)**). As viewed from apex to base, the basal slice rotates clockwise and the apex counter-clockwise leading to twist (75) (**Figure 2.2 c)**). Mathematical models have shown that global myofibre orientation with continuous transmural helix angle change results in smooth shortening of myocytes and warrants ventricular torsion (76). This torsion results in shear stress, which tends to “unwind the helix” (77). As a consequence of the ventricular torsion and contraction, the heart shortens by 15-20 % in longitudinal and circumferential direction (69). In the healthy human heart, left ventricular volume shrinks from approximately 142±21ml in diastole

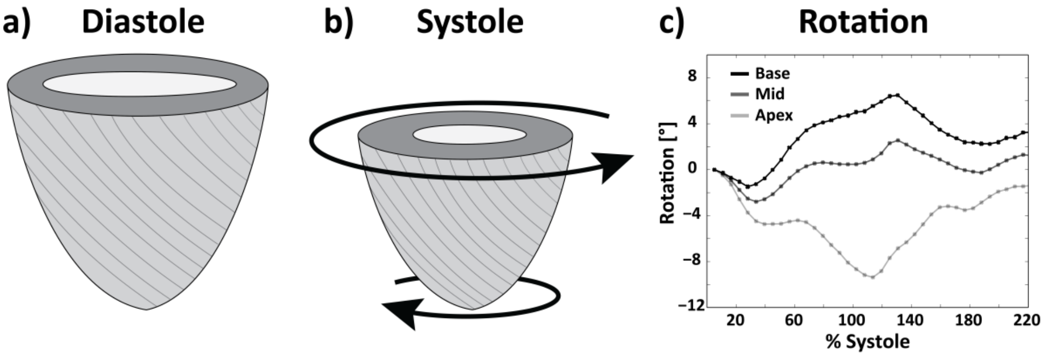

Figure 2.2 a) and b): Left ventricular twist during contraction, c) Rotation time curves at basal, midventricular and apical level. Motion data was derived from 3D tagging imaging.

to 47±10ml in systole (78). The fraction of ejected left ventricular blood per heart beat (ejection fraction) is hence approximately 67±4.6% (78).

Myocardial fibre distribution was found to change during the cardiac cycle. Several studies reported on a longitudinal fibre alignment during cardiac contraction, which is assumed to optimize cardiac pumping efficiency (38,46,79–81). Similarly, radial reorientation of sheets from diastole to systole was observed, providing a potential explanation for the magnitude of radial strain measured *in vivo* (25,74).

During diastole, the left ventricular wall is untwisted by a rapid torsional recoil occurring at the early relaxation phase (82). Stretching along epicardial myofibres and sheet shortening and shear in the endocardial layers have been reported by Ashikaga et al using biplane cineangiography (82). It is assumed that primarily epicardial myofibres and sheet structures between myofibres are the source of restoring forces driving torsional recoil and support early ventricular filling.

Cardiac fibre organization is also a key determinant of cardiac electrophysiology. Directional differences of electrical signal propagation velocities were found in canine myocytes: conduction velocity along fibre direction was found to be up to four times faster than in perpendicular direction (83). Hence, the propagation of excitation waves is aligned with the actual cardiac fibre orientation. In a sheep model of cardiac infarction, the degree of fibre disarray correlated well with a reduction in activation potential (84).

2.3 Cardiac Pathologies

A number of cardiovascular diseases can result in myocardial remodelling. This potentially translates into impaired contractility and hence reduced pumping efficiency, e.g. reduced ejection fraction or cardiac output. *In vivo* cardiac DTI allows for non-invasive assessment of myocardial integrity, while *ex vivo* cardiac DTI is non-destructive in contrast to histological procedures.

In animal models of dilated cardiomyopathy (DCM), an increase in mean diffusivity (MD) and decrease in fractional anisotropy (FA) was found (27). Histological assessment confirmed an increase in extracellular space which poses less restrictions on water diffusion and the degeneration of an organized myofibre structure results in reduced diffusion anisotropy (27,28). Macroscopically, a reduction in circumferential contraction and left ventricular torsion has been found in dilated cardiomyopathy (85,86).

Similarly, disordered fibre patterns have been detected in the *in vivo* human heart with hypertrophic cardiomyopathy (HCM). The degenerate structure was found to correlate with abnormalities in passive and active myocardial function (87), including reduced myocardial strain. The loss of myocardial integrity was quantified by reduced FA, increased MD and increased longitudinal fibre orientation in the septal region (87). According to Ferreira et al., dynamic sheet reorientation between cardiac phases is impaired in hypertrophic regions of the human heart (30). Characteristic systolic sheet orientation was found in regions with hypercontraction in systole and lack of relaxation during diastole (30). In contrast to (87), a comparable helix configuration of HCM relative to healthy controls was measured. Good reproducibly of DTI based results in HCM patients was shown by McGill et al. (29).

Fibrotic tissue, which is a key indicator for heart failure, is clinically evaluated by late gadolinium enhanced (LGE) imaging. Recent studies showed that it can also be characterised and delineated by diffusion-weighted imaging (DWI) in HCM (16) but without requiring the use of contrast agents as in LGE. The diffusion constant of myocardial fibrosis was found to be significantly higher compared to healthy tissue. Apparent diffusion coefficient (ADC) mapping revealed a good spatial correlation with

LGE imaging and extracellular volume (ECV) imaging. ECV in fibrotic region was significantly increased (>30%) compare to non-fibrotic region (ECV: 26±2%) (16) indicating structural remodelling and degeneration of cardiomyocytes (16).

DTI in animal and human subjects (47,48,50,51,54,87) showed that acute ischemia is accompanied by increased MD in myocardial infarction, whereas FA was found to decrease (18,31,51,54). According to Chen et al. reduced diffusion anisotropy in an infarcted rat model correlates well with regions of microscopic fibre disarray (51). Perturbed fibre architecture with nodes of orthogonal myofiber intersection in infarcted hearts was measured using diffusion spectrum imaging (DSI) (48). Regarding chronic infarction, structural remodelling has also been found in the infarct-adjacent and remote zones. Myofibre reorientation towards increased helix angles, i.e. more right handed helix, was observed in humans and sheeps with septal infarcts (31,32,47).

2.4 Cardiac Models

Models describing cardiac architecture remain controversial. For example, the model of a helical ventricular myocardial band (HVMB) which assumes the RV and LV to be formed of a single dissectible muscular band has been debated (88,89). Advances in mathematical cardiac modelling and imaging, however, have meanwhile improved the understanding of cardiac fibre function and architecture. As a result, it has been agreed that the helical band model is not appropriate to describe cardiac anatomy (65,90). It cannot explain the smooth change in ventricular fibre orientation across the myocardium and the discontinuity of myolaminae branching and interconnecting several times between endo- and epicardium (65). Hence, the incomplete and simple idea of HVMB has to be replaced by a concept of myocardium which is organized as continuous and homogeneous three-dimensional myocardial mesh without discrete anatomical and mechanical subcomponents, like tracts or bands (90).

In vivo cardiac DTI is a powerful tool to enhance the understanding of cardiac microstructure. In contrast to histological studies, *in vivo* imaging is non-invasive and depicts cardiac structure under *in vivo* conditions. Additionally, a potential bias in fibre and sheet orientation metrics due to tissue damage by dissection can be avoided.

Chapter 3

Diffusion Imaging

3.1 The Molecular Diffusion Process

The process of free diffusion of water molecules can be modelled as random walk. The probability of finding a particle at position $\vec{x}$ at time t is described by the probability density function $P(\vec{x},t)$. It satisfies the diffusion equation described by Fick (91):

$$\frac{\partial P(\vec{x},t)}{\partial t} = D\nabla^2 P(\vec{x},t) \tag{3.1}$$

with the diffusion constant D. A solution to this partial differential equation with the boundary conditions

$$P(\vec{x},0) = \delta(\vec{x}) \text{ (initial condition)} \tag{3.2}$$

and

$$\int dV P(\vec{x},t) = 1 \text{ (normalization condition)} \tag{3.3}$$

was derived by Einstein (92):

$$P(\vec{x},t) = \frac{1}{\sqrt{4\pi Dt}} e^{-\frac{\vec{x}^2}{4Dt}} \tag{3.4}$$

The root mean squared displacement from the origin to position $\vec{x}$ at time t ($x_{rms}(t)$) is the standard deviation of $\vec{x}(t)$:

$$x_{rms}(t) = \sqrt{\int P(\vec{x},t)x^2 dx - \underbrace{\left(\int P(\vec{x},t)xdx\right)^2}_{=0}} \tag{3.5}$$

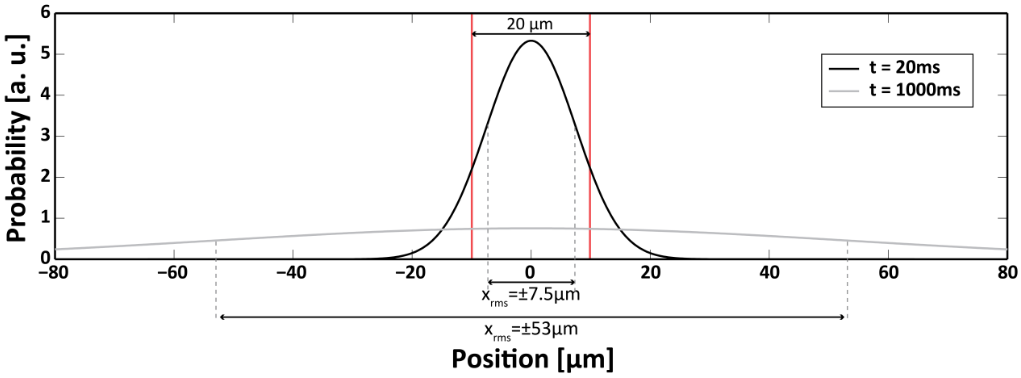

Figure 3.1 Probability density function $P(x,t)$ *for two diffusion encoding times (t=20 and 1000ms). For comparison, the thickness of myocytes (~ 20µm) is indicated by red lines.*

From eq. (3.5) and (3.4) it follows:

$$x_{rms}(t) = \sqrt{6Dt} \text{ (3D)} \qquad (3.6)$$

$$x_{rms}(t) = \sqrt{2Dt} \text{ (1D)} \qquad (3.7)$$

Figure 3.1 depicts $P(x,t)$ for D=1.4x10^{-3}mm^2/s and t=20 and 1000ms in one dimension. The red vertical lines represent the thickness of myocytes (approximately 20µm) (44,60), indicating sizes of potential barriers for freely diffusing water molecules. The probability distribution broadens with diffusion time and the assumption for free diffusion in cardiac tissue is only valid for very short diffusion times t.

3.2 The Stejskal-Tanner Sequence

In 1954, Carr and Purcell demonstrated that the signal intensity in NMR experiments is attenuated by water self-diffusion in the presence of diffusion encoding gradients (93). Based on this work, Stejskal and Tanner extended a spin echo based imaging sequence with pulsed gradients straddling the echo pulse (21) (**Figure 3.2**).

Assuming gradient pulses with gradient strength G and duration δ, the transverse magnetization of water molecules at position x_1 accrues a phase φ_1 during the first gradient pulse:

$$\varphi_1 = \gamma \delta G x_1 \qquad (3.8)$$

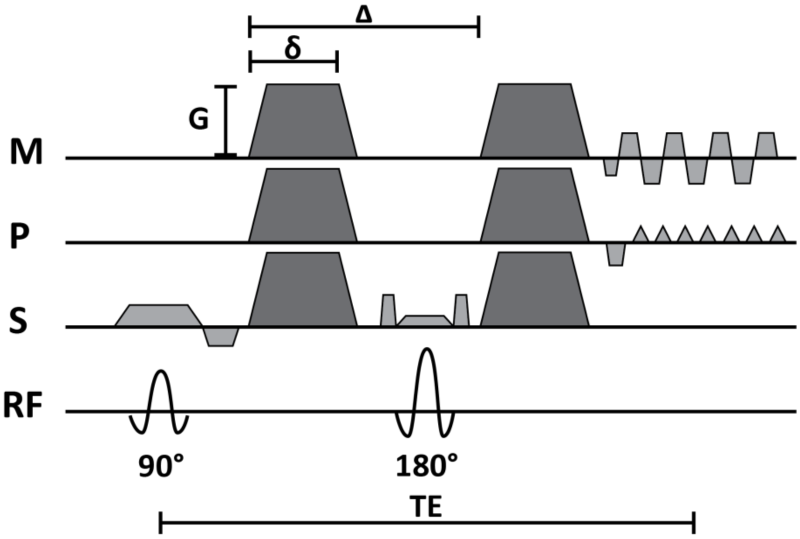

Figure 3.2 Stejskal-Tanner Sequence with single-shot echo planar readout (EPI). Diffusion encoding is performed by unipolar gradients around the refocusing pulse.

with γ as the gyromagnetic ratio $\gamma_{\text{Protons}} = 2 \cdot \pi \cdot 42.6 \frac{MHz}{T}$. If the molecules move during the time Δ to position x_2, the phase accumulation after the second gradient reads:

$$\varphi_2 = \gamma \delta G x_2 \tag{3.9}$$

Hence, the net phase results as:

$$\varphi_2 - \varphi_1 = \gamma \delta G (x_2 - x_1) \tag{3.10}$$

Obviously, net dephasing is zero for static molecules. The measured transverse magnetization $M_\perp$ is the sum over all transverse magnetization vectors with individual phase history within a given voxel. With $\vec{x} = x_2 - x_1$ it follows:

$$M_\perp = M_0 \int P(\vec{x}, \Delta) e^{i\gamma G \delta \vec{x}} d\vec{x} \tag{3.11}$$

Combining Eq. (3.4) and (3.11), the signal $M_\perp$ decays exponentially as function of the gradient parameters and D.

$$\frac{M_\perp}{M_0} = e^{-D(\gamma G \delta)^2 (\Delta - \frac{\delta}{3})} \tag{3.12}$$

3.3 The Diffusion Tensor Model

The dynamics of the nuclear magnetization $\vec{M}$ in the presence of magnetic field $\vec{B}$ is described by the Bloch equations (94). The formula was extended with a diffusion term in 1956 by Torrey (95):

$$\frac{\partial \overrightarrow{M}}{\partial t} = \gamma \overrightarrow{M} \times \vec{B} - \begin{pmatrix} \frac{1}{T2} & 0 & 0 \\ 0 & \frac{1}{T2} & 0 \\ 0 & 0 & \frac{1}{T1} \end{pmatrix} \overrightarrow{M} + \overrightarrow{M_0} \begin{pmatrix} 0 \\ 0 \\ \frac{1}{T1} \end{pmatrix} + \underline{D} \nabla^2 \overrightarrow{M} \tag{3.13}$$

$T1$ and $T2$ are the longitudinal and transversal relaxation times, respectively and $\overrightarrow{M_0}$ the equilibrium magnetization. In the case of diffusion anisotropy, diffusivity needs to be described by a rank 2 tensor $\underline{D}$. For the Stejskal-Tanner experiment, the solution for the transverse magnetization $M_\perp(t)$ reads (41):

$$M_\perp(t) = M_0 \, \mathrm{e}^{-\int_0^t \vec{k}(t')^T \underline{D} \vec{k}(t') dt'} \tag{3.14}$$

with the 0th moment of the diffusion gradient

$$\vec{k}(t') = \gamma \int_0^{t'} \overrightarrow{G}(u) du \tag{3.15}$$

In case of isotropic media, $M_\perp(t)$ at echo formation simplifies to:

$$M_\perp(TE) = M_0 \, \mathrm{e}^{-bD} \tag{3.16}$$

with the gradient waveform dependent diffusion weighting factor b

$$b = \int_0^{TE} \vec{k}(t')^T \vec{k}(t') dt' = \gamma^2 \int_0^{TE} \left(\int_0^{t'} \overrightarrow{G}(u) du \right) \left(\int_0^{t'} \overrightarrow{G}(u) du \right) dt' \tag{3.17}$$

Assuming instantaneous gradient strength, i.e. zero rise time, and neglecting the effect of imaging gradients, the b-value for the pulsed gradient experiment can be calculated as:

$$b = (\gamma G \delta)^2 (\Delta - \frac{\delta}{3}) \tag{3.18}$$

For anisotropic media, eq. (3.14) can be recast to:

$$\ln(\frac{S(b)}{S(0)}) = -\sum_{i=1}^{3} \sum_{j=1}^{3} b_{ij} D_{ij} \tag{3.19}$$

with the diffusion-weighted signal $S(b)$ at TE and the corresponding reference signal without diffusion weighting $S(0)$. b_{ij} and D_{ij} are the components of the b-matrix and diffusion tensor $\underline{D}$, respectively. $\underline{D}$ is represented by a real, symmetric positive definite matrix:

$$\underline{D} = \begin{pmatrix} D_{xx} & D_{xy} & D_{xz} \\ D_{xy} & D_{yy} & D_{yz} \\ D_{xz} & D_{yz} & D_{zz} \end{pmatrix} \tag{3.20}$$

The diagonal terms of $\underline{D}$ correspond to diffusion along the x, y, z axis of the laboratory frame, whereas off-diagonal terms describe the correlation between molecular displacements along orthogonal directions (96).

To calculate the diffusion tensor, at least six diffusion-weighted measurements along non-collinear encoding directions are necessary and one additional $S(0)$ reference image. If more than six directions are encoded, least squares fitting algorithms can be employed to derive $\underline{D}$ (96). Several studies have investigated optimal gradient direction sampling schemes with the conclusion that uniform sampling along three dimensions minimizes the condition number and improves diffusion tensor accuracy (97–100).

The diffusion tensor can be transformed into its eigensystem $(\vec{\mathrm{e}}_1, \vec{\mathrm{e}}_2, \vec{\mathrm{e}}_3)$ with diagonal representation. It can be visualized by a diffusion ellipsoid with the main axis aligned with the orthonormal basis of its eigenvectors (**Figure 3.3**). The boundaries of the ellipsoid are determined by the corresponding eigenvalues $(\lambda_1, \lambda_2, \lambda_3)$ and represent diffusion coefficients along the eigenvectors of $\underline{D}$.

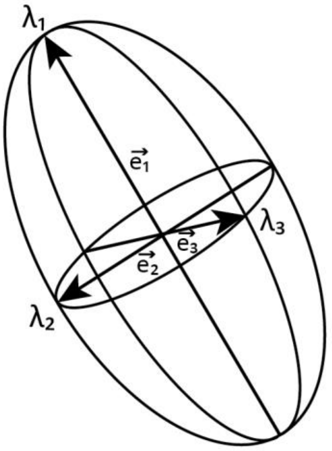

Figure 3.3 *Diffusion tensor representation as diffusion ellipsoid: the principal axis of the ellipsoid form an orthogonal basis which is aligned with the diffusion tensor eigenvectors. The axis lengths are determined by the corresponding eigenvalues.*

For isotropic diffusion $(\lambda_1 = \lambda_2 = \lambda_3)$, the diffusion ellipsoid becomes a sphere, whereas for $(\lambda_1 \gg \lambda_2 \sim \lambda_3)$ the ellipsoid has a cigar shape orientated along its principal eigenvector. In the case of crossing fibers within one voxel, the principal fibre orientations cannot be resolved with a tensor model. In this case, the tensor has a planar shape $(\lambda_1 \sim \lambda_2 \gg \lambda_3)$. Besides the diffusion ellipsoid, superquadric glyphs have been proposed for diffusion tensor representation (101) (**Figure 2.1**). They facilitate visualisation of anisotropic tensor data by enhancing glyph edges, potentially improving diffusion data interpretation.

In case of restricted diffusion, the diffusion constant D is named apparent diffusion constant (ADC). According to eq. (3.16) it can be computed by at least two images with different b-values.

$$ADC = \frac{\log(\mathrm{M}(b_1)/\mathrm{M}(b_2))}{b_2 - b_1} \tag{3.21}$$

For anisotropic diffusion, the ADC depends on the diffusion encoding direction. In this case, the average diffusion constant (“Mean Diffusivity”, MD) can be computed by the mean of the eigenvalues $(\lambda_1, \lambda_2, \lambda_3)$ of the diffusion tensor $\underline{D}$:

$$MD = \frac{\lambda_1 + \lambda_2 + \lambda_3}{3} = \frac{tr(\underline{D})}{3} \tag{3.22}$$

As the trace of a matrix is independent of the choice of basis, any matrix representation of $\underline{D}$ can be used to derive MD. Hence, the MD can be calculated by measuring the ADC along three orthogonal directions (97).

The standard deviation of the diffusion tensor eigenvalues is measured by the fractional anisotropy (FA). It is normalized such that the values of FA range between 0 and 1:

$$FA = \sqrt{\frac{3}{2}} \frac{\sqrt{\sum_{i=1}^{3} (\lambda_i - MD)^2}}{\sqrt{\sum_{i=1}^{3} \lambda_i^{\,2}}} \tag{3.23}$$

In the isotropic case, FA is zero, whereas values above zero indicate diffusion anisotropy, e.g. due to diffusion restrictions.

3.4 Non-Gaussian Diffusion Models

Assuming that the principal fibre orientation is aligned with the first eigenvector, the diffusion tensor model has been established as the most common method to determine fibre orientations in biological tissues. The model, however, fails in regions with multiple fibre orientations, like crossing or bending fibres as only a single fibre orientation can be inferred per imaging voxel. Furthermore, the assumption of a Gaussian diffusion probability density distribution is not fulfilled in the presence of molecular and cellular boundaries, which restrict free diffusion of water molecules. To address these limitations, diffusion encoding schemes with high angular resolution have been developed in combination with fibre orientation reconstruction methods which are independent of diffusion models.

Eq. (3.11) can be rewritten as signal equation $S(\vec{q})$ in vector form using a Fourier integral:

$$S(\vec{q}) = S_0 \int P(\vec{x}, \Delta) e^{i\vec{q}\cdot\vec{x}} d\vec{x} \tag{3.24}$$

with the reciprocal wave vector $\vec{q}$:

$$\vec{q} = \gamma \int_{-\infty}^{\infty} \vec{G}(t)dt \tag{3.25}$$

Hence, the diffusion distribution function $P(\vec{x},\Delta)$ can be obtained by Cartesian sampling of the q-space and Fourier transformation:

$$P(\vec{x},\Delta) = \int \frac{S(\vec{q})}{S_0} e^{-i\vec{q}\cdot\vec{x}} d\vec{q} \tag{3.26}$$

Q-space imaging or diffusion spectrum imaging (DSI)(102) is a six-dimensional acquisition method with three spatial and three q-space dimensions (103).

As the angular fibre orientation is of main interest, the radial information can be integrated via a spherical projection to obtain the diffusion orientation distribution function $ODF(\vec{u})$ with unit vector $\vec{u}$ (102):

$$ODF(\vec{u}) = \int_{0}^{\infty} P(r\vec{u},\Delta) r^2 dr \tag{3.27}$$

Finally, principal fibre orientations for each voxel can be derived from the local maxima of the ODF.

DSI, however, suffers from two practical shortcomings: long acquisition time due to three-dimensional sampling in q-space and the need for strong diffusion encoding gradients to satisfy the Nyquist condition for diffusion in the tissue of interest. Consequently, DSI data quality is limited by low SNR due to long TE.

Instead of sampling the whole q-space, acquisition time can be reduced by sampling on a sphere with high angular resolution (q-ball imaging, HARDI) (104,105). The orientation density function can be approximated via the Funk-Radon transformation as proposed by Tuch et al. (105):

$$ODF(\vec{u}) \approx \int_{\vec{q}\perp\vec{u}} \frac{S(\vec{q})}{S_0} d\vec{q} \tag{3.28}$$

The diffusion probability along a particular direction can be obtained by integration of the diffusion signal along an equator around this direction.

The concept of spherical deconvolution was proposed by Tournier et al. (106) to separate multiple fibre orientations within one voxel. Assuming similar diffusion characteristics for individual fibre bundles, the diffusion signal $S(\theta,\phi)$ can be written as a convolution

$$S(\theta,\phi) = ODF(\theta,\phi) \otimes R(\theta) \tag{3.29}$$

The axially symmetric response function $R(\theta)$ describes the signal attenuation for a single fibre bundle and is weighted by the fibre orientation density function. The ODF can be derived by deconvolving the signal with the response function, which can be approximated from a region with high FA (106). Besides DSI and q-ball imaging, multi-compartment diffusion models have been proposed:

A bi-exponential diffusion tensor model allows imaging of multiple diffusion components, like rapidly and slowly diffusing fractions in intracellular and extracellular spaces (107,108). According to Assaf et al., fiber orientation estimation can be further improved compared to single or dual diffusion tensor imaging, if the diffusion model takes hindrance and restriction effects into account (CHARMED) (109,110).

Diffusion Kurtosis Imaging (DKI) has been proposed to quantify the degree of non-Gaussian water diffusion (111,112). It is described by a rank 4 tensor and can be seen as an extension to the rank 2 diffusion tensor model: the signal equation can be expanded up to 3rd order in b:

$$\ln\left[\frac{S(b)}{S(0)}\right] = -b\sum_{i=1}^{3}\sum_{j=1}^{3} n_i n_j D_{ij} + \frac{1}{6}b^2\left(\frac{1}{3}\sum_{i=1}^{3} D_{ii}\right)^2 \sum_{i=1}^{3}\sum_{j=1}^{3}\sum_{k=1}^{3}\sum_{l=1}^{3} n_i n_j n_k n_l W_{ijkl} + O(b^3) \tag{3.30}$$

with the diffusion and kurtosis tensors D_{ij} and W_{ijkl}, respectively. n_i is the ith component along the direction $\vec{n}$. As the kurtosis tensor is fully symmetric with respect to exchanging indices, 15 components are independent. A useful scalar metric describing diffusional heterogeneity is the diffusional kurtosis $K(t)$:

$$K(t) = \frac{\left[\frac{1}{3}\sum_{i=1}^{3} D_{ii}(t)\right]^2}{\left[\sum_{i=1}^{3}\sum_{j=1}^{3} n_i n_j D_{ij}(t)\right]^2} \sum_{i=1}^{3}\sum_{j=1}^{3}\sum_{k=1}^{3}\sum_{l=1}^{3} n_i n_j n_k n_l W_{ijkl}(t) \tag{3.31}$$

In case of a pure Gaussian diffusion distribution, $K(t)$ vanishes. For a distribution broader than Gaussian, $K(t)$ becomes negative, for a more sharply peaked distribution $K(t)$ is positive. Primary applications to DKI have been neurological studies (111,113), however deviations from Gaussian diffusion distributions have been found in *ex vivo* cardiac tissue recently (114).

The displacement of water molecules during typical diffusion encoding times of spin echo sequences is in the micrometre range. In addition to this microscopic motion, microvascular perfusion in a randomly orientated capillary network can be modelled as pseudo-diffusion on a macroscopic scale leading to additional signal attenuation in the low b-value regime (**Figure 3.4**).

Le Bihan proposed the Intravoxel Incoherent Motion (IVIM) model (115,116), which allows to quantify tissue perfusion. Assuming magnetization dephasing is only due to diffusion and incoherent blood flow in the capillaries, the IVIM theory postulates a bi-exponential signal decay:

$$\frac{S(b)}{S_0} = f \cdot \mathrm{e}^{-bD^*} + (1-f) \cdot \mathrm{e}^{-bD} \tag{3.32}$$

where f is the perfusion fraction, i.e. the fractional volume of capillary blood in the voxel. D and D^* are the diffusion and pseudo-diffusion coefficients, respectively. For free diffusion, the logarithm of signal attenuation is expected to be a straight line as

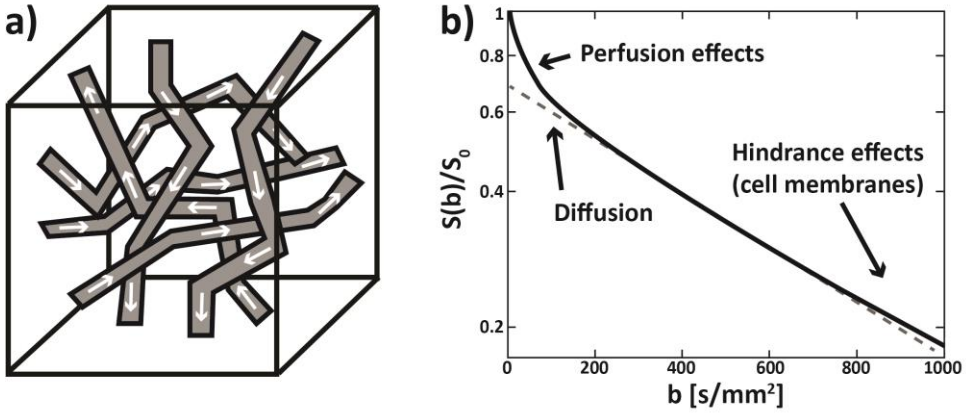

Figure 3.4 *a) Blood circulation in randomly orientated microvasculature, b) logarithmic IVIM signal plot: Perfusion effects cause increased signal decay for low b-values (b<200s/mm^2). For high b-values, interaction with cell membranes leads to additional deviations from mono-exponential signal decay.*

shown in **Figure 3.4 b)**. For small b-values (below $200\mathrm{s/mm^2}$) perfusion effects cause deviations such that the diffusion coefficient appears to be larger if a $b=0\mathrm{s/mm^2}$ is taken as reference. Towards b values of $1000\mathrm{s/mm^2}$ interactions with cell membranes result in non-Gaussian diffusion (117). To account for different relaxation rates of blood and tissue, T1 and T2 relaxation terms can be incorporated in eq. (3.32) as proposed by Lemke at al. (118).

Recently, Moulin et al. (119) and Delattre et al. (120) derived diffusion and perfusion parameters of the *in vivo* human heart using diffusion-weighted imaging. Motion induced signal loss was mitigated by multiple acquisitions during diastole and Principal Component Analysis with Temporal Maximum Intensity Projection PCATMIP (40). Perfusion fraction f was found to be 12±1%, diffusion and pseudo-diffusion constant D and D* were determined to be $1.4\pm0.1\times10^{-3}\mathrm{mm^2/s}$ and $44\pm9\times10^{-3}\mathrm{mm^2/s}$, respectively (119).

Chapter 4

Cardiac Diffusion Imaging

4.1 Systematic Challenges

The primary method for image acquisition in diffusion-weighted imaging is single-shot echo planar imaging (EPI) (**Figure 4.1**). The sequence is one of the fastest MRI sequences, making it particularly suited for cardiac diffusion imaging.

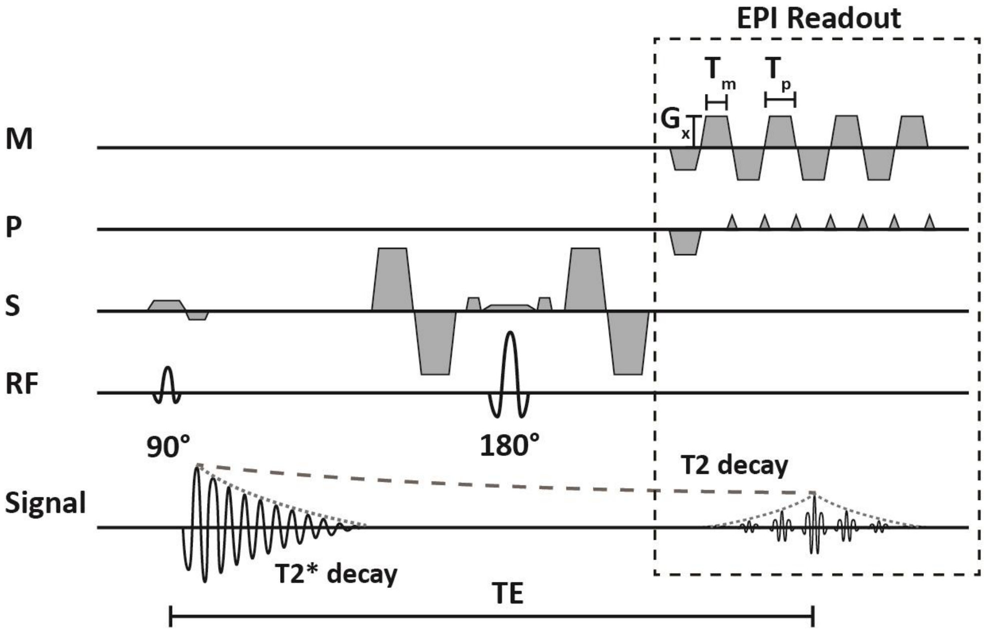

Figure 4.1 Spin echo sequence with echo planar imaging readout. Diffusion weighting is achieved by bipolar diffusion encoding gradients compensating 1^{st} order motion.

As seen in **Figure 4.1**, the global signal envelope follows a T2 decay. EPI suffers from several shortcomings: Due to the echo train, TE is relatively long which leads to low signal-to-noise ratio (SNR) and spatial resolution.

Assuming no ramp-sampling, the acquisition bandwidths along measurement (BW_m) and phase encoding (BW_p) directions are:

$$BW_m = \frac{n_x}{T_m} \tag{4.1}$$

and

$$BW_p = \frac{1}{T_p} \tag{4.2}$$

With the number of sampled data points along x direction (n_x) and the corresponding total sampling time T_m. BW_m is determined by the sampling frequency of the analog-to-digital converter of the acquisition hardware. T_p is the time interval between two adjacent readout profiles (echo spacing):

$$T_p = T_m + \frac{2G_x}{S} \tag{4.3}$$

with the readout gradient strength G_x and the slew rate S. Typical values for BW_m and BW_p for a typical field-of-view (FOV) are 150 kHz and 1 kHz, respectively. For a FOV of 200x100mm^2 and an isotropic voxel size of 2.5x2.5 mm^2, the corresponding pixel bandwidths are 1.9 kHz/pixel and 25 Hz/pixel, respectively. Due to the low bandwidth along the phase encoding direction, EPI is highly sensitive to chemical shift artefacts and magnetic field imperfections.

4.1.1 Magnetic Field Imperfections

Off-resonance effects can cause severe image distortions in EPI. They can be the result of local susceptibility variations, field inhomogeneities, eddy currents with long time constants or concomitant fields.

The effect of local susceptibility variations can be mitigated by careful shim adjustments, e.g. using dedicated first- and second-order shimming based on B_0 field maps (121). Alternatively, B_0 maps can be incorporated into image reconstruction

(122,123) which requires an extension of the signal equation with a field inhomogeneity term $\omega(r)$:

$$s(t) = \int m(\vec{r})c(\vec{r})\,\mathrm{e}^{-i\omega(\vec{r})\cdot(t+TE)}\mathrm{e}^{-i2\pi\vec{k}(t)\vec{r}}\,d\vec{r} \qquad (4.4)$$

$m(\vec{r})$ is the transverse magnetization and $c(\vec{r})$ the complex coil sensitivity. Eq (4.4) can be iteratively solved for $m(\vec{r})$ using the conjugate gradient algorithm as shown by Sutton et al. (123). The proposed method has been used for geometric distortion correction in cardiac diffusion imaging as shown by Harmer et al. (124). Particularly in the vicinity of the posterior vein, signal dropouts or image distortions are a common challenge as seen in **Figure 4.2**. Upon off-resonance correction, the left ventricle has a more physiological shape compared to the original, distorted myocardium. This translates into an improved coverage of diffusion tensors in the infero-lateral region.

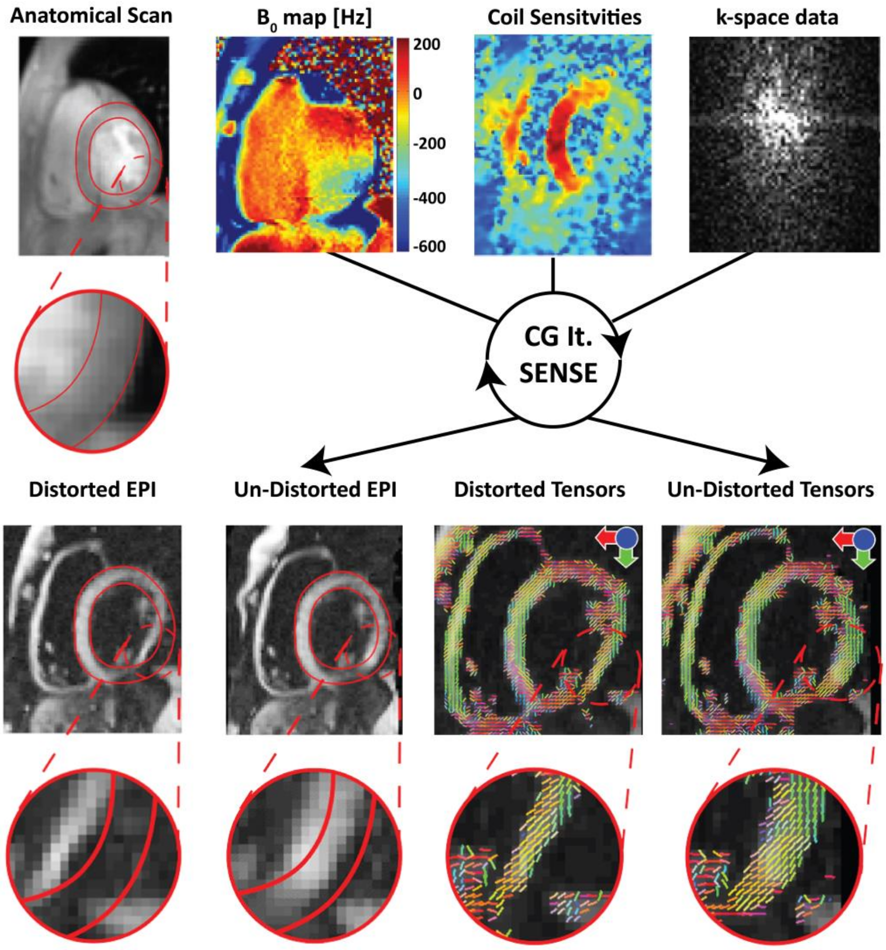

Figure 4.2 *B_0 field maps can be incorporated in image reconstruction using a conjugate gradient iterative SENSE algorithm. Upon off-resonance correction, left ventricular shape follows a more anatomical curvature compared to the distorted case.*

Alternatively, image distortions can be mitigated by reducing the echo train length, e.g. using k-space subsampling and parallel imaging (e.g. SENSE, GRAPPA, (125,126)) or multi-shot imaging (127,128).

4.1.2 Eddy Currents

According to Faraday's law, switching magnetic fields cause eddy-currents in conductive structures of the MR hardware. These currents depend on the applied diffusion-encoding strength and direction and induce temporally shifted magnetic fields counteracting the proposed gradient waveforms. In case of single-shot EPI, this leads to inconsistent k-space trajectories and misaligned diffusion-weighted images. Other artefacts due to eddy-current induced phase changes during image readout are ghosting, bulk object shifts, deformations and signal dropout (122,129). Possible means to reduce these effects are shielded gradient coils (130), gradient pre-emphasis (131) or twice refocused sequence designs (132,133).

Alternatively, eddy-current induced fields can be measured by NMR field probes. The spatiotemporal evolution of the phase (up to 3rd spatial order) can be assessed by a dynamic field camera consisting of 16 NMR probes (134). Applications of this approach have been shown in diffusion and phase contrast imaging (129,135,136). During a separate calibration scan, the phase evolution of the probes is measured and incorporated in the reconstruction algorithms to correct for temporal and higher-order spatial effects. The phase $\Phi(\vec{r},t)$ can be expanded in a spherical harmonic basis:

$$\Phi(\vec{r},t)=\sum_{l=0}^{15}k_l(t)h_l(\vec{\mathrm{r}})+\omega_{ref}(\vec{r})t \tag{4.5}$$

with the set of spherical harmonics basis functions $h_l(\vec{r})$ as in Table 1 of (134). As described in (134), the coefficients $k_l(t)$ can be derived from the measured probe phases. The off-resonance contribution at the reference point at position $\vec{r}$ is $\omega_{ref}(\vec{r})$.

The phase evolution in a spin echo diffusion imaging sequence using uni- and bipolar gradients was characterised in a phantom study by Chan et al. (129). **Figure 4.3** demonstrates the feasibility of phase correction in a structured isotropic phantom. The intensity plots along the vertical blue line for various diffusion encoding directions are

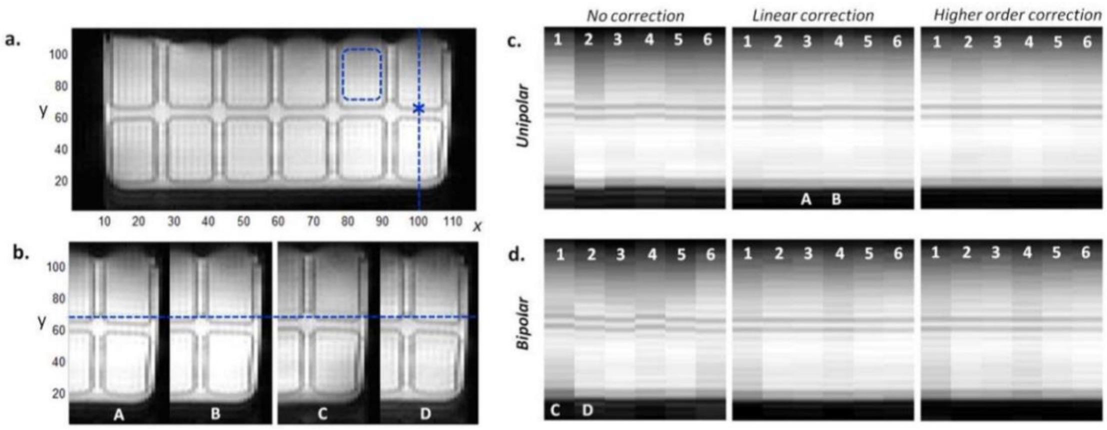

Figure 4.3 c, d) Signal plots along dashed blue line in a) for six diffusion encoding directions (b=1000s/mm^2). Corresponding eddy current corrections for first and higher spatial order. b) distorted 2D images according to letters in c) and d).

shown as columns in **Subfigure 4.3 c)** and **d)**. Image distortions are visible in the unipolar case without phase correction and linear order correction (0th and 1st order). A good alignment is achieved by higher-order correction.

For bipolar diffusion encoding, pixel shifts can be up to six pixels in the uncorrected case. However, a linear correction is already sufficient to align the images. The distorted images are shown in **Subfigure 4.3 b)** corresponding to their letters in **Subfigure 4.3 c)** and **4.3 d).** Particularly in the uncorrected images, through-slice dephasing can result in signal attenuation across the diffusion directions. These signal intensity variations are reduced by linear and higher-order phase correction, however are still slightly visible. This may translate into inaccuracies in diffusion tensor calculation afterwards.

4.1.3 Concomitant Fields

Image distortion, blurring, ghosting and signal loss can be also the result of an additional spatially varying phase induced by concomitant fields. The Maxwell equations for the magnetic flux $B(x, y, z)$ under stationary conditions read:

$$\vec{\nabla} \cdot \vec{B} = 0 \tag{4.6}$$

$$\vec{\nabla} \times \vec{B} = 0 \tag{4.7}$$

The effective magnetic field can be approximated by Taylor expansion of the net magnetic field including transverse contributions B_x, B_y:

$$B(x,y,z) = \sqrt{B_x^2 + B_y^2 + B_z^2} \tag{4.8}$$

For a cylindrical gradient coil system, generally used in MRI:

$$B(x,y,z) \approx B_0 + G_x x + G_y y + G_z z + B_C \tag{4.9}$$

with the 2nd order concomitant field term:

$$B_C = \frac{1}{2B_0}\left[\frac{G_z^2}{4}(x^2+y^2) + (G_x^2+G_y^2)z^2 - G_x G_z xz - G_y G_z yz\right] \tag{4.10}$$

As seen from eq (4.10), concomitant field terms increase with the second power of gradient strength and linearly decrease with B_0. If the k-space trajectories are known, phase errors induced by concomitant fields can be exactly calculated and incorporated into image reconstruction to reduce image distortion (137–139). Additionally, concomitant fields can also result in changes in diffusion gradient b-value and direction.

Symmetric diffusion gradients straddling the echo pulse in a spin echo experiment generate the same concomitant-field phase, however phase inversion results in zero net phase. Hence, waveform symmetrisation can be used to cancel concomitant-field phase errors. Asymmetric diffusion encoding schemes (140) can be used to improve spatial resolution, however, suffer from signal dephasing due to concomitant gradient contributions from eq. (4.10).

4.1.4 Fat Suppression

Spins with a chemical shift of ΔF are shifted along frequency and phase encoding direction according to eq. (4.1) and (4.2):

$$\Delta_x = \frac{\Delta F}{BW_m} FOV_x, \Delta_y = \frac{\Delta F}{BW_p} FOV_y \tag{4.11}$$

ΔF between water and fat is approximately 220 Hz (139) at 1.5T. In case of single-shot EPI, the fat shift along the frequency encoding direction is negligible, whereas fat

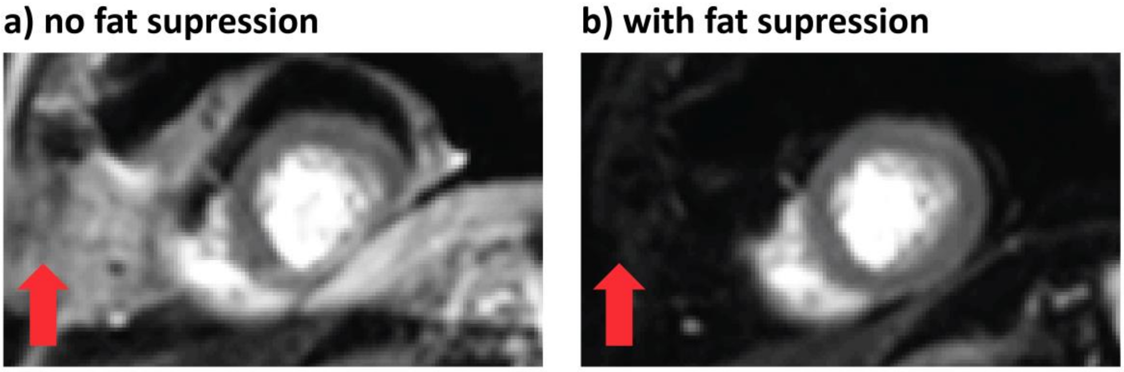

Figure 4.4 SE based diffusion acquisition without fat suppression (a) and spectral spatial excitation pulse (b). The red arrows indicate the phase encoding direction.

displacement along phase encoding directions is typically several pixels and may overlap with regions of interest (**Figure 4.4 a)**). Fat suppression can be employed by spectral spatial excitation (**Figure 4.4 b)**) or spectral presaturation with inversion recovery (SPIR) (139,141). Considering stimulated echo acquisition mode (STEAM) sequences, fat suppression in STEAM is less crucial. Due to the relatively short T1 of fat (~250ms @ 1.5T) compared to myocardium (~1000ms @ 1.5T), a major fraction of longitudinal magnetization of lipids relaxes during the mixing time of STEAM (139).

4.1.5 Signal-to-Noise Ratio (SNR)

One of the major challenges of cardiac diffusion imaging with single-shot EPI is the intrinsic low SNR. This is due to several aspects: the echo signal decays with a relatively short T2 of approximately 52ms for myocardium at 1.5T (142). Additionally, TE is prolonged (60-70ms) by the echo train length and the diffusion encoding time for higher-order motion-compensated gradients. To minimize TE, maximum gradient strength and slew rate are typically used for diffusion encoding and image readout. The SNR efficiencies (i.e. SNR normalized to the square root of time) for SE and STEAM sequences read:

$$SNR_t(SE) \propto B_0 \Delta V (1-\mathrm{e}^{-TR/T1})\,\mathrm{e}^{-TE_{SE}/T2}\,\frac{\sqrt{N_x N_y N_z}}{\sqrt{N}\sqrt{BW}} \tag{4.12}$$

$$SNR_t(STEAM) \propto \frac{1}{2}\frac{1}{\sqrt{2}} B_0 \Delta V (1-\mathrm{e}^{-TR/T1})\,\mathrm{e}^{-TM/T1}\mathrm{e}^{-TE_{STEAM}/T2} \frac{\sqrt{N_x N_y N_z}}{\sqrt{N}\sqrt{BW}} \tag{4.13}$$

$$TR = \frac{60\ \mathrm{min}^{-1}}{HR[\mathrm{min}^{-1}]} \cdot 1000ms, \quad TM = TR - \frac{TE_{STEAM}}{2} \tag{4.14}$$

with the main magnetic field B_0, the voxel volume $\Delta V = \Delta x \Delta y \Delta z$, N as the number of signal averages and $N_{x,y,z}$ the number of data samples along x, y, z direction. The factors 1/2 and 1/√2 in eq. (4.13) account for the inherent signal loss in STEAM and the need for two cardiac cycles in stimulated echo formation. According to eq (4.12) and (4.13), spatial resolution is on the order of mm assuming relevant scan time and SNR. SNR can be improved by increasing B_0, increase of the voxel size and the number of signal averages. If multiple 2D slices are acquired, SNR can be enhanced by prolonging TR using slice cycling. **Figure 4.5** compares the SNR_t for SE and STEAM at 1.5T and 3T. The corresponding T1 and T2 values of myocardium were taken from Table 4.1.

	1.5T	3.0T
T1 [ms]	1030±39	1341±42
T2 [ms]	52±3	42±4

Table 4.1 T1 and T2 values for myocardium taken from (142–145)

Relevant values for TE were taken from the literature (146) assuming second-order motion-compensated gradients for SE based imaging: TE_{SE}: 70ms, TE_{STEAM}: 31ms. All values for SNR_t are normalized to SNR_t of the first signal average in the SE case at 1.5T (marked with the cross in Figure 4.5 a). Partial signal saturation along multiple signal averages can be seen in all cases. Cardiac diffusion imaging using spin echoes is clearly favourable with respect to SNR at both field strengths. For a heart rate of 60 beats/minute the ratio of SNR_t(SE) vs. SNR_t(STEAM) is approximately 3.5 and 2.4, at 1.5T and 3T, respectively.

a) Relative SNR$_t$ (1.5 T)

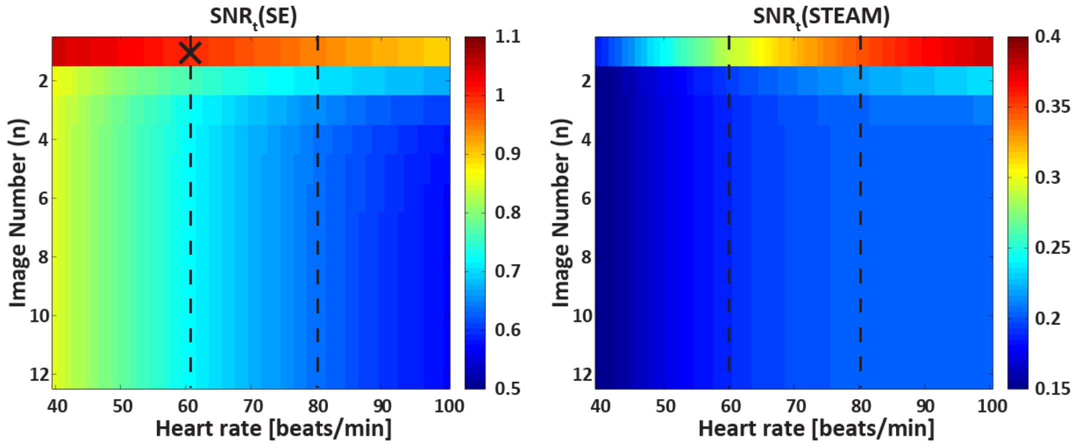

b) Relative SNR$_t$ (3.0 T)

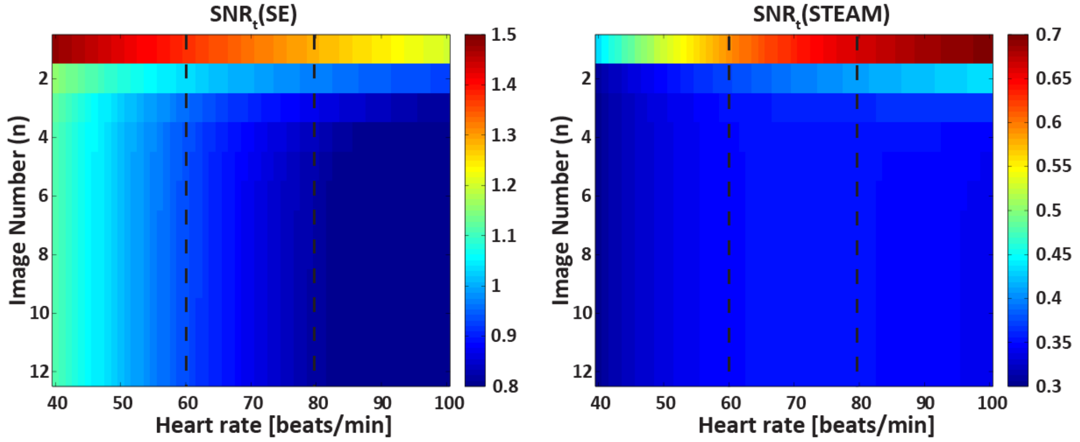

c) Relative SNR$_t$ (60, 80 beats/min)

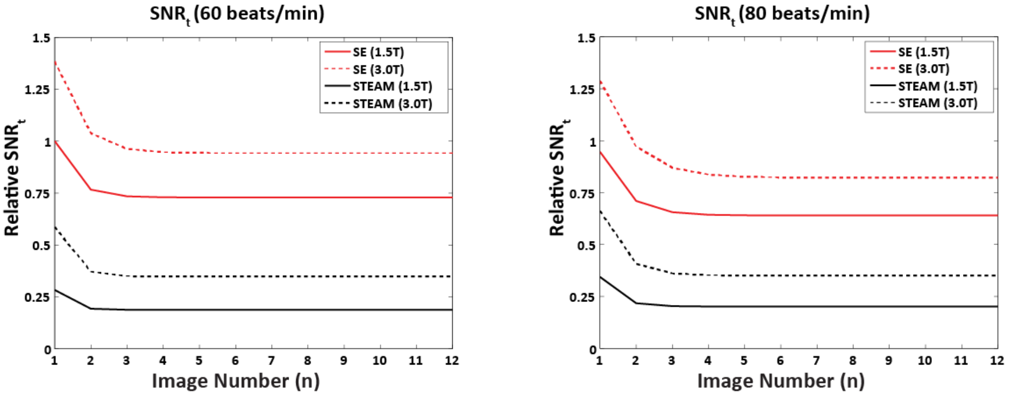

Figure 4.5 a, b) SNR efficiencies for 1.5 and 3T, respectively. SNR$_t$ with SE is increased relative to STEAM. For increasing heart rate, SNR$_t$ of SE reduces and increases in the STEAM case. c) Increasing the main field strength from 1.5 to 3.0 T, leads to an increase in SNR$_t$ of 29%/30% (60/80 bpm) for SE and 80%/75% (60/80 bpm) for STEAM.

According to **Table 4.1**, myocardial T2 is approximately 20% shorter at 3T compared to 1.5T, leading to increased signal loss by T2 decay. Hence, the requirement for high performance gradient hardware is of even greater importance at 3T compared to 1.5T. In addition, specific-absorption-rate (SAR) limitations restrict maximum B_1 amplitudes to 10-15µT at 3T relative to 25-30µT at 1.5T. As SE based diffusion imaging requires dedicated fat suppression, stringent B_1 limitations hamper efficient fat suppression using spectral spatial excitation (141). Finally, phase errors due to local susceptibility variations scale linearly with B_0 (122). Consequently, image distortions and signal dephasing are pronounced at high field strengths. As discussed, this issue can partly be addressed by k-space subsampling and parallel imaging, however, these approaches have their own limitations.

4.2 Physiological Challenges

4.2.1 Respiratory and Bulk Motion

During respiration, the heart moves primarily along the foot-head direction. To ensure consistent slice position during data acquisition, respiratory motion needs to be considered. A pencil beam navigator placed on the right hemi diaphragm can be used to gate image acquisition during breath holding or free breathing (**Figure 4.6**). The size of the acceptance window determines position accuracy of the imaging slice along the long axis and is typically in the range of a few millimetre. It has been shown, that navigator efficiency during free breathing acquisition can be increased by additional visual feedback systems (37). In addition, slice tracking allows for on-the-fly correction of slice position using navigator offsets, further improving scan efficiency (119). Even with navigator gating, residual misalignment due to respiratory or bulk motion may still be present across diffusion-weighted images. Furthermore, eddy currents can cause image distortions between different diffusion encoding directions.

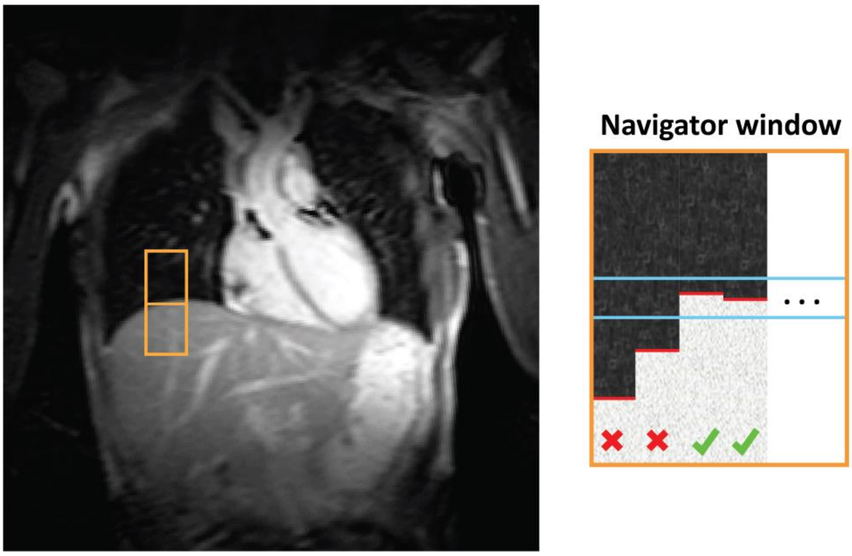

Figure 4.6 Respiratory navigator gating by a pencil beam navigator placed on the right hemi diaphragm. Images are accepted, if the navigator is within the acceptance window indicated by the blue lines.

To address these image inconsistencies, geometrical alignment is improved by additional image registration during post-processing prior to tensor calculation. Registration target for the moving images can be the mean image of all directions or a single direction or the b=0s/mm^2 image, if SNR is sufficient. To account for large displacements, images can be rigidly registered to the target image in a first step, followed by an additional affine or non-rigid registration process. Standard similarity metrics for image registration are mutual information, cross-correlation or intensity differences (147). **Figure 4.7** and **Figure 4.8** illustrate the effect of image registration. The columns in **Figure 4.7** represent the signal profiles along the horizontal dashed red lines. Bulk motion can lead to spatial displacements of up to 7 pixels, corresponding to approximately 10mm. Upon affine image registration, intensity profiles show a good alignment across the diffusion directions. Particularly at the endo- and epicardial surfaces, geometrical inconsistencies between diffusion-weighted images causes corrupted tensor orientations, leading to increased transverse angles and incorrect helix angles as shown in **Figure 4.8**.

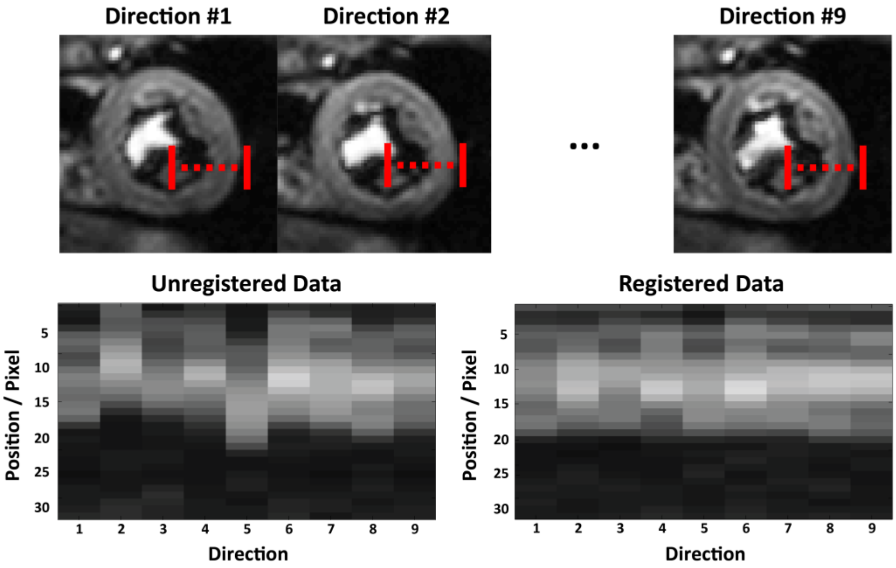

Figure 4.7 Misalignment of diffusion-weighted images due to bulk and respiratory motion can be corrected for by image based registration. Upon affine registration, intensity profiles (dashed red line) are well aligned.

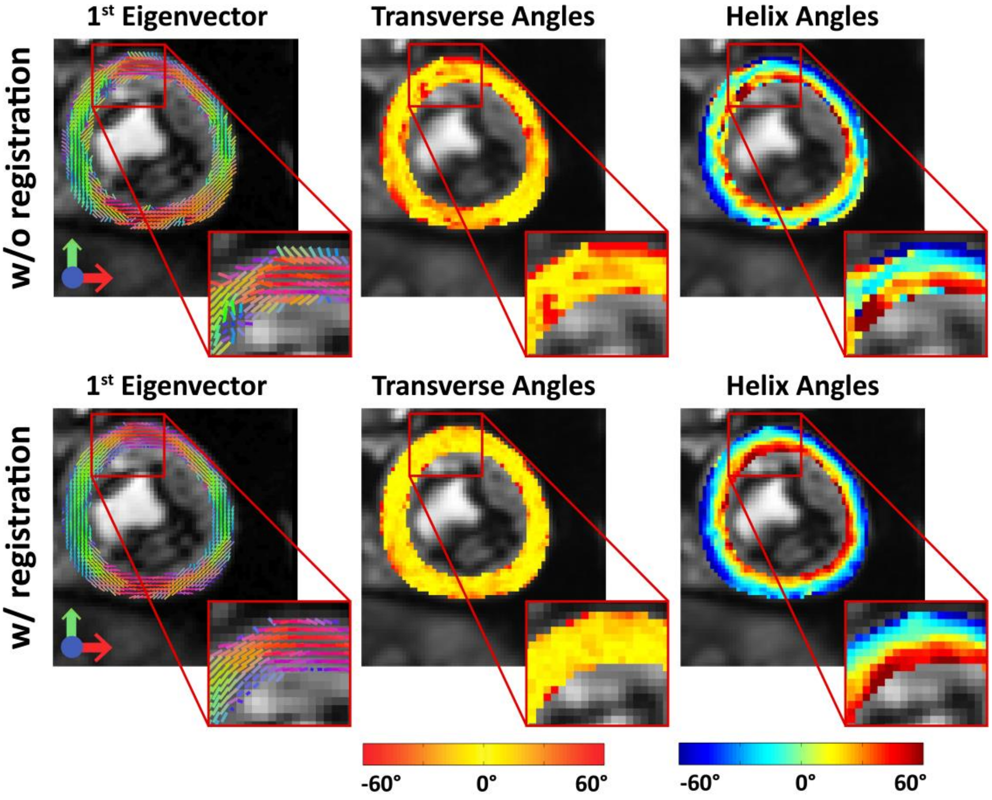

Figure 4.8 Misalignment causes inconsistent diffusion tensors, particularly at the endo- and epicardial boundaries. This results in increased transverse angles and erroneous helix angle estimation.

4.2.2 Cardiac Motion

Ex vivo cardiac diffusion imaging can be performed using classical Stejskal-Tanner diffusion encoding as the technical challenges of *in vivo* imaging, such as cardiac contraction and bulk motion are absent. If acquisition time can be increased relative to *in vivo* imaging, high resolution diffusion imaging is feasible (48,62,66).

In vivo cardiac diffusion imaging is very challenging due to the complex cardiac motion pattern. As described in Chapter 2.2., the left ventricular wall makes a twist and contracts with radial thickening and circumferential and longitudinal shortening during systole. The contraction pattern shows regional variation across the LV with greatest circumferential and radial stretch at the apex and base, respectively (148,149). In case of cardiac disease, cardiac motion can become unpredictable and inconsistent due to conduction abnormalities or mechanical dysfunction (150–153).

For *in vivo* diffusion imaging, two sequence designs have been established: The primary method relies on the stimulated echo acquisition mode (STEAM) as proposed by Edelman et al. (20). Alternatively, *in vivo* cardiac diffusion imaging has been performed using spin echoes (33–35,146,154,155).This method, however, is highly sensitive to the cardiac motion due to the relatively long diffusion encoding gradient waveforms compared to the STEAM sequence. As shown by Wedeen et al. (156) and Gamper et al. (33), cardiac motion causes signal loss if the resulting phase gradient exceeds π/2 per voxel. To reduce this motion sensitivity, diffusion encoding gradient waveforms with up to third order motion compensation have been proposed (33–35). Cardiac diffusion encoding using spin echoes and stimulated echoes will be reviewed in the next two chapters.

Motion induced signal loss can be (partly) recovered by means of Principal Component Analysis (PCA) in combination with Temporal Maximum Intensity Projection (TMIP) as shown by Pai et al. (40). PCATMIP is performed on a series of diffusion-weighted images acquired with different trigger delays during a time window with minimal cardiac motion in diastole (133). The feasibility of this approach was shown for IVIM and DTI measurements (119,120) in the human heart. When using PCATMIP, an SNR increase of up to 11% relative to pixelwise signal averaging was found (133). For multi slice imaging, scan efficiency can be increased to 100% duty cycle by using real-time, respiratory navigator based slice following acquisition as proposed by Moulin et al. (119). In contrast to single-phase DTI acquisitions which typically require 8 to 16 signal averages per diffusion encoding direction (34,37,38,146,157), PCATMIP based DTI and IVIM measurements have been performed with 10 trigger time points without averaging (119,133). As the STEAM sequence spans over two consecutive R-R-intervals, scan time efficiency of PCATMIP based DTI is higher compared to the combination of single-phase imaging and signal averaging.

4.2.2.1 Spin Echo based diffusion imaging

The unipolar Stejskal-Tanner spin echo sequence is not suitable for *in vivo* cardiac diffusion imaging. Myocardial strain and bulk motion is encoded by the diffusion gradients resulting in intravoxel dephasing which cannot be discriminated from diffusion induced phase alteration (156). The effect on spin phase $\phi(t)$ due to bulk motion in the presence of diffusion gradients can be approximated by a Taylor expansion of the spin trajectory $\vec{x}(t)$ around time t_0 :

$$\phi(t)=\gamma\int_0^t \vec{G}(t')\vec{x}(t')dt' \approx \gamma\int_0^t \vec{G}(t')\vec{x}(t_0)dt' + \gamma\int_0^t \vec{G}(t')\dot{\vec{x}}(t_0)tdt' + \frac{1}{2}\gamma\int_0^t \vec{G}(t')\ddot{\vec{x}}(t_0)t^2dt' + \ldots$$

(4.15)

$$\phi(t)\approx\gamma(m_0+m_1\dot{\vec{x}}(t_0)+\frac{1}{2}m_1\ddot{\vec{x}}(t_0)+\ldots) \tag{4.16}$$

with the nth gradient moment:

$$m_n=\int_0^t \vec{G}(t')t^n dt' \tag{4.17}$$

Hence, the sensitivity to bulk motion can be reduced by gradient moment nulling. First order motion compensation was achieved with a pair of bipolar gradient blocks, as shown by Gamper et al. (33) (**Figure 4.9 a)**). The systolic time window could be extended for successful 2D diffusion tensor imaging in the beating human heart. The bipolar sequence can be shortened to a single sided bipolar gradient pair before the

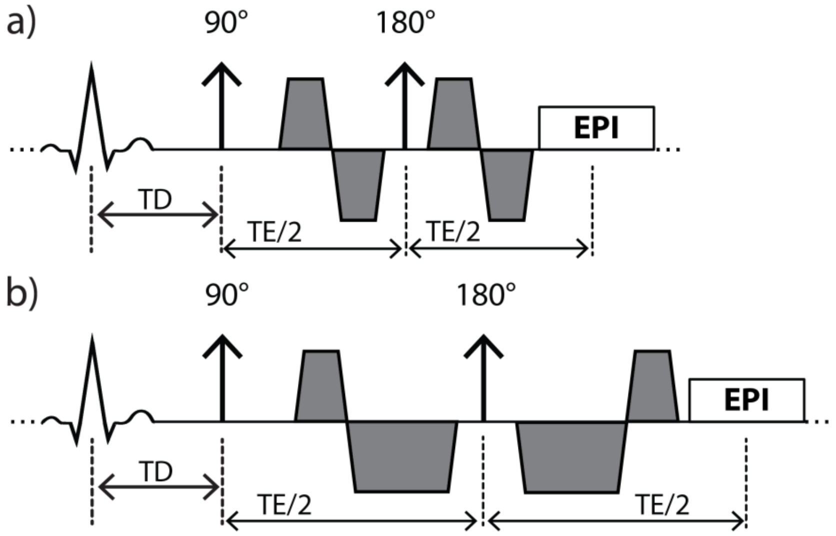

Figure 4.9 First- (a) and second- (b) order motion-compensated diffusion sequences with single-shot EPI readout.

180° pulse as shown in (140). This approach benefits from a reduced echo time, however suffers from signal dephasing due to concomitant fields and only 0^{th} order motion compensation. *In vivo* cardiac diffusion imaging with second-order motion-compensated diffusion encoding gradients has been proposed recently (34,35). The extended diffusion gradient waveforms, however, lead to an increase in diffusion encoding and echo time (**Figure 4.9 b)**). Hence, for sufficient SNR, gradient systems with high gradient strength and slew rate are necessary if higher-order motion-compensated waveforms are employed. **Figure 4.10** depicts sample diffusion-weighted images using acceleration-compensated diffusion encoding. The red arrows indicate diffusion encoding direction along phase, measurement and slice direction, respectively. Local signal attenuation is increased, if the principal fibre orientation (**Figure 4.10 d)**) is parallel to the diffusion encoding direction.

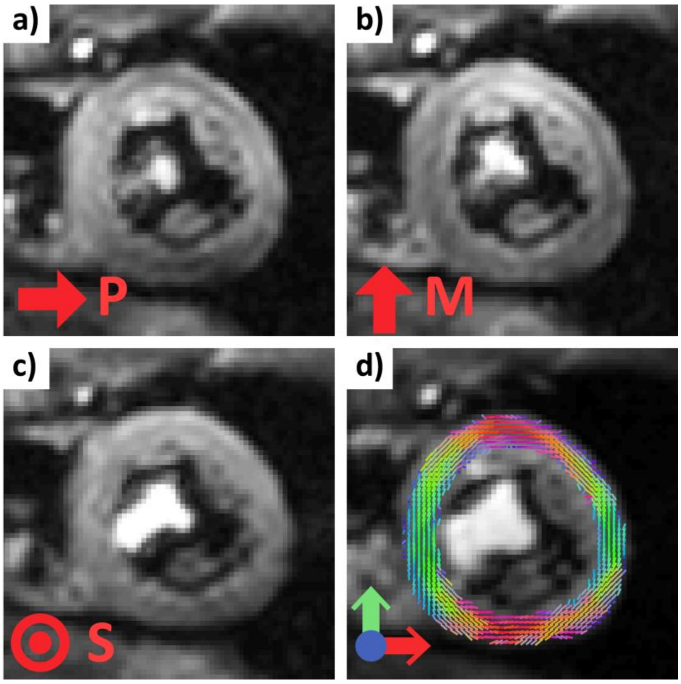

Figure 4.10 Example data of second-order motion-compensated diffusion-weighted imaging (b=450s/mm^2). Diffusion encoding is along phase (a), measurement (b) and slice selection (c) direction (indicated by the red arrows). d) color-coded orientation of the first diffusion tensor eigenvector.

4.2.2.2 STEAM based diffusion imaging

In vivo cardiac DTI studies have successfully been performed with a double gated STEAM sequence (**Figure 4.11**) (20,30,32,37–39,79,81,87,158–160). The sequence spans over two consecutive heartbeats with the first and third 90° pulse applied at the same trigger delay, followed by unipolar or bipolar diffusion gradients. Assuming constant heart rate, the diffusion encoding is performed in the same cardiac phase in successive cardiac cycles.

Diffusion sensitization primarily occurs during the mixing time $TM = RR - {}^{TE}\!/_{2}$ such that short diffusion gradients with moderate gradient strength are sufficient for adequate diffusion weighting. Furthermore, quasi identical motion trajectories during the application of the short diffusion encoding gradients make the STEAM sequence less sensitive to bulk motion. During TM, magnetization stored in the longitudinal direction decays with T1, in contrast to T2 decay in a diffusion-weighted SE sequence (161) (**Figure 4.5**).

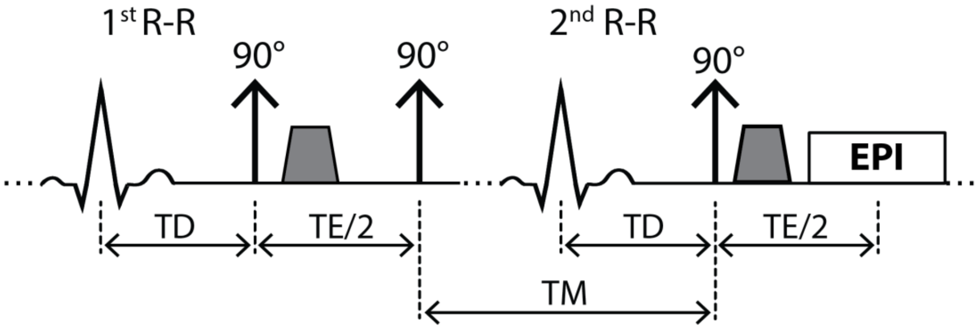

Figure 4.11 STEAM sequence spanning over two consecutive heartbeats with unipolar diffusion encoding and single-shot EPI readout.

Besides the intrinsic SNR loss of 50% relative to spin echoes and the inherent time inefficiency, STEAM requires the spatial position of the heart to be consistent over consecutive heartbeats. Accordingly, repeated breathholding or respiratory navigator gating with narrow acceptance windows need to be employed (37). Cardiac motion is assumed to be periodic for STEAM imaging, however, heart rate variations or arrhythmia can cause signal loss, particularly in case of diastolic triggering (37).

The STEAM sequence with unipolar diffusion encoding gradients is sensitive to material strain during the relatively long mixing time TM (162,163). As the diffusion gradients phase encode the local displacement distribution (164), myocardial deformation during the cardiac cycle results in additional modulation of the encoding strength which confounds diffusion induced signal attenuation (162,163,165). The impact of material strain on the diffusion tensor can be determined if the strain tensor is known (38,163,166). The apparent diffusion tensor can be expressed by the right stretch tensor $U(t)$ and the true diffusion tensor D_{true}:

$$D_{apparent} = \frac{1}{\Delta}\int_{0}^{\Delta} U(t)^{-1} D_{true} U(t)^{-1} dt \tag{4.18}$$

with Δ being the duration of the R-R cycle. With known stretch tensor $U(t)$, eq. (4.18) can be inverted, leading to the undisturbed diffusion tensor D_{true}. As shown by Stoeck et al., $U(t)$ can be computed from 3D tagging images (38).

Figure 4.12 summarizes the processing steps for diffusion tensor strain correction. As a first step, diffusion and tagging data are registered to ensure geometric consistency.

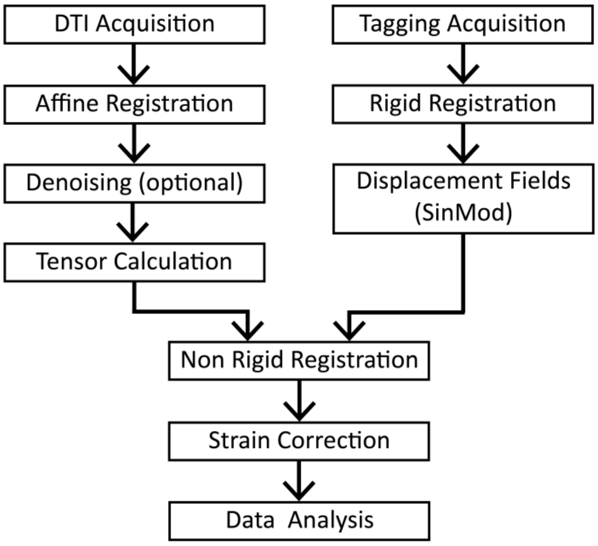

Figure 4.12 *Strain correction pipeline: Diffusion and tagging data are registered prior to tensor calculation and displacement field computation. Using non-rigid registration, left ventricular shapes of tagging and diffusion data are mapped onto each other followed by diffusion tensor strain correction on a pixel-by-pixel basis.*

Displacement fields are derived using the SinMod algorithm (167) and diffusion data may be denoised (168) prior to tensor calculation. Upon manually masking the LV on diffusion and tagging data, corresponding points between both domains are registered by 2D non-rigid transformation (169). Deformation gradient fields and right stretch tensors are calculated for each position of calculated diffusion tensors. The true diffusion tensor D_{true} is then determined according to eq. (4.18).

Sample DTI data acquired during peak systole with and without strain correction are shown in **Figure 4.13**. Uncorrected primary eigenvectors deviate from the circumferential contour near the anterior RV/LV intersection and in the lateral wall, which leads to increased transverse angles. Upon strain correction, primary eigenvectors follow a more coherent track with reduced transverse angles.

Careful ECG trigger timing allows minimizing the effect of cardiac strain, if diffusion encoding is performed at the "sweet spots" $T*$ during the cardiac cycle. According to Tseng et al. (39), the temporal mean of material strain is zero in this case:

$$\int_{T*}^{T*+\Delta} U(t)^{-1} dt = id \qquad (4.19)$$

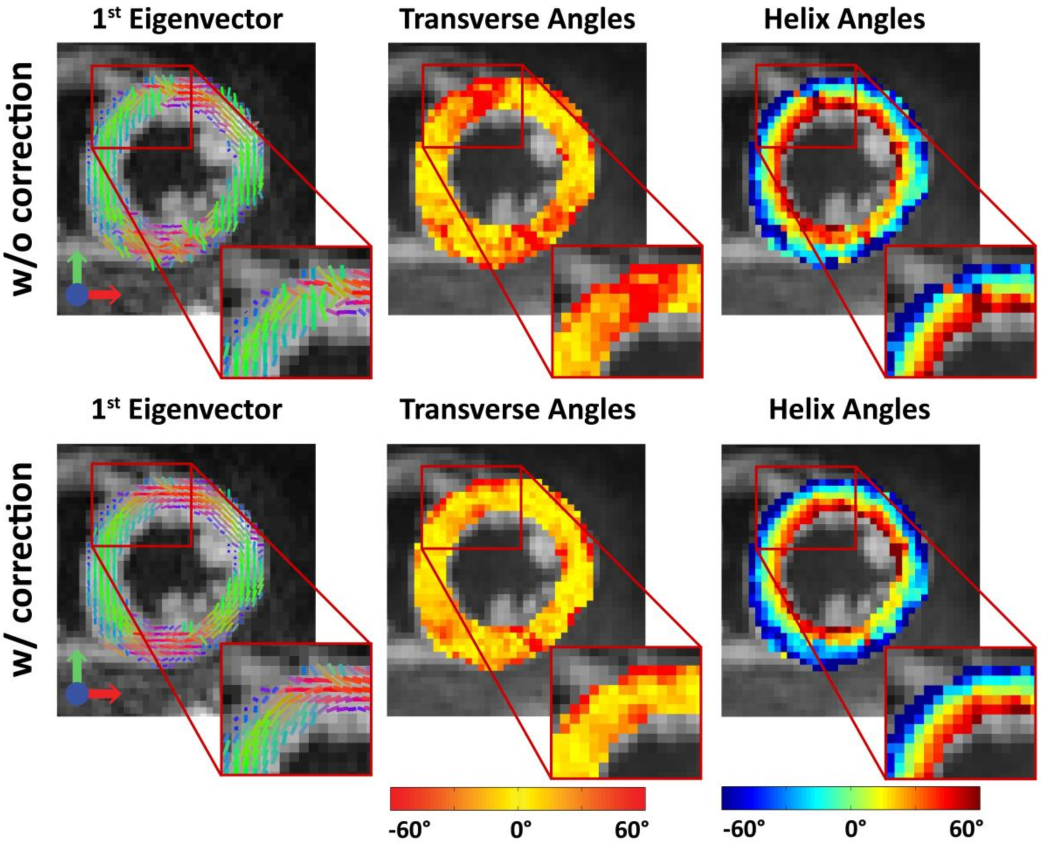

Figure 4.13 Uncorrected diffusion tensors are incoherent in the RV/LV intersection leading to increased transverse angles. Upon strain correction, first eigenvectors follow the circumferential contour more coherently.

In the healthy human heart, the sweet spots are located in mid-ejection and in mid-filling phase as shown in **Figure 4.14** (39). Alternatively, strain sensitivity can be reduced by replacing the unipolar diffusion encoding gradients with bipolar blocks as shown by Dou et al. (79). The prolonged diffusion encoding time, however increases TE and reduces SNR further.

According to eq. (3.18), the b-value depends linearly on the mixing time Δ. Consequently, heart rate variations directly affect the degree of diffusion weighting. Therefore, the effective b-value needs to be determined based on the actual heart rate (HR):

$$\Delta_{actual} = \frac{60\min^{-1}}{HR[\min^{-1}]} \cdot 1000ms - \frac{TE_{STEAM}}{2} \tag{4.20}$$

$$b_{actual} = (\gamma G \delta)^2 (\Delta_{actual} - \frac{\delta}{3}) \approx (\gamma G \delta)^2 \frac{60\min^{-1} \cdot 1000ms}{HR[\min^{-1}]} \tag{4.21}$$

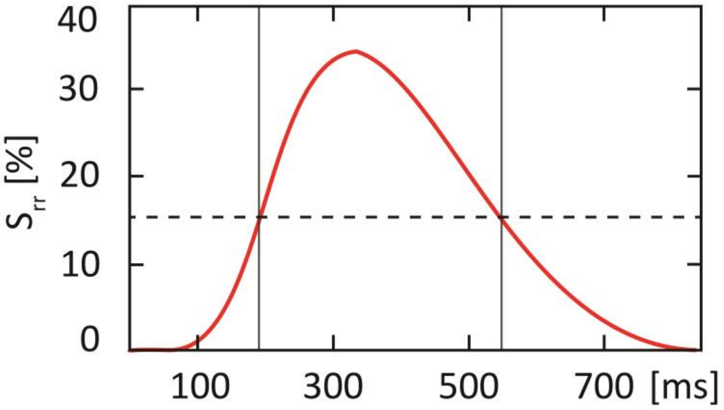

Figure 4.14 Time course of the radial strain component. Grey vertical lines indicate sweet spots in mid systole and mid diastole. The horizontal line corresponds to the temporal mean of radial strain. Figure adapted from (170).

The true MD_{true} can be derived by scaling the calculated $MD_{apparent}$ with the b-value ratio $\frac{b_{nominal}}{b_{actual}}$:

$$MD_{true} = MD_{apparent} \frac{b_{nominal}}{b_{actual}} \tag{4.22}$$

Assuming a drop in heart rate from 60 to 50beats/min, the actual b-value and $MD_{apparent}$ increase by $\frac{60-50}{50}\frac{[\min^{-1}]}{[\min^{-1}]} = 20\%$ relative to the nominal and true values, respectively. An increase in heart rate by 10beats/min to 70beats/min, reduces b_{actual} and $MD_{apparent}$ by 14%. Ideally, the actual b-value for each diffusion-weighted image is calculated and the corresponding b-matrix extended accordingly (159).

Chapter 5

Spin Echo versus Stimulated Echo Diffusion Tensor Imaging of the *In Vivo* Human Heart[*]

5.1 Introduction

The fiber architecture of the heart has significant influence on cardiac function, mechanical contraction and electrophysiology (76,83,171–173). The principal orientation of myofibers can be obtained from histological studies (63,174,175) or *ex vivo* (26,55,66) and *in vivo* (18,20,33,37–39,56,79,154,158,162,163,165) Diffusion Tensor Imaging (DTI). While histological exams provide localized information on myocyte orientation with very high spatial resolution *ex vivo*, cardiac DTI allows assessment of myofiber aggregates non-invasively and *in vivo*. In agreement with histology, *ex vivo* DTI studies have demonstrated the characteristic circumferential alignment of myofibers with a distinct double helical pattern from endo- to epicardium (45,46,176). Fiber disarray and myocardial remodeling due to myocardial infarction and cardiomyopathies have been assessed by DTI methods both in animal and humans subjects (47,48,50,51,54,87). Moreover, microstructural integrity of the myocardium

---

[*] Published in: Constantin von Deuster, Christian T. Stoeck, Martin Genet, David Atkinson, Sebastian Kozerke. “Spin Echo versus Stimulated Echo Diffusion Tensor Imaging of the In Vivo Human Heart”, Magnetic Resonance in Medicine, doi: 10.1002/mrm.25998

has been described using mean diffusivity (MD) and fractional anisotropy (FA). Whereas mean diffusivity increased in myocardial infarction, FA was found to decrease (18,31,51,54). These findings highlight the potential of *in vivo* cardiac DTI to allow for structural and functional tissue characterisation in a range of relevant diseases.

In vivo cardiac DTI has primarily been performed using the stimulated echo acquisition mode (STEAM) (18,20,37–39,79,87,158,162,163). Alternatively, spin echo (SE) imaging is feasible provided that motion-compensated diffusion gradients are employed or dedicated post-processing to account for motion-induced signal loss is used (23,33,34,40,56,161,177). Image formation is typically accomplished using echo planar imaging (EPI) or balanced steady-state free precession imaging (36). Despite the advances in sequence design and data processing, DTI of the beating heart remains a challenging task due to low signal-to-noise-ratio (SNR), off-resonance artifacts, cardiac bulk motion and myocardial strain.

In STEAM, diffusion encoding ranges across two consecutive heartbeats and hence the spatial position and shape of the myocardium are required to be identical in subsequent cardiac cycles. Accordingly, dedicated breath holding and navigator gating schemes are essential to suppress respiratory motion induced displacements. Alternatively, free breathing acquisition can be performed in combination with a dedicated navigator gating strategy and optional patient feedback system (37). The effect of myocardial strain during diffusion encoding using STEAM has to be considered by acquiring at so-called “sweet spots” (39) in the cardiac cycle. Alternatively, separately acquired strain data (38,163) may be used to correct for strain effects in the DTI data. A key advantage of STEAM over SE relates to the modest gradient hardware requirements as diffusion encoding takes place over a whole cardiac cycle and hence relatively low diffusion encoding gradient strengths are sufficient for adequate diffusion weighting.

With recent improvements in gradient hardware becoming widely available on clinical MR systems and dedicated diffusion gradient designs, diffusion-weighted single-shot spin echo (SE) sequences have become feasible for *in vivo* cardiac DTI. Several studies have shown that signal attenuation due to myocardial motion can be addressed successfully by incorporating motion-compensated diffusion gradient waveforms

(23,34,35,140,154,158,161,177–179). Promising results of the *in vivo* human (34) and rat (35) heart using second and third order motion-compensated DTI have been presented recently.

While image and data quality depend on many parameters including residual motion, off-resonance and eddy-current effects (129), the low SNR of cardiac DTI is a significant impediment to wider adoption of the technique in the clinic. Besides the need for patient feedback (37) and dedicated data post-processing (38,40), low scan time efficiency is a major reason for the small number of cardiac DTI studies on patients (29,30,180). Accordingly, a comparison of the available sequence approaches with regard to SNR and time efficiency is warranted to guide further improvements.

It is the objective of the present work to assess and compare SNR efficiency and diffusion metrics derived from cardiac DTI employing acceleration-compensated diffusion-weighted SE and cardiac triggered STEAM in both phantoms and in the *in vivo* human heart.

5.2 Methods

Figure 5.1 illustrates the ECG-triggered and diffusion-weighted STEAM and SE sequences used in the present study. For the SE variant, second-order motion-compensated diffusion gradients are employed (34).

The SNR of SE and STEAM depend on sequence timing parameters (echo time: TE, repetition time TR, mixing time TM), tissue properties (relaxation times T1, T2, diffusivity D), imaging parameters (voxel size ΔV, number of signal averages NSA, flip angle α) and diffusion encoding strength b. Here SNR efficiency (i.e., SNR normalized to the square root of time) for the SE and STEAM sequences is defined as:

$$SNR_t(\mathrm{SE}) \propto \frac{1-\mathrm{e}^{-TR/T1}}{1-\cos\alpha\,\mathrm{e}^{-TR/T1}} \sin\alpha\,\mathrm{e}^{-TE_{SE}/T2}\,\mathrm{e}^{-b\cdot D}\,\frac{\Delta V}{\sqrt{NSA}} \qquad (5.1)$$

$$SNR_t(\mathrm{STEAM}) \propto \frac{1}{2}\frac{1-\mathrm{e}^{-TR/T1}}{1-\cos\alpha\,\mathrm{e}^{-TR/T1}} \sin\alpha\,\mathrm{e}^{-TM/T1}\mathrm{e}^{-TE_{STEAM}/T2}\,\mathrm{e}^{-b\cdot D}\,\frac{\Delta V}{\sqrt{NSA}\sqrt{2}} \qquad (5.2)$$

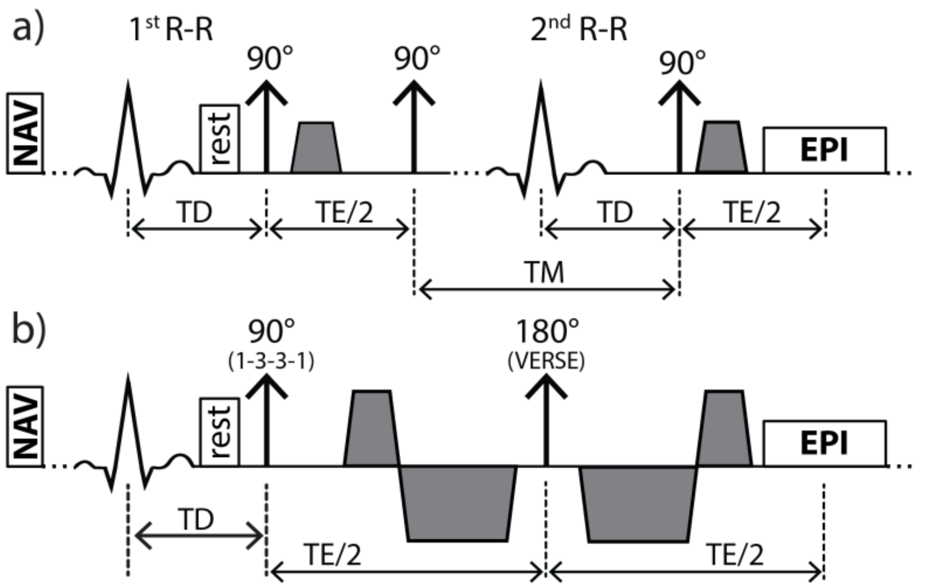

Figure 5.1 *Sequence diagrams. a) STEAM acquisition spanning over two consecutive heartbeats and b) SE acquisition with second-order motion-compensated diffusion encoding gradients including VERSE (variable rate selective excitation) echo pulse. Fat suppression is achieved by a binomial excitation pulse. The excitation slab is tilted with respect to the 90° or 180° pulses to allow for reduced field of view imaging. Prior to the first 90° excitation, rest slabs are applied orthogonal to the field of view in phase encoding direction to suppress residually excited signal. For both sequences, the trigger delay was set to mid systole and images were encoded by identical single-shot EPI readouts.*

In equation (5.2) the factors $1/2$ and $1/\sqrt{2}$ account for the inherent signal loss in STEAM and the fact that two cardiac cycles are required to encode the stimulated echo. Because of ECG triggering, TR and TM are determined by the subject's heart rate (HR) according to:

$$TR = \frac{60 \min^{-1}}{HR[\min^{-1}]} \cdot 1000[ms] \quad TM = TR - \frac{TE_{STEAM}}{2} \tag{5.3}$$

In **Figure 5.2** the ratio of SNR efficiency for SE versus STEAM, SNR_t(SE/STEAM), is presented with sequence parameters according to the gradient system used in this study (b-value=450s/mm^2, TE_{SE}=70ms, TE_{STEAM}=31ms). The SNR_t(SE/STEAM) ratio is seen to decrease with increasing heart rate but remains greater than 2.3 up to heart rates of 90min^{-1}. At a heart rate of 60min^{-1} and T1/T2 = 1030/52ms (142,143) the theoretical SNR gain of SE relative to STEAM is approximately 3.5x.

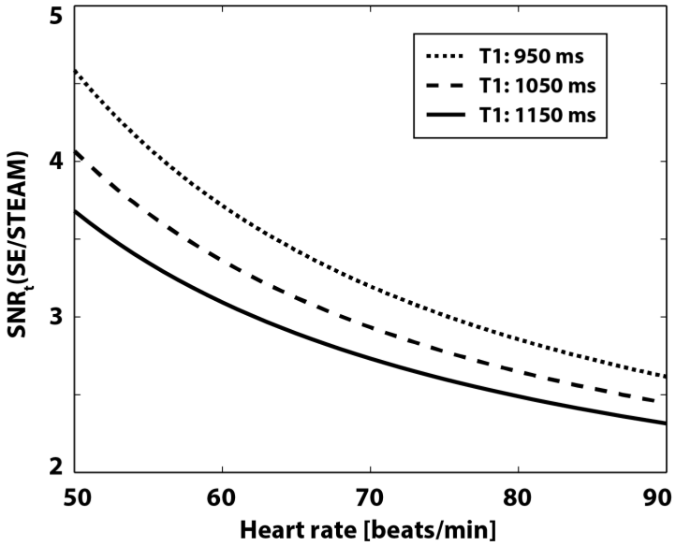

Figure 5.2 Theoretical SNR efficiency. The SNR efficiency ratio of SE versus STEAM is seen to decreases with increasing heart rate. At a heart rate of 60min^{-1}, b-value=450s/mm^{2}, TR/TE=1000ms/70ms (SE), TR/TM/TE=1000ms/985/31ms (STEAM) the relative gain in SNR efficiency of SE versus STEAM is 3.5x.

Study Protocol

Cardiac SE and STEAM diffusion-weighted imaging were implemented on a 1.5T Philips Achieva System (Philips Healthcare, Best, The Netherlands) with gradients delivering 80mT/m maximum strength at a slew rate of 100mT/m/ms per physical axis. Signal was received with a 5-channel cardiac receiver array. Written informed consent was obtained from all subjects prior to imaging. The study protocol was approved by the ethics committee of the Canton of Zurich. Consent included imaging as well as publication of anonymized data.

Phantom Measurements

A phantom with isotropic diffusivity was made from an aqueous agar solution with a concentration of 40g/l. T1 was reduced by addition of 2.5×10^{-6}mmol/l Gadolinium (Primovist, Bayer Schering, Germany) and relaxation times determined by a vendor pre-implemented imaging sequence (181): $T1_{Agar}$ = 1153±10ms, $T2_{Agar}$ = 49.6±0.4ms within a region of interest inside the phantom.

To probe differences of the diffusion process during SE and STEAM diffusion encoding, a dedicated diffusion phantom with fiber structures mimicking cardiac myofibers was used in a second set of phantom measurements. The phantom consists of two crossing fiber bundles (~20mm diameter) of hydrophobic polyethylene cords as described previously (182).

The SNR efficiency of SE and STEAM was determined for several b-values (50, 100, 200, 300 and 450s/mm^2). Diffusion-weighted images were acquired with in-plane resolution: 2.8×2.8mm^2, slice thickness: 16mm (isotropic phantom)/12mm (anisotropic phantom), field of view (FOV): 230×98mm^2, TR/TE (SE): 1000ms/70ms, TR/TE (STEAM): 1000ms/31ms, flip angle (SE, STEAM): 90°, 4 signal averages and 6 diffusion encoding directions (**Table 5.1**). To measure noise, the scans were repeated without RF and gradient pulses keeping the receiver gain and bandwidth the same as for actual imaging. Sufficient time (>10sec) was allowed between image and noise acquisition to ensure complete signal decay. SNR was determined for each voxel by dividing the absolute signal value of the diffusion-weighted images by the standard deviation of the real part of complex noise in a local mask of 9 by 9 pixels. SNR_t(SE/STEAM) of the anisotropic diffusion phantom was corrected for different T1/T2 values between both phantoms ($T1_{\text{diffusion phantom}}$ = 934±42ms, $T2_{\text{diffusion phantom}}$ = 104.2±4ms).

To reduce perfusion effects (115,159,183), *in vivo* DTI was performed without the b = 0s/mm^2 image. Instead, three low diffusion-weighted images (b = 100s/mm^2) were acquired along orthogonal directions along with nine additional diffusion-weighted images (b = 450s/mm^2) distributed on the edge of a cube to maximize gradient utilisation and hence gradient strength. The duration of diffusion encoding gradients for the different diffusion weightings was kept the same and differences in b-values were achieved by scaling the gradient strength. Imaging parameters were as follows: in-plane resolution: 2.8×2.8mm^2, slice thickness: 12mm, field of view (FOV): 230×98mm^2, TR/TE (SE): 1000ms/70ms, TR/TE (STEAM): 1000ms/31ms, number of signal averages: 16. To examine the effect of the sequence upon MD and FA, rather than any effects due to intrinsic SNR dependence (184), the flip angle of the SE excitation pulse was reduced to 16° to match SNR of the corresponding STEAM sequence (flip angle STEAM: 90°). Hence, variations in MD and FA can be uniquely assigned to differences during the diffusion encoding process.

SNR measurement (isotropic phantom)

	Resolution	b-values [s/mm^2]	Flip angle [deg]	# directions	NSA
SE	2.8x2.8x16mm^3	50,100,200,300,450	90	6	4
STEAM	2.8x2.8x16mm^3	50,100,200,300,450	90	6	4

SNR measurement (anisotropic phantom)

	Resolution	b-values [s/mm^2]	Flip angle [deg]	# directions	NSA
SE	2.8x2.8x12mm^3	50,100,200,300,450	90	6	4
STEAM	2.8x2.8x12mm^3	50,100,200,300,450	90	6	4

DTI measurement (anisotropic phantom)

	Resolution	b-values [s/mm^2]	Flip angle [deg]	# directions	NSA
SE	2.8x2.8x12mm^3	100,450	16	12	16
STEAM	2.8x2.8x12mm^3	100,450	90	12	16

Table 5.1 Imaging parameters of SNR and DTI phantom experiments

In Vivo Measurements

Data were acquired in seven healthy subjects without history of cardiac disease (5 female, weight 64±6kg, age 28±6years, heart rate 64±10beats/min, min/max heart rates: 49/89beats/min). Prior to diffusion imaging, cine data with a temporal resolution of 10ms were acquired in two-chamber and short-axis view orientations. According to the cine images, systolic quiescent time points were determined on a per subject basis with a mean delay of 316±19ms.

Diffusion-weighted imaging was performed during breath holding in short-axis view orientation with a reduced field-of-view (FOV) technique (185). Consistent levels of breath-holds were ensured by the use of a respiratory navigator placed on the right hemi diaphragm with a gating window of 5mm. To avoid aliasing from residual excitation along the phase encoding direction, saturation slabs orthogonal to the imaging plane were played out prior to the RF excitation pulse (see **Figure 5.1**). A 1-3-3-1 binomial spatial-spectral excitation pulse for fat suppression (141) was employed in the SE case. The duration of the 180° refocusing pulse was minimized using variable rate selective excitation (VERSE) (186) (**Figure 5.1**). Diffusion weighting was performed by unipolar gradients (STEAM) and second-order motion-compensated gradient waveforms (SE) as proposed in (34,35).

The trigger delay (TD) of the STEAM sequence was set to the systolic strain “sweet spot” (50% end systole as shown in **Figure 4.14**). At this time point in the cardiac cycle, strain approximates its temporal mean and the impact on diffusion metrics is minimized (39). The centers of mass of the STEAM and SE diffusion gradients within an R-R interval were aligned, resulting in a trigger delay for the SE sequence of 45% peak systolic contraction. *In vivo* SNR measurements were performed in each volunteer similar to the phantom experiments with a slice thickness of 16mm to increase SNR. To guarantee identical b-values for the SE and STEAM sequences, the effective b-values during STEAM acquisitions were calculated based on the actual heart rates recorded during the *in vivo* experiments. Additionally, sufficient time to recover between the breath holds was ensured to avoid significant heart rate variations during scanning. To avoid magnetization transients during imaging, the first average was used as dummy scan and discarded.

For DTI, total scan time of the *in vivo* experiments was matched between SE and STEAM. Accordingly 8 signal averages per diffusion encoding direction were acquired with STEAM while 16 averages were recorded with SE (**Table 5.2**). The imaging slice (slice thickness: 8mm) was positioned at a mid-ventricular level. Data acquisition was split into multiple breath holds by acquiring all signal averages of a single diffusion encoding direction during a single breath hold. Between the breath holds, sufficient time for complete relaxation of magnetization was insured.

Additionally, DTI and SNR measurements were repeated during respiratory navigator-gated free breathing acquisition with identical imaging and sequence parameters. Data collection was performed in seven healthy volunteers (5 female, weight 62±9kg, age 24±2years, heart rate 66±10beats/min) in a separate imaging session. The methods and results are listed in the Appendix and **Figure 5.9**.

SNR measurement (*in vivo*)

	Resolution	b-values [s/mm^2]	Flip angle [deg]	# directions	NSA
SE	2.8x2.8x16mm^3	50,100,200,300,45	90	6	4
STEAM	2.8x2.8x16mm^3	50,100,200,300,45	90	6	4

DTI measurement (*in vivo*)

	Resolution	b-values [s/mm^2]	Flip angle [deg]	# directions	NSA
SE	2.8x2.8x8mm^3	100,450	90	12	16
STEAM	2.8x2.8x8mm^3	100,450	90	12	8

Table 5.2 Imaging parameters of SNR and DTI in vivo experiments

Data Analysis

The mean SNR of the phantom and *in vivo* data was determined for all acquired b-values ranging from b=50s/mm^2 to 450s/mm^2. SNR efficiency ratios of the SE sequence relative to the STEAM approach were calculated and compared to the theoretical values according to equations (5.1) and (5.2) taking the individual sequence timing (TR, TM, TE) into account. Relaxation times (T1=1030ms/T2=52ms) were taken from literature (142,143).

For diffusion tensor analysis, images were first registered to the mean image using affine image transformations (elastix toolbox (147)). The *in vivo* SNR was determined using myocardial contours. To avoid partial voluming effects, voxels at the epi- and endocardial borders were excluded from the statistics. The actual b-values due to heart rate variations were corrected for by adjusting b_{100} and b_{450} to the corresponding true values and the b-matrix modified for the proposed sampling scheme. The corresponding set of equations reads:

$$\mathrm{B}^{\dagger}\vec{\mathrm{S}} = \vec{\mathrm{D}} \tag{5.4}$$

The modified b-matrix reads:

$$B=\begin{bmatrix} b_{100}\begin{pmatrix} x^2_{diff\,01} & y^2_{diff\,01} & z^2_{diff\,01} & 2xy_{diff\,01} & 2xz_{diff\,01} & 2yz_{diff\,01} \\ & & & \vdots & & \\ x^2_{diff\,03} & y^2_{diff\,03} & z^2_{diff\,03} & 2xy_{diff\,03} & 2xz_{diff\,03} & 2yz_{diff\,03} \end{pmatrix}\begin{pmatrix} -1 \\ \vdots \\ -1 \end{pmatrix} \\ b_{450}\begin{pmatrix} x^2_{diff\,04} & y^2_{diff\,04} & z^2_{diff\,04} & 2xy_{diff\,04} & 2xz_{diff\,04} & 2yz_{diff\,04} \\ & & & \vdots & & \\ x^2_{diff\,12} & y^2_{diff\,12} & z^2_{diff\,12} & 2xy_{diff\,12} & 2xz_{diff\,12} & 2yz_{diff\,12} \end{pmatrix}\begin{pmatrix} -1 \\ \vdots \\ -1 \end{pmatrix} \end{bmatrix} \tag{5.5}$$

b_{100} and b_{450} are the two heart rate adjusted b-values (nominal values: 100 and 450s/mm^2). $\vec{S}$ denotes the negative logarithmic signal vector

$$\vec{\mathrm{S}}=-\ln\left(\left[\mathrm{S}_{\mathrm{diff}\,01} \quad \cdots \quad \mathrm{S}_{\mathrm{diff}\,12}\right]^{\mathrm{T}}\right) \tag{5.6}$$

The $\vec{D}$ vector contains the diffusion tensor elements and the b=0s/mm^2 signal S_0:

$$\vec{\mathrm{D}}=\left[\mathrm{D}_{\mathrm{x}^2} \quad \mathrm{D}_{\mathrm{y}^2} \quad \mathrm{D}_{\mathrm{z}^2} \quad \mathrm{D}_{\mathrm{xy}} \quad \mathrm{D}_{\mathrm{xz}} \quad \mathrm{D}_{\mathrm{yz}} \quad \ln\left(\mathrm{S}_0\right)\right]^{\mathrm{T}} \tag{5.7}$$

$\dagger, T$ denote the Moore-Penrose pseudo inverse and transpose, respectively.

Upon tensor calculation the helix and transverse angles were calculated. Here the helix angle captures the local helix elevation, i.e., the angle between the projection of the first eigenvector of the diffusion tensor onto the epicardial surface and the transmural plane. The transverse angle represents the deviation of the helix from circumferential structure, i.e. the angle between the first eigenvector projected onto the radial circumferential plane and the circumferential contour (22). For each diffusion tensor, a normalized transmural position was calculated. Angle analysis was performed for the anterior, septal, inferior and lateral region separately. Furthermore, the gradient of a linear fit to the transmural helix angle course was calculated. Reproducibility of MD and FA were assessed by a two-tailed paired t-test and the Bland-Altman method (187). Significance of difference between SE and STEAM diffusion tensor metrics was evaluated by a two-tailed paired t-test. Prior to statistical analysis, values were checked for normality and equality of variances in SPSS (Version 23, IBM Corp., Armonk, NY) using the Shapiro-Wilk and Levene test, respectively. If the requirements for the t-test were not fulfilled, a non-parametric Wilcoxon signed-rank test was used instead. A p-value smaller than 0.05 was considered statistically significant.

5.3 Results

SNR Measurements

Figure 5.3 a) shows example *in vivo* images for the b = 100 and 450s/mm^2 acquisitions obtained by the SE and STEAM approach. The bright blood pool signal in the b = 100s/mm^2 image of the SE measurements is dephased with increasing diffusion weighting. No signal contributions from blood in the STEAM case are noticeable. SNR efficiency maps of SE and STEAM for a single average obtained with a b-value of 450s/mm^2 are compared in **Figure 5.3 b)**.

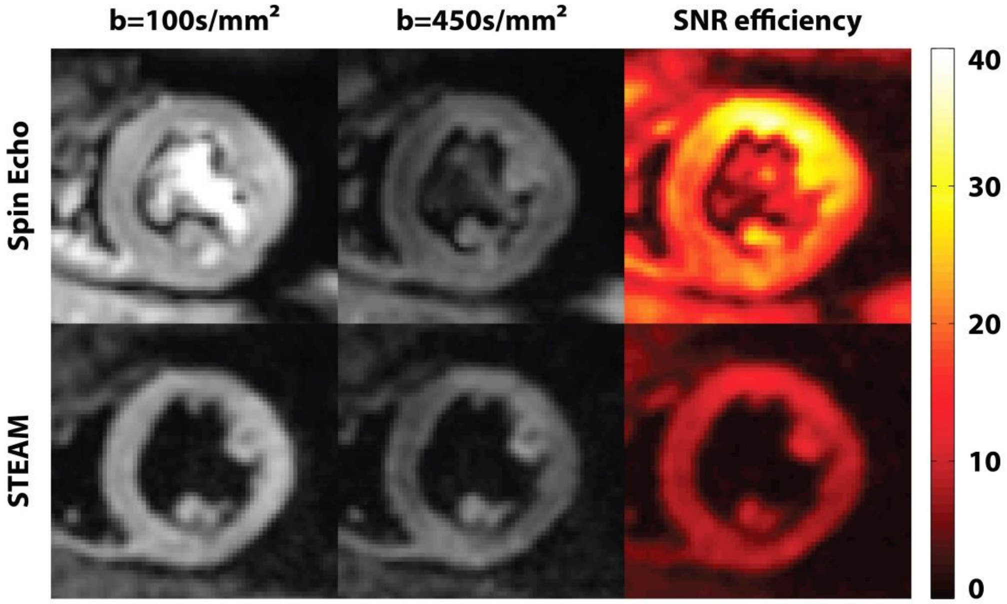

Figure 5.3 In vivo data. a) Example dataset acquired at b=100s/mm^2 and 450s/mm^2. b) Corresponding SNR efficiency maps for b=450s/mm^2.

SNR efficiency ratios SNR$_t$(SE/STEAM) per single average of the phantom and *in vivo* data are plotted in **Figure 5.4**. The data of the isotropic agar phantom yielded a mean ratio of 2.84±0.08, which agrees well with theory (theoretical SNR$_t$(SE/STEAM)=3.07) as shown in **Figure 5.4 a)**. While SNR$_t$(SE/STEAM) was independent of the b-value in the isotropic phantom, a distinct decrease of SNR$_t$(SE/STEAM) was measured in the anisotropic diffusion phantom. Here the ratio of SNR efficiency for SE versus STEAM was found to decrease from 2.75±0.05 to 2.20±0.13 when increasing the b-value from 50 to 450s/mm^2. The mean SNR efficiencies for the phantom measurements are listed

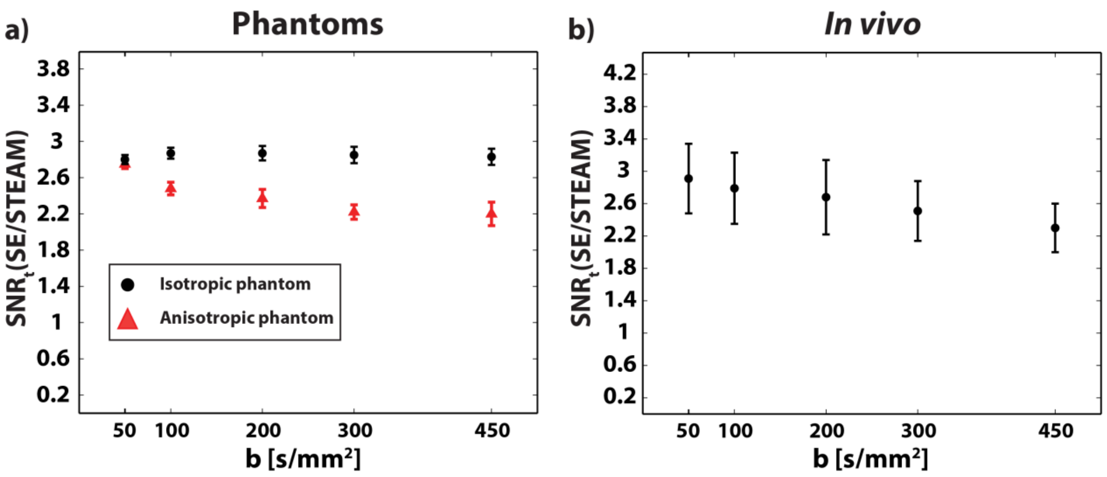

Figure 5.4 SNR efficiency ratios of isotropic agar and anisotropic diffusion phantom as well as of in vivo measurements are shown for b-values ranging from 50 to 450s/mm^2. a) While the isotropic agar phantom shows no b-value dependency, SNR$_t$(SE/STEAM) is seen to decrease with increasing diffusion weighting in the anisotropic diffusion phantom. b) In vivo data reveal b-value dependency of SNR$_t$(SE/STEAM) similar to anisotropic diffusion phantom.

in **Table 5.3** and **5.4**. Similarly, the *in vivo* data revealed a reduced SNR$_t$(SE/STEAM) with increasing b-value as shown in **Figure 5.4 b)**. The *in vivo* SNR efficiency ratios decreased from 2.91±0.43 to 2.30±0.30 when increasing the b-value from 50s/mm^2 to 450s/mm^2 (theoretical SNR$_t$(SE/STEAM)=3.46±0.45). The mean SNR efficiencies across all volunteers and b-values are listed in **Table 5.5**.

DTI Measurements

MD values obtained from SE data in the anisotropic diffusion phantom were found to be higher (1.58±0.10x10^{-3}mm^2/s) when compared to STEAM (MD$_{STEAM}$= 1.14±0.13x10^{-3}mm^2/s). Likewise FA values obtained with SE were lower (FA$_{SE}$=0.29±0.07) relative to STEAM (FA$_{STEAM}$=0.53±0.11).

In vivo DTI data was acquired within 10:16±4:40min:sec and 10:16±4:22min:sec for SE and STEAM, respectively. Data quality was assessed by calculating the percentage of negative eigenvalues. While 0.02±0.05% of the diffusion tensors derived from SE were found to have negative eigenvalues, STEAM resulted in 2.53±1.63%.

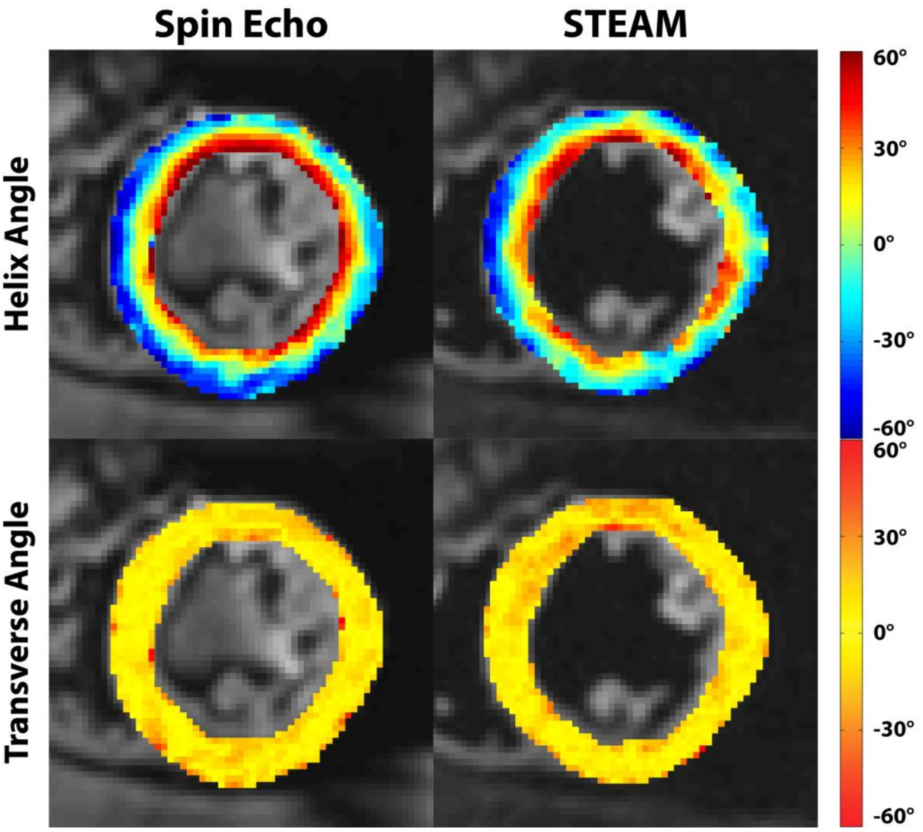

Figure 5.5 Helix and transverse angle maps. The linear decrease of helix angles from endo- to epicardium is visible, however more coherent in the SE case. Transverse angles are close to zero degrees for both sequences except for non-negative values at the intersection of left and right ventricular structures and near the papillary muscles.

In **Figure 5.5**, example helix and transverse angle maps are compared for SE and STEAM. A clear progression in helix angle from positive to negative values from endo- to epicardium can be observed. Reduced SNR in the STEAM case, however, causes patches with increased angle variations.

Statistics on helix and transverse angles across all volunteers for the anterior, septal, inferior and lateral segments are reported in **Figure 5.6**. The solid boxes and error bars correspond to the 50% and 90% percentiles of the helix angle distribution along the circumferential dimension. The linear dependency of the helix angles as a function of transmural depth is clearly evident for SE and STEAM. In the STEAM case, however, endo- and epicardial helix angles are found to be less steep with increased angle variation at the inferior-lateral region relative to SE. The root mean squared error (RMSE) of linear regression of the transmural helix angle distribution was found to be

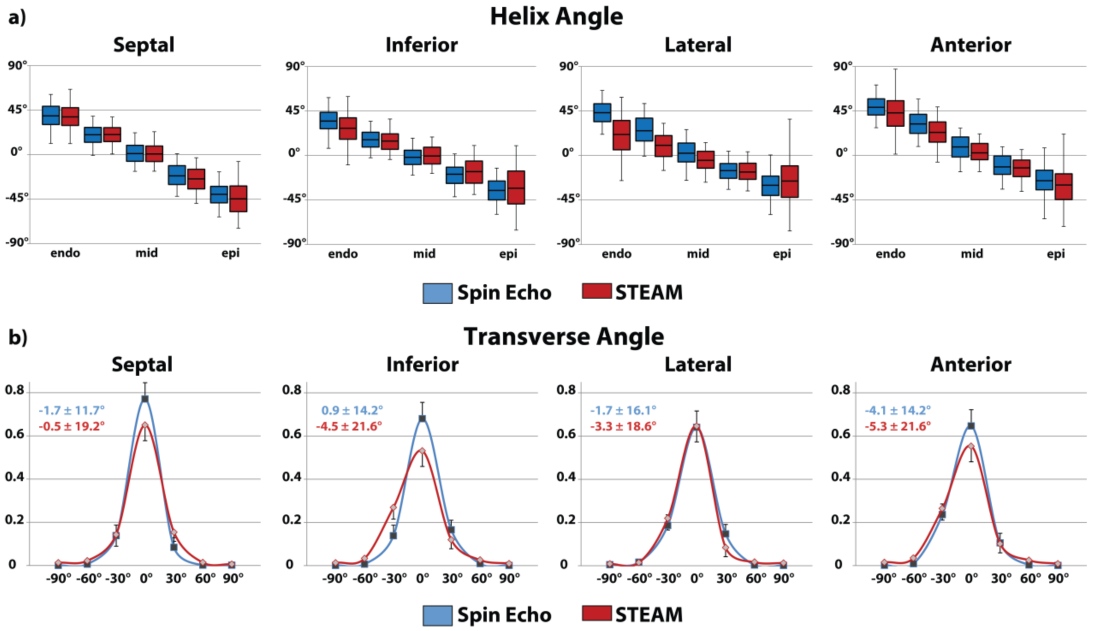

Figure 5.6 Sectorwise helix and transverse angle statistics. a) Comparison of transmural helix angle distribution for SE (blue) and STEAM (red) (solid box: 50% percentile, error bars: 90% percentile of the helix angle distribution in circumferential direction). Helix angle variations are more pronounced in STEAM, particularly at the endo- and epicardial region. b) Histograms of transverse angles show reduced dispersion of transverse angle for SE.

significantly reduced in SE versus STEAM (13.7±2.6° vs. 18.0±2.8°, p<0.01). The standard deviation of the transverse angles across all subjects and sectors was significantly smaller for SE compared to STEAM: (13.7±1.2° vs. 19.7±2.0°, p<0.01).

The reproducibility of MD and FA was determined by repeated acquisitions during one session. The average MD values were 1.43±0.06x10^{-3}mm^2/s for SE and 1.05±0.08x10^{-3}mm^2/s for STEAM. No statistically significant differences were found between repeated experiments for both SE and STEAM (SE: p=0.31, STEAM: p=0.10). However, differences for MD between SE and STEAM were statistically significant (p<0.001). Mean FA values over all volunteers were 0.38±0.02 for SE and 0.59±0.03 for STEAM with no statistically significant differences between repeated experiments (SE: p=0.91, STEAM: p=0.41) in each case. However, FA differences between the SE and STEAM were statistically significant (p<0.001). Corresponding Bland-Altman and line plots for the *in vivo* MD and FA values are shown in **Figure 5.7**.

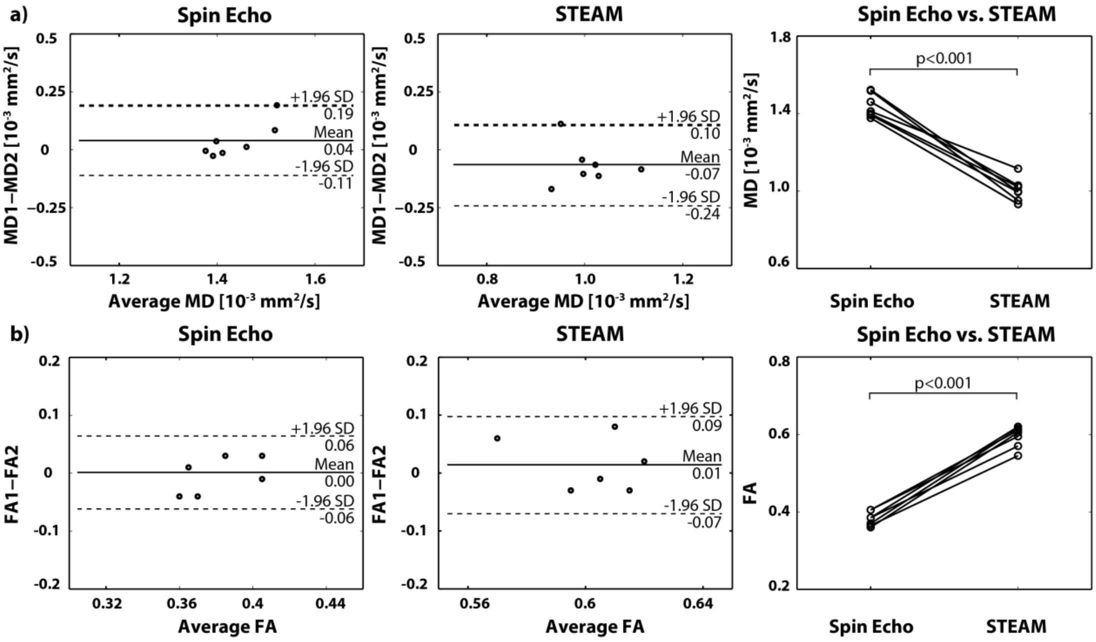

Figure 5.7 Bland-Altman and line plots of MD (a) and FA (b) representing intra subject reproducibility of SE versus STEAM. No statistical differences were observed between repeat measurements for MD and FA for both SE and STEAM. Significant differences were found for MD and FA between both sequences.

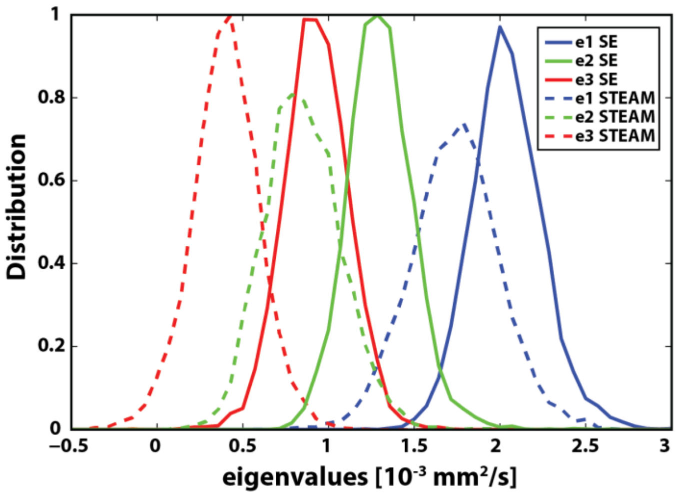

Figure 5.8 *Eigenvalue analysis. Diffusion tensor eigenvalue (e1, e2, e3) histograms for SE (solid line) and STEAM (dashed line). SE eigenvalues show a distinct and dense distribution, while STEAM eigenvalue histograms are broadened.*

Figure 5.8 shows the distribution of the first, second and third eigenvalues (e1, e2, e3) for SE and STEAM DTI data across all volunteers. The SE distributions show narrow, almost equally high distinct peaks, whereas the eigenvalue spectrum in the STEAM case is broadened. The small percentage of negative eigenvalues (e3) in the STEAM case can be appreciated as well. Furthermore, the maximums of the SE eigenvalue distributions are increased and less separate relative to STEAM, in agreement with the results for MD and FA.

5.4 Discussion

In this study the relative SNR gain of cardiac-triggered, motion-compensated SE diffusion tensor imaging with respect to STEAM has been demonstrated using both phantom and *in vivo* data. The SNR gain was found to improve the accuracy of diffusion metrics including helix and transverse angle maps.

At a b-value of 50s/mm^2 the measured SNR efficiency gain of 2.84 of SE vs. STEAM agreed well with theory in the phantoms. *In vivo*, the measured gain in SNR efficiency at the lowest b-value was smaller compared to theory (2.91±0.21 (*in vivo*) vs. 3.46±0.45 (theory)). This is attributed in parts to slice profile imperfections of the VERSE echo pulse (186) and partial volume effects through-slice *in vivo*. All SNR measurements were obtained from a single signal average. Thereby confounding factors due to image misregistration and phase correction for averaging of complex data were avoided. To facilitate these measurements, the slice thickness was increased to 16mm contributing to increased partial voluming.

While the ratio of SNR efficiency of SE vs. STEAM was found to be independent of the b-value in the isotropic agar phantom, decreasing values were measured with increasing b-value for both the anisotropic diffusion phantom and in the *in vivo* myocardium. This result is explained by differences in diffusion times ΔT (ΔT_{STEAM} = 1000ms vs. ΔT_{SE} = 25ms) (188,189). Assuming a mean diffusivity of 1.4x10^{-3}mm^2/s and diffusion times of 25ms for SE and 1000ms for STEAM, the diffusion length is approximately 15 and 90µm, respectively. In comparison, the thickness of cardiac myocytes is in the range of approximately 10-20µm (44,60). Hence, diffusion becomes restricted during STEAM encoding and diffusion induced phase distributions deviate from a Gaussian shape (114). The phase distribution in STEAM is expected to be stretched out along the fiber direction due to the long diffusion time and the lateral confinement by myofibers.

DTI data were acquired with a modified sampling method. Instead of acquiring a b=0s/mm^2 image, 3 directions with a b-value of 100s/mm^2 and 9 directions with a b-value of 450s/mm^2 were sampled. Thereby the effect of *in vivo* perfusion was reduced (115,159,183). Helix angle maps obtained with SE and STEAM revealed the expected linear decrease from endo- to epicardium in accordance with previous studies (33,37,38,79,162). However, STEAM data resulted in increased deviation from the linear function when compared to SE, in particular in the inferior-lateral region, which corresponds to areas of low SNR in the SNR efficiency maps. The drop in SNR is related to the distal positon of the inferior-lateral segment to the surface coils.

In this region of low SNR the helix angle range was found to be underestimated compared to SE. Transverse angles were measured close to zero degrees on average, describing the circumferential alignment of myofibers. The lower SNR of STEAM, however, caused a larger variation around zero when compared to SE.

In vivo results for MD and FA were reproducible and in accordance with literature values of the *in vivo* human heart (33,34,37,38,79,162). Significant differences in MD and FA were seen between *in vivo* STEAM and SE similar to previous results found in muscle tissue (188). The measurements in the anisotropic diffusion phantom confirmed these findings. While MD is higher in the SE case, FA is increased with STEAM. Increased fractional anisotropy FA_{STEAM} is represented by a broad separation of the eigenvalue distributions compared to a compact, distinct distribution pattern in the SE case.

By design, the total scan duration for breath-held SE and STEAM imaging was kept identical in this study. However, SE acquisitions are favored for time-efficient free-breathing acquisitions as demonstrated in the Appendix. In contrast, free-breathing STEAM imaging requires a very narrow respiratory gating window between the second (decoding) and first (encoding) heartbeat (37) hence reducing scan efficiency significantly relative to SE. As demonstrated in the Appendix, SE resulted in 30%

increased scan efficiency compared to STEAM while SNR and DTI results were in very good agreement with the findings from the breath hold measurements.

Acceleration-compensated spin echo cardiac DTI requires a high-performance gradient system to reduce TE to approx. 65-70ms for a b-value of 450s/mm^2. With the recent introduction of clinical MR machines with high-performance gradient systems, this requirement is expected to be met increasingly in the near future.

5.5 Conclusion

Cardiac diffusion tensor imaging using motion-compensated SE yields up to 2.9x increase in SNR efficiency relative to STEAM, which in turn translates to reduced deviation of helix and transverse angles from expected *in vivo* configurations. The SE method hence presents an attractive alternative to STEAM based approaches for cardiac diffusion tensor imaging of the *in vivo* heart on modern MR systems with high-performance gradients.

5.6 Appendix

Since the SE approach requires only one cardiac cycle to acquire a diffusion-weighted image (in contrast to two R-R-intervals for STEAM), the sequence is particularly suited for free-breathing navigator gated acquisition.

DTI acquisition was performed during free breathing with a navigator gating scheme as proposed by Nielles-Vallespin et al. (37) along 3 (b=100s/mm^2) and 9 (b=450s/mm^2) diffusion directions without a visual feedback system. Images were accepted if the first navigator of the STEAM sequence was within the acceptance window of 5mm and the second navigator had a relative displacement of less than ±0.5mm to the first one. The imaging parameters were identical to the parameters used for breath held imaging: resolution 2.8×2.8mm^2, slice thickness 8mm, FOV: 230×98mm^2, TE/TR(SE): 70ms/1-R-R, TE/TR(STEAM): 31ms/2-R-R, signal averages SE/STEAM: 16/8. Imaging was timed to

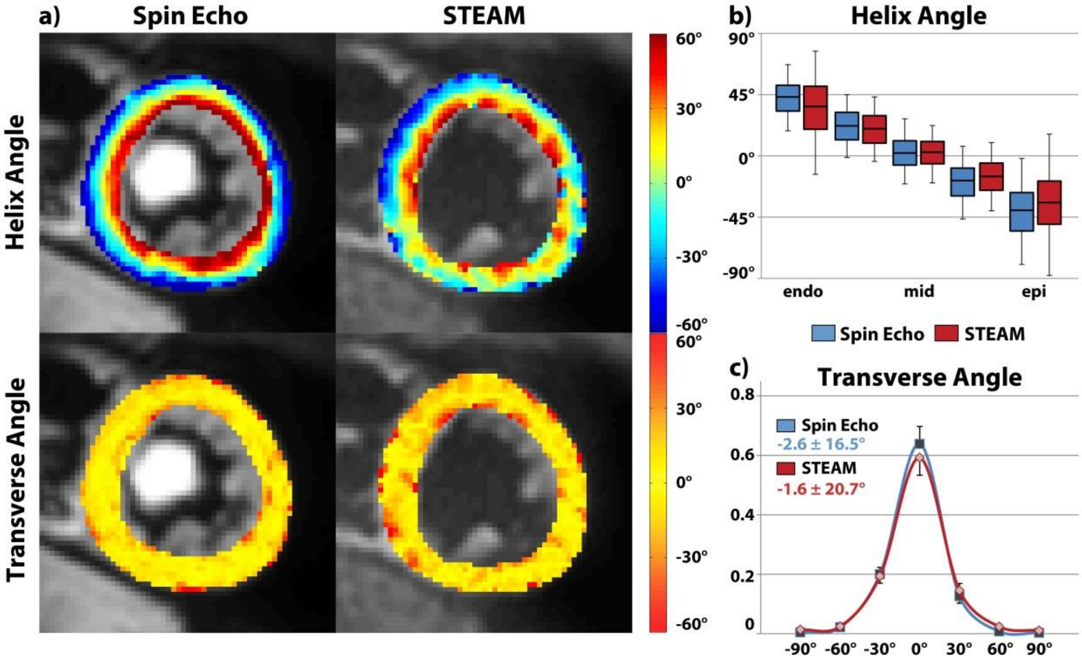

Figure 5.9 Free breathing acquisition: a) Helix and transverse angle maps. Similar to the breath hold case, the decrease of helix angles from endo- to epicardium is more coherent for SE. Transverse angles are close to zero degrees. b) Helix and transverse angle statistics: Comparison of transmural helix angle distribution for SE (blue) and STEAM (red) (solid box: 50% percentile, error bars: 90% percentile of the helix angle distribution in circumferential direction).

the systolic strain “sweet spot” (39). DTI analysis was performed based on mean diffusivity (MD), fractional anisotropy (FA), helix and transverse angles, the percentage of negative eigenvalues of the diffusion tensor and scan time efficiency. SNR was measured in a separate scan for b=50 and 450s/mm^2 along 6 diffusion directions (16mm slice thickness), 4 signal averages. DTI data reproducibility was not part of this sub-study.

SE based DTI data acquisition was 29% faster than STEAM for all volunteers (5:59±2:43min:sec vs. 8:28±2:56min:sec). **Figure 5.9 a)** shows an example helix and transverse angle map. Similar to the breath-hold acquisition (**Figure 5.5**), the helix map for STEAM shows patches with increased angle variations and less steep angles endo- and epicardially. A linear transmural change of helix angles can be seen in **Figure 5.9 b)**. Transverse angles were close to zero degrees with a significantly ($p<0.01$) wider spread in the STEAM (-1.6±20.7)° case compared to SE (-2.6±16.5)°. The RMSE of linear regression of the transmural helix angle distribution was significantly reduced in all cases for SE versus STEAM (15.9±3.7° vs. 19.8±4.2°, $p<0.01$). While 3.5±1.4% of the diffusion tensors derived from STEAM had negative eigenvalues, no negative eigenvalue was found in the SE case. FA values obtained with STEAM were significantly higher relative to SE (0.60±0.03 vs. 0.37±0.03, $p<0.001$) while MD values were lower for STEAM vs. SE ($1.01\pm0.06\text{x}10^{-3}\text{mm}^2/\text{s}$ vs. $1.49\pm0.15\text{x}10^{-3}\text{mm}^2/\text{s}$, $p<0.02$). Except for MD, all diffusion metrics fulfilled the requirements for t-testing. MD and FA were in accordance with breath hold and literature values (33,34,37,38,79,162). Similar to the breath hold measurements, the *in vivo* data shows a SNR_t(SE/STEAM) of 2.8±0.6 to 2.4±0.6 with increasing b-value from 50s/mm^2 to 450s/mm^2 (theoretical SNR_t(SE/STEAM)=3.4±0.5). In summary, free breathing DTI and SNR results are in very good agreement with the results from breath hold acquisitions of this work and similar to previous studies (37,38). In addition, scan time efficiency was significantly improved for SE compared to STEAM. Hence, besides the SNR benefit, free breathing navigator gating efficiency is increased when employing SE based DTI.

b [s/mm^2]	**SNR_t(SE)**	**SNR_t(STEAM)**	**SNR_t(SE/STEAM)**
50	49.19±0.35	17.59±0.28	2.80±0.05
100	43.81±0.39	15.27±0.31	2.87±0.06
200	36.18±0.49	12.61±0.30	2.87±0.08
300	28.76±0.37	10.08±0.29	2.85±0.09
450	20.86±0.32	7.37±0.21	2.83±0.09

Table 5.3 *Results of SNR efficiency of SE versus STEAM measured in isotropic agar phantom for different b-values.*

b [s/mm^2]	**SNR$_t$(SE)**	**SNR$_t$(STEAM)**	**SNR$_t$(SE/STEAM)**
50	9.40±0.12	3.42±0.06	2.75±0.05
100	7.89±0.27	3.18±0.05	2.48±0.07
200	6.52±0.31	2.75±0.14	2.37±0.10
300	5.59±0.44	2.52±0.15	2.22±0.08
450	4.49±0.61	2.04±0.23	2.20±0.13

Table 5.4 Results of SNR efficiency measured in anisotropic diffusion phantom.

b [s/mm^2]	**SNR$_t$(SE)**	**SNR$_t$(STEAM)**	**SNR$_t$(SE/STEAM)**
50	44.29±5.78	15.40±2.20	2.91±0.43
100	39.10±5.89	14.16±1.92	2.79±0.44
200	33.51±5.19	12.64±1.94	2.68±0.46
300	27.63±3.24	11.17±1.61	2.51±0.37
450	22.16±2.81	9.67±1.07	2.30±0.30

Table 5.5 Results of SNR efficiency of SE versus STEAM measured in vivo for different b-values.

Chapter 6

Studying Dynamic Myofibre Reorientation in Dilated Cardiomyopathy using *In Vivo* Magnetic Resonance Diffusion Tensor Imaging[*][‡]

6.1 Introduction

Dilated cardiomyopathy (DCM) is a major cause of heart failure, morbidity and mortality. Recent studies have reported that DCM is the third most common cause of heart failure and the primary indication for heart transplantation (190–192). It is a multifactorial disease encompassing hereditary and acquired forms (193). Though heterogeneous in aetiology, histologically most cardiac findings are non-specific, with hypertrophy and elongation of myocytes, reduced density of myofibrils, cellular necrosis, and fibrosis (194).

---

[*] Based on: Constantin von Deuster[†], Eva Sammut[†], Liya Asner, David Nordsletten, Pablo Lamata, Christian T. Stoeck, Sebastian Kozerke, Reza Razavi,"Studying Dynamic Myofiber Aggregate Reorientationin Dilated Cardiomyopathy Using In Vivo Magnetic Resonance Diffusion Tensor Imaging", Circulation Cardiovascular Imaging, in press

† equal contributors

[‡] The biomechanical modelling was performed by Liya Asner and David Nordsletten.

The clinical course is variable however progressive and largely irreversible. Clinically, the disease is characterised by advancing ventricular chamber enlargement and systolic dysfunction with patients developing breathlessness and oedema due to fluid retention and an increased risk of sudden cardiac death due to malignant arrhythmias (195,196). Over time, the heart becomes unable to compensate for the loss of contractile force and clinical manifestations become apparent (197). Pathophysiologically there is myocyte dysfunction and disarray, and activation of neurohormonal pathways to increase circulating blood volume resulting in a vicious cycle, ultimately leading to adverse cardiac remodelling and end organ damage (198). Despite developments in understanding and treatment approaches, the disease is not yet fully characterised and prognosis remains poor.

In recent years, the field of cardiac Magnetic Resonance (MR) Diffusion Tensor Imaging (DTI) has gained significant momentum. Quantitative information on the orientation of myocardial fibre aggregates from *ex vivo* DTI has been shown to correlate well with findings from histological studies (22,25,49,62,176). The integrity, mobility and arrangement of the myocytes contribute significantly to efficient ventricular function (76) and cardiac DTI has shown potential to gain novel insights into various cardiac conditions (29,30,47,48,50,51,54,87,180). Using diffusion sensitizing MR sequences, the displacement probability of diffusing water molecules within tissue of interest is measured (96). The resulting image information may be modelled by a diffusion tensor for each voxel. Based on the anisotropy of diffusion in tissue, the diffusion tensor can be used to characterise microstructural properties. The primary principal eigenvector of the diffusion tensor represents the mean myocyte direction and thus the arrangement of myocyte aggregates can be reconstructed. Scalar metrics such as mean diffusivity and fractional anisotropy allow characterisation of structural integrity (32,51,54).

The majority of cardiac DTI work has been performed *ex vivo* (24,26,31,48–51,54,55,66,67,176,199,200). In preclinical DCM models, alterations of the transmural helix angle of fibre bundles (28) along with increased diffusivity and decreased diffusion anisotropy have been described (27). One important shortcoming of *ex vivo* data is the deviation of mechanical load and systemic blood pressure from *in vivo* conditions. With advances in MR imaging methodology, *in vivo* cardiac DTI has been shown to be feasible and robust in animal and human studies (23,32–39,79,146,154,158,159). Moreover, the implementation of dual heart phase cardiac DTI now also permits insights into dynamic changes of myocardial fibre aggregates during the cardiac cycle confirming and complementing *ex vivo* studies in hearts fixated in diastolic or systolic states (62,80). *In vivo* dual heart phase DTI has been demonstrated both in healthy volunteers and patients with hypertrophic cardiomyopathy (8,35,42).

In general, cardiac DTI is technically challenging due to cardiac and respiratory motion. These issues are inherent to all cardiac imaging, however particularly critical in cardiac diffusion imaging where bulk motion is two to three orders of magnitude larger compared to displacements of diffusing water molecules. Hence, breathholding or dedicated navigator gating schemes are necessary to suppress respiratory motion induced signal loss (37). In addition, material strain due to cardiac contraction needs to be accounted for to avoid systematic errors in the diffusion metrics (38,39,163).

The objective of the present work was to study dynamic alterations of myocardial microstructure and strain in DCM patients using dual heart phase cardiac DTI and 3D MR tagging and compare the findings relative to data from age-matched healthy controls. Using biomechanical modelling, mechanistic insights into the underlying processes pertaining to differences in fibre reorientation during cardiac contraction in DCM patients versus controls are provided.

6.2 Methods

Study Protocol

Patients with non-ischaemic dilated cardiomyopathy were enrolled at St Thomas' Hospital, Kings College London. Criteria for DCM was left ventricular ejection fraction (LVEF) below 50%, no myocardial scar on previous cardiac MR, and a previous invasive coronary angiogram confirming unobstructed epicardial coronary arteries. Age-matched healthy volunteers without a history of cardiac events were enrolled as control group at the University Hospital Zurich. Imaging was performed on 1.5T Philips Achieva systems (Philips Healthcare, Best, The Netherlands) equipped with 32-channel cardiac receiver arrays at both sites. Written informed consent was obtained from all subjects prior to imaging, and the study protocol was approved by the ethics committees of Kings College London and the Canton of Zurich. Obtained informed consent included imaging as well as publication of anonymized data.

Prior to diffusion imaging, balanced steady state free precession (bSSFP) cine data (spatial resolution 2x2x15mm^3, temporal resolution 10ms) were acquired in two-chamber and short-axis view of the left ventricle (LV). On cine images, subject-specific mid-diastolic and peak-systolic time points were visually determined. To assess cardiac function, a contiguous stack of short-axis bSSFP cine images from apex to base was acquired during multiple breath holds (spatial resolutions 1.6x1.6x8mm^3, temporal resolution 30ms).

Diffusion Tensor Imaging

Diffusion-weighted imaging was performed in short-axis view orientation with a reduced field-of-view (FOV) technique (201) using stimulated echo acquisition mode (STEAM) imaging with single-shot echo planar image (EPI) readout (20). Since the diffusion-weighted imaging sequence spans over two consecutive heart beats, spatial position and diffusion encoding time are required to be identical in consecutive cycles. Therefore the imaging plane was placed at mid-ventricular level and the acquisition was ECG triggered to peak systole and mid diastole. Consistent levels of breath holding were ensured by respiratory navigator gating (gating window 5mm). Eight signal averages for each diffusion encoding direction were acquired within a single breath hold. A total of ten optimized diffusion directions were encoded (97) with a b-value of 350s/mm^2, resulting in 22 breath holds for two cardiac phases. Sufficient time to recover between the breath holds was allowed to avoid significant heart rate variations during data collection. To reduce echo time, crusher gradients necessary in STEAM were removed from the diffusion-weighted acquisitions, but kept for the "b=0s/mm^2" imaging. Parameters of the diffusion sequence were: field-of-view: 309×129mm^2, in-plane resolution: 2.5×2.5mm^2, slice thickness: 8mm, TE/TR 18ms/2 R-R intervals, partial Fourier factor 0.65.

Motion Imaging

Tissue motion and strain was quantified using three-dimensional complementary spatial modulation of magnetization (CSPAMM) tagged imaging, employing a segmented echo planar imaging readout (202). Three orthogonally oriented line tagged cine image volumes were acquired sequentially, covering the whole LV. Data acquisition was navigator gated (acceptance window 15mm) within three consecutive breath holds, each spanning over 18 heartbeats. Imaging parameters were as follows: field-of-view: $108x108x108mm^3$, spatial resolution: $3.5x7.7x7.7mm^3$, tag line distance: 7mm (EPI factor 7, 3 excitations per heart phase), temporal resolution: 20ms. Geometrical stack alignment of all tagged volume images was performed by incorporating navigator offsets and rigid image registration.

Data Analysis

Functional Analysis

Left and right ventricular volumes and ejection fractions, and left ventricular mass were calculated by manually drawing end-diastolic and end-systolic contours on short-axis images (excluding the papillary muscles) using commercially available software (CVI software, Circle Cardiovascular Imaging Inc., Canada). Left ventricular (LV) wall thickness was measured at end diastole and end systole in the mid LV, defined at the level of the papillary muscles.

Diffusion Tensor Analysis

In plane displacements of the diffusion-weighted images due to variations of breath hold levels were corrected by affine image registration prior to tensor calculation (147). Systolic and diastolic diffusion tensors were determined based on the Stejskal-Tanner equation, taking additional diffusion weighting of the “$b=0s/mm^2$” image acquisition due to crushers gradients into account. Systolic diffusion tensors were corrected for myocardial strain as previously reported (38,163). Upon tensor calculation, helix, transverse and sheet angles were computed. The helix angle α reflects the local helix elevation, i.e. the angle between the projection of the first eigenvector of the diffusion tensor onto the epicardial surface and the transmural

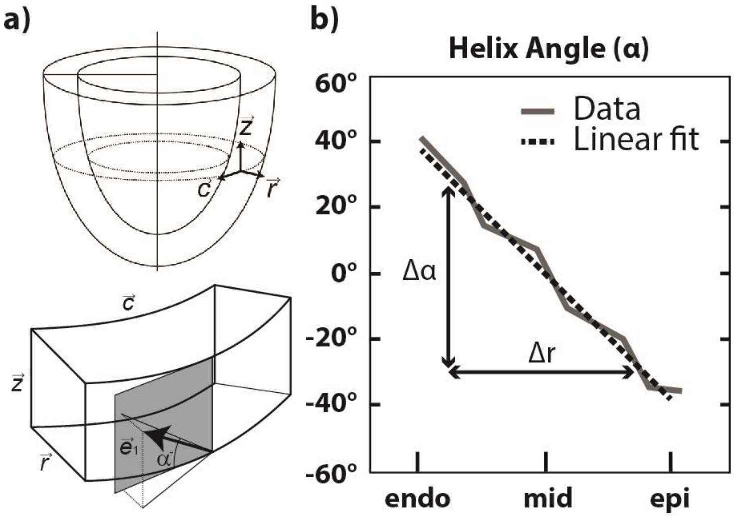

Figure 6.1 *a) Defintion of helix angle (α): The angle between the projection of the first eigenvector onto the epicardial surface and the transmural plane. b) Corresponding linear fit of the transmural course of the helix angles.*

plane. The transverse angle β denotes the deviation of the helix from the circumferential orientation and, accordingly, is defined as the angle between the projection of the first eigenvector onto the short-axis plane and the circumferential contour (**Figure 6.1 a)**). The E2A sheet angles were computed according to Ferreira et al. (30): Accordingly, the cross-myocyte plane perpendicular to the projection of the first eigenvector onto the epicardial surface ($E1_{proj}$) was determined for each voxel. Subsequently, the second eigenvector (E2) was projected onto this plane and the angle relative to the cross-myocyte direction (orthogonal to radial direction and $E1_{proj}$) was measured.

For each diffusion tensor, a locally normalized transmural position was calculated. Helix angles were binned along ten equidistant transmural positions on a per subject basis, followed by linear regression to determine the slope of the linear transmural helix angle course. To avoid partial voluming effects at the endo- and epicardial boundaries, data points from 80% of the inner myocardium were used for data fitting (**Figure 6.1 b)**). Helix angle ranges were computed as difference between subendocardial and subepicardial helix angle values. For each cardiac phase, mean and standard deviation across both groups was computed for MD, FA, helix angle slope and transverse angles.

Motion and Strain Analysis

On the 3D tagging data, endo- and epicardial contours of the LV were manually defined while excluding papillary muscles. Longitudinal, radial and circumferential strain were determined by contour tracking utilising the SinMod algorithm (TagTrack, GyroTools LLC, Zurich, Switzerland) (167). The time course of cardiac torsion was determined as proposed previously (75). It is defined as the difference in rotation angle between an apical and basal slice, normalized by their longitudinal distance. Circumferential and radial strains are given in the mid ventricular region. Longitudinal strain was computed across the whole LV. Additionally, 3D displacement fields were computed for diffusion tensor strain correction at a spatial resolution of 0.9mm isotropically.

Statistical Analysis

Differences between diastolic/systolic parameters and DCM patients/controls were determined by a Wilcoxon signed-rank and Wilcoxon rank-sum test, respectively. A p-value smaller than 0.05 was considered statistically significant.

Biomechanical Modelling[‡]

Two idealised geometric models of the left ventricle truncated at the base were created using the average measurements (end-diastolic long and short-axis lengths, wall thicknesses and cavity volumes). The two models represent an average of the control and DCM populations. Fibre distributions were chosen to match the average end-diastolic helix angle slopes observed in the respective cohorts. Passive inflation and active contraction of the ventricle were simulated using computational biomechanical models (203–205). The impact of dilatation and increased sphericity on the changes of helix angle slopes was explored and compared between the groups. Additionally, strain and torsion were measured in both models with varying helix angle slopes to investigate whether the changes in fibre orientation were in part responsible for the differences seen in these parameters. More details on the modelling methods are listed in the Appendix.

[‡] The biomechanical modelling was performed by Liya Asner and David Nordsletten.

6.3 Results

The final study cohort consisted of 9 DCM patients and 9 healthy volunteers. Demographics and clinical characteristics are shown in **Table 6.1**. The two groups were matched for age with no significant difference in body surface area and average heart rate at the time of scan. Compared to the control group, indexed left ventricular end-systolic volume (LV ESV) and LV mass were significantly greater in the DCM group and LVEF was significantly lower. There were no significant differences in LV end-systolic and end-diastolic wall thickness and end-diastolic volumes (LV EDV) between the groups.

DCM is clinically defined as systolic dysfunction and dilation of the ventricles. According to Codd et al. (206), the major diagnosis criteria for DCM is LVEF below 51%. Additionally, iLVESV and iLVEDV need to be at least two standard deviations greater than age and gender matched reference values from healthy subjects (207). As outlined in the Methods section, our patient selection criteria was LVEF<50% which translates in an average LVEF of 38±10% for the patient cohort. With the measured average end diastolic and end systolic volumes in the DCM patients (99.3±36.6 ml/m^2 and 62.2±25.5 ml/m^2) and corresponding reference values (76±9 ml/m^2 and 25±5.5 ml/m^2) for healthy controls (207), above diagnosis criteria are met.

The DTI data are summarized in **Table 6.2** and results of helix and transverse angle calculations as well as scalar diffusion metrics are reported below. Assuming an effective respiratory navigator efficiency of 30%, the total acquisition time for the DTI scans can be approximated as 17:15±3:05 min:sec for the patients and 18:37±2:04 min:sec for the control group.

	DCM	**Control**	p (DCM vs Control)
Male/Total	7/9	7/9	-
Age (years)	61±12	50±6	0.52
Heart rate (beats/min)	68±12	63±7	0.38
BSA (m^2)	1.8±0.2	1.8±0.2	0.75
iLV EDV (ml/m^2)	99.3±36.6	80.0±11.9	0.48
iLV ESV (ml/m^2)	62.2±25.5	31.2±5.1	<0.01*
LVEF (%)	38±10	60±4	<0.01*
iLV mass (g/m^2)	75±15	55±12	<0.02*
iRV EDV (ml/m^2)	75±28	78±16	0.40
iRV ESV (ml/m^2)	37±13	31±6	0.40
RVEF (%)	54±9	60±4	0.063
LV dia. wall thickness (mm)	8.9±1.3	8.9±0.9	0.96
LV sys. wall thickness (mm)	10.4±1.7	12.7±2.4	0.054

** denotes significance*

Table 6.1 *Demographics and functional data from patient and control group. BSA: Body Surface Area, iLV EDV/ESV: indexed Left Ventricular End Diastolic/Systolic Volume, EF: Ejection Fraction, iRV EDV/ESV: indexed Right Ventricular End Diastolic/Systolic Volume. Reported values are mean±standard deviation.*

			p		
	DCM	**Control**	DCM (dia vs sys)	Control (dia vs sys)	DCM vs Controls
Dia. HA slope (°/trans. depth)	-1.15±0.35	-0.79±0.11	0.89	<0.01*	<0.01*
Sys. HA slope (°/trans. depth)	-1.15±0.34	-1.06±0.12	-	-	0.90
Dia. HA range (°)	81±23	56±9	0.82	<0.01*	<0.02*
Sys. HA range (°)	81±23	76±8	-	-	0.97
Dia. TA (°)	-1±26	-2±17	0.82	0.43	0.40
Sys. TA (°)	0±29	-1±26	-	-	0.63
Dia. MD (x10^{-3}mm^2/s)	1.20±0.17	1.10±0.10	0.43	0.50	0.23
Sys. MD (x10^{-3}mm^2/s)	1.24±0.20	1.13±0.15	-	-	0.27
Dia. FA	0.56±0.05	0.62±0.06	0.36	0.30	<0.04*
Sys. FA	0.58±0.05	0.59±0.04	-	-	0.56

** denotes significance*

Table 6.2 *Diffusion tensor metrics from patient and control group. HA: Helix Angle, TA: Transverse Angle, MD: Mean Diffusivity, FA: Fractional Anisotropy. Reported values are mean±standard deviation.*

Helix angles

Figure 6.2 shows example helix angle maps for a control subject and DCM patient in diastole and systole. Histograms of transmural helix angle distributions for controls and DCM patients are displayed in **Figure 6.3**. A change towards steeper helix angles during contraction is seen in the control group, whereas reduced dynamic change between diastole and systole is observed in the DCM patients. Bin counts of diastolic helix angles close to zero degrees are reduced in DCM relative to healthy controls. The corresponding transmural helix angle slopes derived from linear regression are shown in **Figure 6.4**.

In diastole, the endo- and epicardial helix angles were higher in the DCM patients compared to controls (40±11° and -41±13° versus 26±6° and -29±7°, respectively). As a result, the diastolic helix angle slope was significantly steeper in the patients when compared to controls (-1.15±0.35 versus -0.79±0.11, $p<0.03$) with a significantly higher range of values from endo- to epicardium (81±23° versus 56±9°, $p<0.02$) in the DCM patients compared to the controls in diastole.

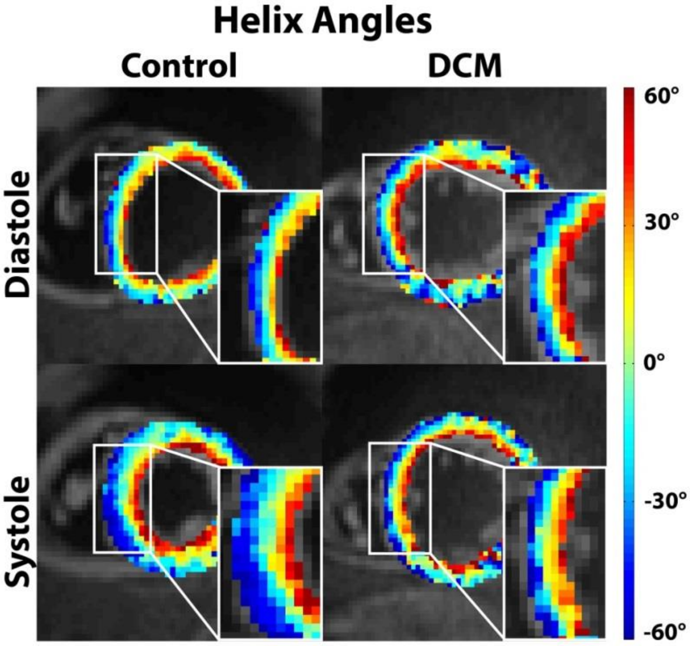

Figure 6.2 Comparison of helix angle maps acquired in diastole and systole from control versus DCM patient. A linear transition from positive to negative helix angles as a function of transmural depth is seen. While endo- and epicardial helix angles become steeper during systole in the healthy control, no explicit change between diastole and systole is found in the DCM case.

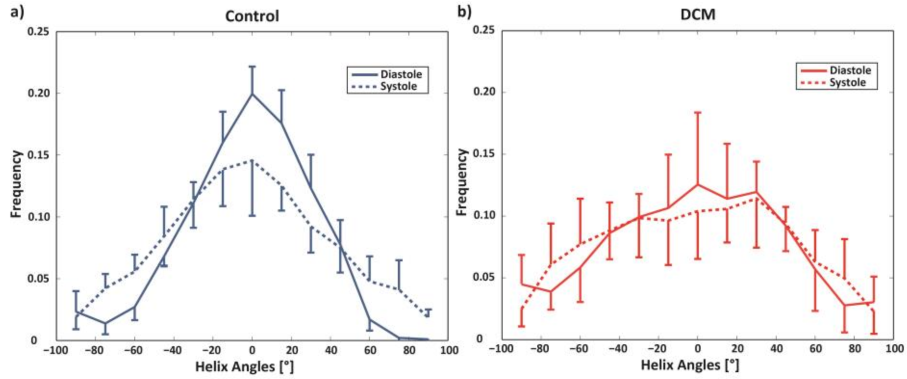

Figure 6.3 *Histograms of diastolic and systolic helix angles for controls (a) and DCM patients (b). While a shift towards steeper helix angles is seen in the systolic healthy heart, systolic and diastolic distributions are similar in the DCM case.*

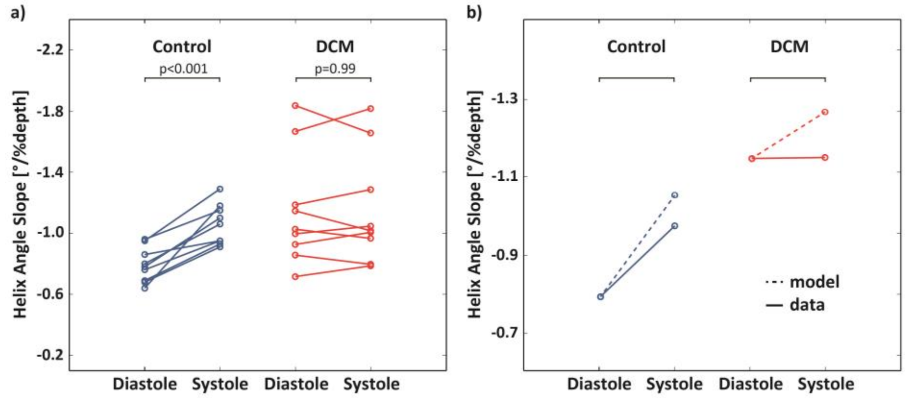

Figure 6.4 *a) Comparison of transmural helix angle slopes in diastole versus systole for the control and DCM groups. b) Diastolic and systolic helix angles for control and DCM modelling as compared to the data.*

In systole, there was a significant increase in maximum endo- and epicardial helix angle in the controls indicating a more longitudinal alignment of fibres with cardiac contraction. This resulted in a significant increase in helix angle slope in the control group from diastole to systole -0.79±0.11 to -1.06±0.12, p<0.01). In contrast, there was no significant change in helix angle slope from diastole to systole in the DCM patients (-1.15±0.35 to -1.15±0.34, p=0.89). The finding indicates that despite steeper endo- and epicardial helix angles in diastole in the patients there was significantly less longitudinal reorientation with cardiac contraction in the DCM patients than in healthy controls.

Transverse angles

The results for transverse angles are also shown in **Table 6.1**. The values are distributed around zero degrees indicating the expected alignment of the fibre aggregates along the circumferential direction. No significant differences were seen between diastole and systole or between groups.

Sheet angles

Histograms of E2A sheet angle distributions for controls and DCM patients are shown in **Figure 6.5**. A dynamic change in E2A angles towards a broader distribution during contraction is seen in the control group, whereas reduced dynamic change between diastole and systole is observed in the DCM patients. Bin counts of diastolic sheet angles close to zero degrees are reduced in DCM relative to healthy controls.

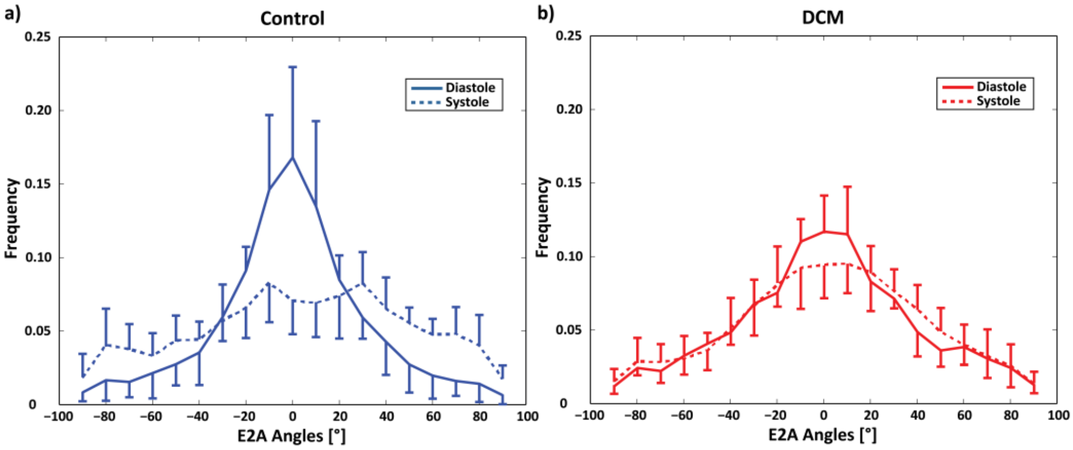

Figure 6.5 a) Histograms of diastolic and systolic E2A sheet angles for controls and DCM patients. The sheet angle distribution is broader in the systolic healthy heart compared to diastole, whereas systolic and diastolic distributions are similar in the DCM case.

Mean diffusivity (MD) and fractional anisotropy (FA)

In both diastole and systole, there was lower FA in the DCM group than in the controls which was statistically significant in diastole (diastole 0.56±0.05 versus 0.62±0.06 respectively, p=0.06; systole 0.58±0.05 versus 0.59±0.04 respectively, p=0.58). There were no significant differences in FA between cardiac phases in either group.

There was a trend towards higher MD in the DCM group relative to controls, however this was not statistically significant (diastole 1.20±0.17x10^{-3}mm^2/s versus 1.10±0.10x10^{-3}mm^2/s, p=0.10; systole 1.24±0.20x10^{-3}mm^2/s versus 1.13±0.15x10^{-3}mm^2/s, p=0.30). There were no significant differences in MD between cardiac phases in either group.

Torsion and strain

Figure 6.6 shows the mean torsional deformation normalized to long-axis length over the cardiac cycle. **Table 6.3** reports maximum torsion and strain for both groups. Longitudinal, circumferential and radial strains were all significantly reduced in the DCM group compared to the controls. Mean (systolic and diastolic) helix angle slope was correlated against maximum torsion, LVEF and longitudinal strain.

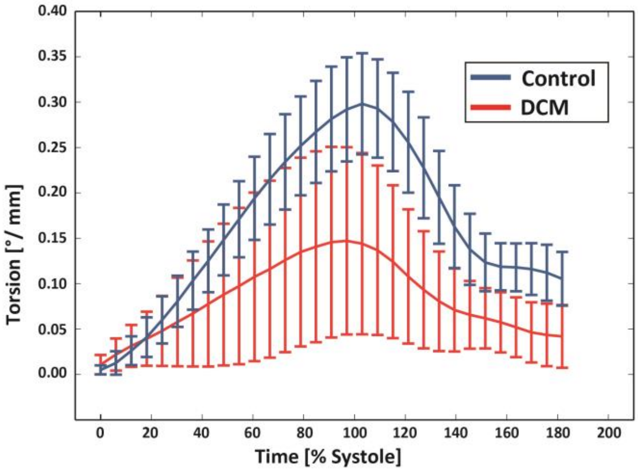

Figure 6.6 Time course of myocardial torsion for DCM and control. In DCM patients, torsion is reduced relative to the healthy controls.

	DCM	**Control**	p (DCM vs Control)
Max torsion (°/mm)	0.17±0.09	0.30±0.05	<0.02*
Max radial strain	0.11±0.05	0.16±0.03	<0.01*
Min circumferential strain	-0.12±0.04	-0.18±0.02	<0.01*
Min longitudinal strain	-0.11±0.03	-0.17±0.01	<0.01*

** denotes significance*

Table 6.3 Torsion and strain metrics for patient and control group. Reported values are mean±standard deviation

The correlations were found to be limited in both groups and are shown in **Figure 6.7**. In the DCM group, there was a trend towards reduced torsion and longitudinal strain with increased helix angle slope compared to controls. LVEF was found to remain on constant level of around 40% for helix angle slopes in the vicinity of 1.0°/% transmural depth, however decreased to 15% with increased helix angle slope.

In the control group, values for peak torsion were spread by approximately 15% around 0.30°/mm and the values for longitudinal strain were in the relatively small range of 0.15 and 0.19 for the controls compared to 0.07 and 0.17 for the DCM patients. Healthy LVEF values were densely distributed around 60±4%.

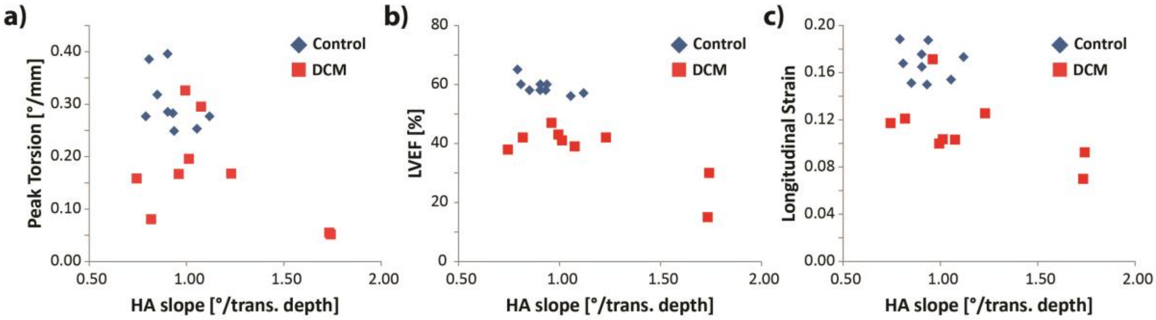

Figure 6.7 Peak torsion (a), left-ventricular ejection fraction (LVEF) (b) and longitudinal strain (c) as a function of normalized helix angle (HA) slope. A trend towards lower torsion (a), LVEF (b) and longitudinal strain (c) with increasing helix angle slope is seen in the DCM group.

Biomechanical modelling[‡]

The active contraction phase was simulated for the healthy and the DCM models to understand the differences in the helix angle changes between the end-diastolic and end-systolic states. Both models were progressively activated at respective end-systolic volumes, and the change in helix angle slopes at the endo- and epicardial surfaces was recorded. **Figure 6.4 b)** shows the results for the two models. The observation from the data that in controls the slope change is higher than in DCM patients is supported by the model.

[‡] The biomechanical modelling was performed by Liya Asner and David Nordsletten.

The next modeling objective was concerned with potential explanation of the observed changes in helix angles by the dilatation and remodeling seen in DCM hearts. To this end, the control LV was inflated from its reference volume to the DCM model reference volume. The angles at the larger volume are steeper, but the change is too low to explain the difference between the measured control and DCM helix angle slopes (**Figure 6.8**). The experiment was repeated for the DCM LV, which was inflated to twice the cavity volume resulting in 11°/% change. These values compare to 36°/% difference between average control and DCM slopes, as computed from the DTI data.

Lastly, we aimed to investigate whether the change in fibre angle was contributing to the reduced torsion and strain or whether this may minimize the reduction of motion parameters compared to normal fibre angles. The effect of changing ventricle size and shape was again considered separately from the effect of changing helix angles. There was consistently little or no change in strains and torsion due to change in initial helix angles, whereas the differences between the control and the DCM LV models were more pronounced. Using the models, an approximately twofold increase in torsion between patients and controls was observed (**Table 6.4**).

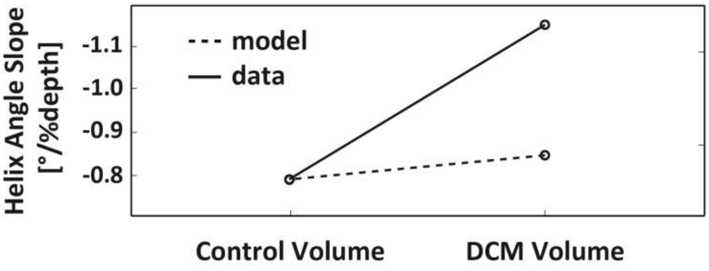

Figure 6.8 Change in helix angle slope caused by passive inflation of the control LV model to DCM model cavity volume as compared to measured difference in control and DCM helix angle slopes. Volume change alone does not explain observed differences between the two cohorts.

	DCM model	**Control model**
Max torsion (°/mm)	0.10	0.24
Max radial strain	0.23	0.41
Min circumferential strain	-0.10	-0.18
Min longitudinal strain	-0.06	-0.04

Table 6.4 Torsion and strain metrics for patient and control model.

6.4 Discussion

In this study, the dynamic change of myocardial fibre orientation in DCM patients and healthy controls was investigated using *in vivo* dual-phase cardiac diffusion tensor imaging. A statistically significant change of fibre orientation between diastole and systole was found in the control group. The longitudinal fibre alignment during contraction is assumed to optimize cardiac pumping efficiency and has been described previously using *in vivo* and *ex vivo* DTI data and histology (38,46,79–81). In contrast to healthy controls, the change in fibre and sheet angles from diastole to systole was found to be far less pronounced in DCM patients and was not statistically different between both heart phases. On average, diastolic fibre orientation with more longitudinal orientation in DCM patients relative to healthy controls was observed.

Seven out of nine DCM patients showed comparable systolic helix angle configurations relative to healthy controls. In the two remaining patients, however, clearly increased helix angle slopes in both cardiac phases were measured. It is speculated, that this elevated longitudinal fibre orientation could be the result of advanced remodelling as these two patients were considerably older (76 and 77 years) when compared to the mean age of the patient population (60±14 years). Accordingly, successive elongation of myocytes and reduced contractility may have been present. Similar reorientation was previously described by Tseng et al. (87) in hypertrophic hearts. However, more recent data seems to not confirm this finding (30).

Myocardial strain and torsion obtained in the DCM patients revealed reduced myocardial strain and impaired systolic torsion relative to controls. Our data on maximum torsion in DCM patients and controls is in good agreement with literature values (85). In general, cardiac pumping performance in the DCM patients was significantly reduced compared to the controls as quantified by a number of parameters: LVEF, maximum torsion, longitudinal, radial and circumferential strain. Particularly low LVEF, torsion and strain values were found for the two patients with elevated helix angle slopes.

As well as the clinical and gross structural changes seen in DCM, the results of fibre reorientation must be considered alongside well-recognised subcellular changes such as microarchitecture disarray. Histologically, heart failure is characterised by myocyte elongation, reduced myocyte density and fibrosis and these changes have been correlated with *ex vivo* DTI results in previous studies (17,27). Though histological examination was not possible in our cohort of patients the trend towards an increase in mean diffusivity and decrease in fractional anisotropy supports the presence of reduced myofibril density and cellular necrosis where water is able to diffuse more freely.

A feature of the present study was the ability to investigate the changes seen from the MR data using biomechanical modelling. This was two fold – firstly to try to understand whether the size and/or shape of the ventricle could be responsible for the altered steepness of the fibres in diastole, and secondly to understand the implications of the alterations in particular whether they appear to be beneficial or counter-productive to efficient cardiac contraction.

Our initial tests showed that the dilatation of the heart is not sufficient to produce the observed differences in fibre angle between the groups. We achieved more similar results when using a dilated, more spherically-shaped heart.

We also sought to understand if the reorientation of the fibres may minimise or exacerbate the reduction in strain and torsion seen in the remodelled ventricle. The results show that the reduction in longitudinal strain and torsion appear to be exacerbated by steeper fibre angles and that this is regardless of the LV model used suggesting that this factor is independent of the changes to LV size and shape. Accordingly, even in a dilated and remodelled heart the steeper angles are not beneficial to maintaining longitudinal, radial or circumferential strain or torsion.

The underlying reasons for exacerbated deterioration in strain and torsion with these fibres may reflect underlying subcellular changes that could not be examined in this study. Efficient excitation-contraction (E-C) coupling relies on local control of calcium ion release between voltage-gated channels found on T-tubules and receptors on the sarcoplasmic reticulum (SR) on the myocytes. Normally, the T-tubule network is highly organised in relation to the SR and this permits co-ordinated contraction for maximal contractile force with least energy cost. A number of studies (208–210) have shown that in ventricular tissue or individual myocytes in models of heart failure, there is dilatation and decreased density of T-tubules with disorganisation of the T-tubule network pattern. Reorientation of the cardiac fibres may be related to this phenomenon and would need to be examined alongside future DTI work in this cohort to fully appreciate the interplay between these aspects.

Interestingly we also show that there is little or poor correlation with any of the single parameter tested against the change in helix angle slope in the subjects studied. This suggests that a composite of factors such as dilatation, sphericity, poor systolic function and the recognised other subcellular alterations seen in DCM may be responsible for this structural rearrangement. Further studies would be needed to confirm this and may be a future area of study.

In summary, we have been able to demonstrate that there are changes in the diastolic orientation of cardiac fibres and, importantly, that there is reduced and inconsistent dynamic reorientation of the fibres during cardiac contraction in DCM patients relative to healthy hearts. We have been able to show that the remodelling of the heart appears to be an important factor in the changes of fibre orientation but have also demonstrated that the change in shape does not explain the difference seen in helix angle slope between DCM patients and controls. We have also demonstrated that steeper fibres are coupled with a worsening in the strain and torsion observed. Overall, our findings provide new insights into the structural alterations within the living heart in DCM and underline the importance of MR diffusion tensor imaging to gain deeper understanding of cardiac disease.

Study Limitations

The DCM patient cohort in this study had a diagnosis of non-ischaemic cardiomyopathy however the aetiology may be heterogeneous. Clinical, morphological and functional data were variable and, accordingly, a large variation of helix angle distribution was seen.

Because of scan time constraints, the imaging resolution of cardiac DTI was relatively coarse ($2.5x2.5x8mm^3$) and hence partial voluming effects were inherently present at the endo- and epicardial borders. To reduce the impact of this, edge voxels were excluded from the analysis. In line with the limited scan time available, only one slice could be acquired using cardiac DTI.

6.5 Conclusion

Diffusion tensor imaging has revealed reduced and inconsistent dynamic reorientation of fibres during cardiac contraction in DCM patients relative to healthy hearts. Remodeling of the heart appears to be an important factor in the changes of fibre orientations. Steeper fibres are coupled with a worsening in strain and torsion. Overall, the findings provide new insights into the structural alterations in DCM patients.

6.6 Appendix[‡]

Overview of the biomechanical model

The biomechanical model is based on the classical continuum approach combined with finite element discretisation. This supplement provides a brief overview of the mathematical and computational model. Further particulars of the model and methods used can be found in (204,211).

Let the reference configuration of the myocardium be denoted by Ω_0 with the coordinate $\boldsymbol{X}$, and a deformed configuration at time $t \in (0,T]$, $T>0$, be denoted by Ω_t with the coordinate $\boldsymbol{x}$. At a given time t domain deformations can be defined as $\boldsymbol{u} = \boldsymbol{x} - \boldsymbol{X}$, while the hydrostatic pressure and the boundary tractions (described below) are denoted by p and $\boldsymbol{\lambda}$ respectively. The principle of stationary potential energy (212) states that at any time t this deformation can be found by minimising the total energy of the system:

$$\Pi(\boldsymbol{u},p,\boldsymbol{\lambda}) = \inf_v \sup_{q,\mu} \Pi(\boldsymbol{v},q,\boldsymbol{\mu}).$$

[‡] The biomechanical modelling was performed by Liya Asner and David Nordsletten.

The total energy can be separated into internal and external energy terms:

$$\Pi = \Pi_{int}(\mathbf{u},p) + \Pi_{ext}(\mathbf{u},p,\boldsymbol{\lambda}).$$

We assume that myocardium can be modelled as a hyperelastic incompressible tissue, so that the internal energy can be written in terms of the strain energy function Ψ, the hydrostatic pressure p and the determinant of the deformation gradient $J = det(\mathbf{F})$, where $\mathbf{F} = \nabla_{\mathbf{X}}\mathbf{u} + \mathbf{I}$, and $\mathbf{I}$ is the identity matrix:

$$\Pi_{int} = \int_{\Omega 0}\Psi + p(J - 1)\, d\mathbf{X}.$$

The strain energy function incorporates orthotropic passive and active behaviour of the tissue:

$$\Psi = \Psi_p + \Psi_a.$$

The model employs the Holzapfel-Ogden passive constitutive law (213), defined as follows:

$$\Psi_p = a / (2b) \exp[b(I_1 - 3)] + \textstyle\sum_{i=f,s} a_i\ / (2b_i) (\exp[b_i(I_{4i} - 1)^2] - 1) + a_{fs} / (2b_{fs}) \exp[b_{fs}\, I_{8fs}^{\ 2}],$$

where $a, b, a_f, b_f, a_s, b_s, a_{fs}, b_{fs}$ represent material parameters (values given in Table S2 below), and $I_1, I_{4f}, I_{4s}, I_{8fs}$ are the strain invariants associated with fibre and sheet directions. Specifically, if at a given location in the reference domain the myocyte aggregate (referred to as fibre in the model) and sheet orientation vectors are $\mathbf{f}_0$ and $\mathbf{s}_0$ respectively, and $\mathbf{C} = \mathbf{F}^T\, \mathbf{F}$ is the right Cauchy-Green strain tensor, then

$$I_1 = \mathbf{C} : \mathbf{I}, \quad I_{4f} = \mathbf{f}_0 \cdot (\mathbf{C}\, \mathbf{f}_0), \quad I_{4s} = \mathbf{s}_0 \cdot (\mathbf{C}\, \mathbf{s}_0), \quad I_{8fs} = \mathbf{f}_0 \cdot (\mathbf{C}\, \mathbf{s}_0).$$

Active response is produced with a simplified version of Kerchoffs-type length-dependent constitutive laws (214,215) with reference myocyte compressive strain l_0=0.8, global active tension value AT, and added transverse activation at 30% of the fibre activation as discussed in (205,216):

$$\Psi_a = AT \int_0^{I4f} \tanh(2(\surd\xi\text{-}l_0))\, d\xi + 0.3\ AT \int_0^{(I1\text{-}I4f)} \tanh(2(\surd\xi\text{-}l_0))\, d\xi.$$

The external energy Π_{ext} comes from any forces acting on the boundaries of the domain. Ventricular cavity volume is set via an endocardial energy term

$$\Pi_{endo} = \lambda_{endo}(V - V_{data}),$$

where λ_{endo} is a scalar endocardial Lagrange multiplier representing cavity pressure, V the cavity volume produced by the simulation, and V_{data} the prescribed cavity volume. The cavity volume can be approximated as follows (204):

$$V = -\int_{\Gamma_{endo}} 0.5\, [(\mathbf{I} - \mathbf{n}_b \otimes \mathbf{n}_b)\, \mathbf{x}] \cdot \mathbf{n}\, d\mathbf{x},$$

where Γ_{endo} denotes the deformed configuration of the endocardial surface of the ventricle, $\mathbf{n}_b$ is the base normal vector and $\mathbf{n}$ the outward endocardial normal vector.

A simpified base condition allowing sliding in plane only was imposed due to the generic nature of the model. The base plane was aligned with the z = 0 plane, and the centre of the base coincided with the origin. The external energy term on the base could be written as follows:

$$\Pi_{base} = \int_{\Gamma base} \lambda_{base}\, (\mathbf{u} \cdot \mathbf{n}_b)\, d\mathbf{x} + \lambda_{0,1} \int_{\Gamma base} u_1\, d\mathbf{x} + \lambda_{0,2} \int_{\Gamma base} u_2\, d\mathbf{x} + \lambda_2 \int_{\Gamma base} u_1 \cdot x_2\, d\mathbf{x},$$

where Γ_{base} denotes the deformed configuration of the base surface of the ventricle, λ_{base} is a spatially varying Lagrange multiplier enforcing no longitudinal motion of the base plane, $\mathbf{n}_b$ is the base normal vector, $\lambda_{0,1}$ and $\lambda_{0,2}$ are scalars ensuring no translation of the base centre, and λ_2 is a scalar enforcing no rotation around the axis.

With this definition of the energy terms, and combining all Lagrange multipliers in a vector $\boldsymbol{\lambda}=(\lambda_{endo},\lambda_{base},\lambda_{0,1},\lambda_{0,2},\lambda_2)$, the full state of the system $(\mathbf{u},p,\boldsymbol{\lambda})$ at a given time t is found as the critical point of the total energy Π:

$$D_{(\mathbf{u},p,\boldsymbol{\lambda})}\, \Pi(\mathbf{u},p,\boldsymbol{\lambda}) = 0.$$

This equation provides the weak form of the problem, which can be solved numerically using the finite element method. The reference domain is discretised into quadratic hexahedral elements, with Q2-Q1 approximation for the displacement-pressure pair, quadratic approximation on quadrilateral surface elements for λ_{base}, and constant approximations for λ_{endo}, $\lambda_{0,1}$, $\lambda_{0,2}$ and λ_2. The resulting nonlinear system is solved via Newton-Raphson iteration with line search, with linear solve steps carried out by direct matrix inversion.

All simulation results were obtained using *C*Heart (217), a parallel multiphysics software engine.

Test specifications

Two reference geometries were produced: one to represent a generic healthy ventricle, and another to represent a generic DCM ventricle. Both shapes were simplified as ellipsoids cropped in the short axis plane below the base of the ventricle. The shapes were adjusted in such a way that passive inflation to prescribed end-diastolic volume produced representative short and long axis dimensions and wall thickness. The prescribed cavity volume, both at end diastole and end systole, was set to values lower than the data averages to account for ventricle truncation. The end-systolic state for each geometry was obtained by prescribing end-systolic volume, and gradually increasing active tension in the tissue to reach end-systolic cavity pressures of ~100 mmHg. It should be noted that the ventricle dimensions, as well as the HA/E2A values undergo significant changes at the first few activation steps ($AT < 25$ kPa), and then stabilise, meaning that the precise cut-off pressure (with $AT > 100$ kPa) has virtually no effect on these measurements. The prescribed and observed metrics are presented in **Table 6.5.**

Parameters used in passive inflation (given in **Table 6.6**) were based on values obtained for a healthy volunteer in [11]. Further, the values of the stiffness parameters a, a_f, a_s, a_{fs} were scaled to produce realistic end-diastolic pressures (10-15 mmHg) and ventricle dimensions similar to those observed in the data.

	Control			DCM		
	Reference state (REF)	End diastole (ED)	End systole (ES)	Reference state (REF)	End diastole (ED)	End systole (ES)
Cavity vol., ml	50	92	37	82	162	100
LA, cm	6.40	7.74	7.35	6.40	7.58	7.15
SA, cm	4.20	5.13	3.53	5.40	6.83	5.74
WT, mm	12.0	8.9	11.6	12.0	8.5	10.0

Table 6.5 Dimensions of the idealised geometrical models used in simulations (LA/SA – long/short axis length, WT – wall thickness). Low cavity volumes are the result of ventricle truncation. Cells with grey/white background show metrics that were prescribed/obtained using simulations.

	a, kPa	b	a_f, kPa	b_f	a_s, kPa	b_s	a_{fs}, kPa	b_{fs}
Control	0.24	3.0	4.80	4.0	0.96	1.5	0.4	3.4
DCM	0.60	3.0	6.40	4.0	1.28	1.5	0.6	3.4

Table 6.6 Parameters of the Holzapfel-Ogden constitutive law used in the simulations.

Chapter 7

Simultaneous Multi-Slice Diffusion Tensor Imaging of the *In Vivo* Human Heart[*]

7.1 Introduction

Stimulated echo acquisition mode (STEAM) imaging has been established as primary method for *in vivo* diffusion-weighted imaging of the beating heart (20,37–39,79,87,158,162,163). The STEAM technique, however, suffers from inherently low signal-to-noise ratio (SNR) due to the echo signal formation and the long mixing time (~1R-R interval). Imaging at high field strengths (3T), parallel imaging methods and multiple signal averaging have been used to address these limitations, but full 3D coverage of the *in vivo* human heart still requires very long scan times. As the STEAM sequence spans over two consecutive heart beats, breath holding or respiratory navigator gated free breathing methods (37) are necessary, which hampers the translation of the STEAM approach into a clinical setting (16,29,30,180).

---

[*] Based on: Constantin von Deuster, Christian T. Stoeck, Daniel Giese, Jack Harmer, Rachel W. Chan, David Atkinson, Sebastian Kozerke. "Concurrent dual-slice cardiac DTI of the in-vivo human heart", Proceedings of the 21st Meeting of ISMRM, Salt-Lake City, USA, 2013

Constantin von Deuster, Christian T. Stoeck, Martin Buehrer, Jack Harmer, Rachel W. Chan, David Atkinson, Sebastian Kozerke. "Free-breathing cardiac DTI with simultaneous multi-slice excitation", Proceedings of the 22nd Meeting of ISMRM, Milan, Italy, 2014

An attractive approach to accelerate diffusion-weighted imaging in the heart is simultaneous multi-slice (SMS) imaging. Multiple slices are acquired concurrently using multi-band excitation in combination with dedicated image reconstruction methods. Several approaches have been proposed for SMS imaging using Wideband (218,219), Simultaneous Image Refocusing (SIR) (220,221) and Parallel Imaging (PI) (222–225) reconstruction methods.

The Wideband technique can lead to severe voxel tilting artifacts and hence image blurring, whereas the SIR method extends the readout duration, increasing echo planar imaging (EPI) distortions and signal loss due to off-resonance effects and prolonged echo time (TE), respectively. SMS imaging with parallel imaging acquisition does not suffer from the aforementioned drawbacks. However, the final SNR depends on the geometry-factor which is directly related to the coil configuration and the undersampling factor and pattern (125). The conditioning of the reconstruction process can be improved by inducing an inter-slice image shift along the phase encoding direction using alternating RF pulses (222) or short blip gradients along the slice selection direction during EPI image readout (225). This approach is termed “Controlled Aliasing In Parallel Imaging Results In Higher Acceleration” (CAIPIRINHA) (222).

The objective of the presented work is to accelerate STEAM based cardiac DTI by concurrent dual-slice imaging and controlled aliasing in parallel imaging (222,225). Magnitude images and diffusion metrics for dual-slice short-axis acquisitions are presented and compared to sequential single-slice acquisitions.

7.2 Methods

Study Protocol

Cardiac STEAM diffusion-weighted imaging was implemented on a 1.5T Philips Achieva System (Philips Healthcare, Best, The Netherlands) equipped with a 32-channel cardiac receiver array. Prior to diffusion imaging, cine data with a temporal resolution of 10ms were acquired in two-chamber and short-axis view orientations. Systolic quiescent time points were determined visually on a per subject basis. Data were acquired in six healthy subjects without history of cardiac disease (4 male, weight 65.0±10.1kg, age 26.7±6.5years, heart rate 61.0±5.7beats/min). Written informed consent was obtained from all subjects prior to imaging. The study protocol was approved by the ethics committee of the Canton of Zurich.

Diffusion Imaging Sequence

Diffusion-weighted imaging was performed with a reduced field-of-view (FOV) technique (201) (**Figure 7.1**). The sequence was ECG triggered to the systolic strain “sweet spot” (39) and diffusion encoding was performed by unipolar gradients along ten optimized (97) directions (b-value: 400s/mm^2).

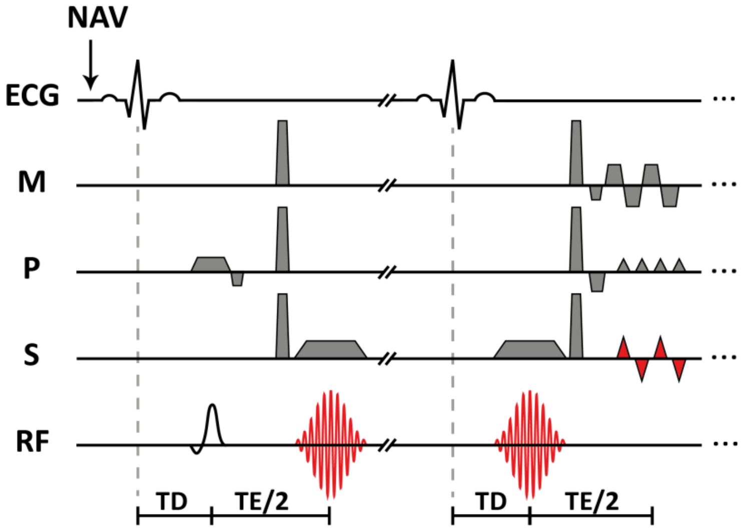

Figure 7.1 ECG-gated diffusion-weighted multi-band sequence with single-shot EPI readout. Dual-band RF pulses and CAIPIRINHA blips are shown in red.

The imaging parameters were as follows: resolution 2.5×2.5mm^2, slice thickness 8mm, Field of View (FOV): 200×100mm^2, TE: 16ms, TR: 2-R-R-intervalls, partial Fourier sampling (65 %). Fat suppression was achieved by frequency-selective saturation prior to the first 90° excitation. To ensure consistency of breath hold levels, respiratory navigator gating was used with a 1D navigator placed on the right hemi diaphragm (gating window: 5mm). For each diffusion encoding direction, eight signal averages were acquired within one breath hold (BH). The phase encoding direction was parallel to the chest wall to avoid aliasing of the bright chest wall and the heart. Compared to an anterior-posterior phase encoding direction, this orientation is also favorable with respect to coil sensitivity variation facilitating the unfolding process.

The Shinnar-Le Roux algorithm (226) was used for RF-waveform realization, generating two passbands corresponding to two slices with a slice thickness of 8mm and a stopband corresponding to a slice gap of 26mm (passband ripple: 0.01, stopband ripple: 0.01). The slice profile of the dual-band pulse was measured and compared to a numerical Bloch simulation.

Controlled aliasing was performed by a half FOV shift of one of the two slices (222,225). According to the Fourier shift theorem, a linear phase $\varphi(\mathrm{m}) = \mathrm{m}\,\Delta\,\mathrm{k}\,\Delta y$ in k-space corresponds to an offset Δy in image domain $\rho(\mathrm{y})$:

$$\rho\left(y+\Delta y\right)=\sum_{m=-N/2}^{N/2} S\left(m\Delta k\right)\exp(\mathrm{im}\,\Delta\,\mathrm{k}\,\Delta\,\mathrm{y})\exp(\mathrm{im}\,\Delta\,\mathrm{ky}) \tag{7.1}$$

with $\Delta k = 2\pi / FOV$ as the k-space spacing between N equidistant k-space lines and $S(k)$ the complex k-space signal. For an image shift by half FOV along the phase encoding direction, the linear phase ramp simplifies to: $\varphi(m) = m\pi = \pi, 0, \pi, 0, \ldots$ i.e. an alternating phase difference of π and 0 between both slices. This additional phase was generated for every second phase encoding line by alternating gradient blips along the through-slice direction (**Figure 7.1**) as proposed by Setsompop et al. (225).

Upon completion of the multi-band imaging, the diffusion imaging protocol was repeated as sequential single-slice acquisition for both slices during 22 breath holds. The same respiratory navigator gating window was used for accelerated and non-accelerated data acquisition to ensure geometric consistency among diffusion data collection.

Image Reconstruction

As no in-plane undersampling was performed, two voxels originating from the two slices fold onto each other forming an aliased image I_x for coil *x* according to:

$$\begin{pmatrix} I_1 \\ \vdots \\ I_{32} \end{pmatrix} = \begin{pmatrix} C_{1,1}(\mathrm{x},\mathrm{y}) & C_{1,2}(\mathrm{x},\mathrm{y}+\Delta\,\mathrm{y}) \\ \vdots & \vdots \\ C_{32,1}(\mathrm{x},\mathrm{y}) & C_{32,2}(\mathrm{x},\mathrm{y}+\Delta\,\mathrm{y}) \end{pmatrix} \cdot \begin{pmatrix} M_1(\mathrm{x},\mathrm{y}) \\ M_2(\mathrm{x},\mathrm{y}+\Delta\,\mathrm{y}) \end{pmatrix} \tag{7.2}$$

where *C* denotes coil sensitivity and *M* the unaliased image voxels. The coil sensitivities were determined by a separate b=0s/mm^2 sensitivity scan during one additional breath hold per slice. The imaging parameters were identical to the DTI scans, however slice thickness was doubled to 16mm to increase SNR.

The reconstruction algorithm was implemented in Matlab (MathWorks, Natick, MA) which solves eq. (7.2) in a least squares sense. The g-factor corresponding to the index i of the folded pixel reads (125):

$$g_{ii} = \sqrt{[(\mathrm{C}^H\mathrm{C})^{-1}]_{ii}[(\mathrm{C}^H\mathrm{C})]_{ii}} \tag{7.3}$$

It scales the SNR according to:

$$SNR_{CAIPI} = \frac{SNR_{full}}{g} \tag{7.4}$$

SNR_{full} refers to the SNR of a fully sampled sequential acquisition.

Data analysis

Consistent phase alternation of 0 and π between two consecutive k-space lines was ensured by an off-centre dependent phase correction during image reconstruction. Diffusion-weighted images were aligned to the b=0s/mm^2 image using affine image registration (elastix toolbox (147)). Diffusion tensors were calculated taking the diffusion weighting of the crusher gradients of the “b=0s/mm^2” image into account. Thereupon helix angles (HA) and transverse angles (TA) were derived (22). The gradient of a linear fit to the transmural HA course was calculated and compared together with mean diffusivity (MD) and fractional anisotropy (FA) between multi-band and sequential imaging. Diffusion tensor metrics were determined on the left ventricle excluding epi- and endocardial voxels to avoid partial voluming effects. Statistical analysis was performed by a two-tailed paired t-test. Test data were checked for normality and equality of variances in SPSS (Version 23, IBM Corp., Armonk, NY) using the Shapiro-Wilk and Levene test, respectively. If the requirements for the t-test were not fulfilled, a non-parametric Wilcoxon signed-rank test was used instead. A p-value smaller than 0.05 was considered statistically significant.

7.3 Results

The slice profile of the dual-band RF pulse was measured to be in very good accordance with the corresponding Bloch simulation (**Figure 7.2**). The error of M_x and M_y relative to simulation was below 2.0% and residual excitation in the stop band (threshold-level: $0.05\cdot\left|M_{x,y}\right|_{\max}$) was 5.5%. **Figure 7.3** depicts aliased raw data prior to image reconstruction. Aliasing from two slices and additional N/2 ghosting can be observed. Unfolded magnitude images (b=0s/mm^2) show good correspondence with the reference single-slice data. The effect of controlled aliasing on the g-factor can be appreciated in **Figure 7.4**. For the presented example case of dual-band image reconstruction, the mean g-factor reduces from 1.69±0.24 without inter-slice shift to 1.19±0.10 with FOV/2 shift. According to eq. (7.4) this translates to a theoretical SNR loss relative to non-accelerated acquisition of 41% without shift and 16% with shift, respectively.

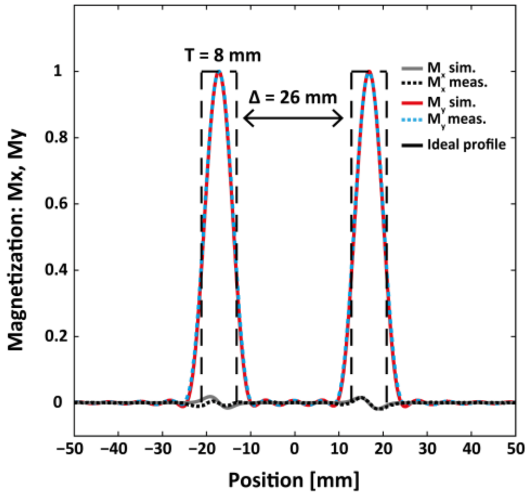

Figure 7.2 Measured (dotted line) and simulated (solid line) slice profiles of the multi-band pulse.

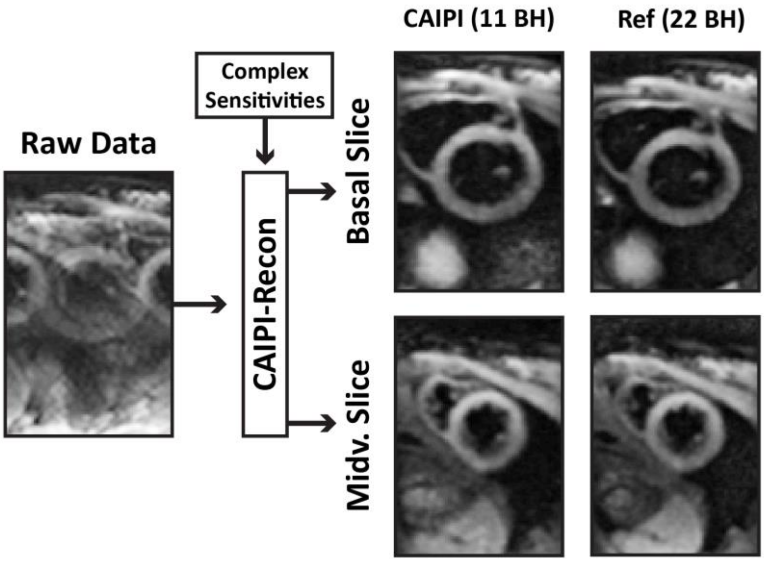

Figure 7.3 Left: Aliased raw data prior to image reconstruction. Right: Unfolded images show good correspondence with reference data obtained by sequential single-slice imaging. BH: breath hold.

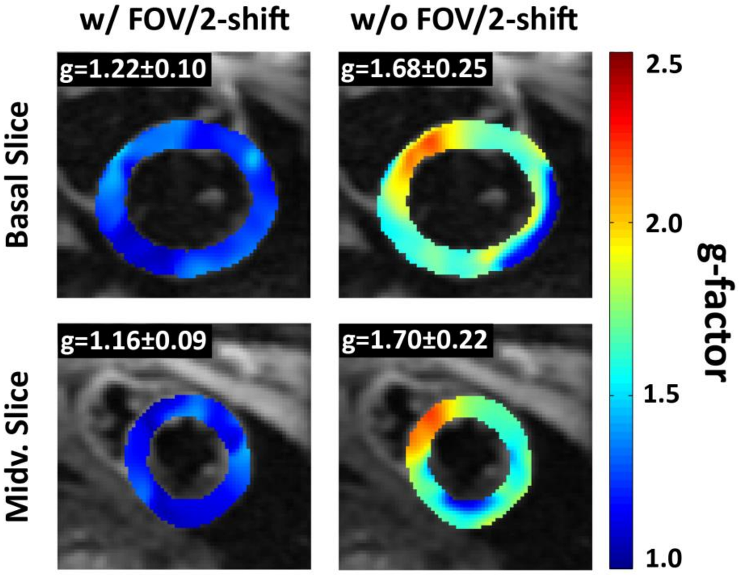

Figure 7.4 g-factor maps for dual-band image reconstruction with and without FOV/2 shift. g-factors are reduced when using controlled aliasing.

First eigenvectors of the diffusion tensors are shown in **Figure 7.5** for SMS and reference imaging: Accelerated and conventional data are in very good agreement following the circumferential contour of the left ventricle. HAs are reported for four transmural layers at septal, inferior, lateral and anterior region in **Figure 7.6**. A linear transition of HA from endo- to epicardium can be seen for all cases in **Figure 7.7**. HAs were found to be steeper at the midventricular level compared to the basal level.

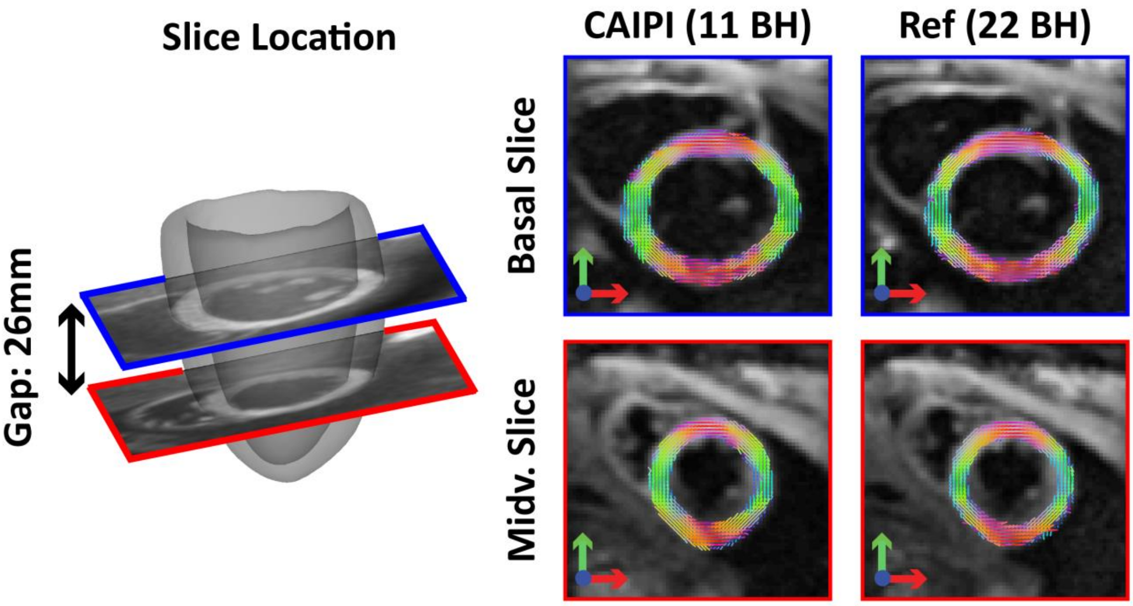

Figure 7.5 Left: Slice locations in the left ventricle. Right: Diffusion tensor representation (1st Eigenvector) of reconstructed CAIPI and reference DTI data. BH: breath hold.

Table 7.1 lists helix and transverse angles from SMS and sequential single-slice imaging. Endo- and epicardial HA (HA_{endo}, HA_{epi}) and corresponding slopes were found to be slightly reduced in the SMS case relative to reference data, however differences were statistically not significant. Mean TA were close to zero degrees with comparable standard deviations for both measurements. No statistically significant differences were found for MD and FA in SMS and single-slice imaging. Except for TA_{std} (ref, midv. slice) and FA (caipi, basal slice), all diffusion metrics fulfilled the requirements for t-testing. Assuming an effective respiratory navigator efficiency of 30%, the total acquisition time for the DTI scans is halved for the multiband approach compared to the sequential single slice acquisition (19:14±1:44 min:sec vs. 9:37±0:52 min:sec).

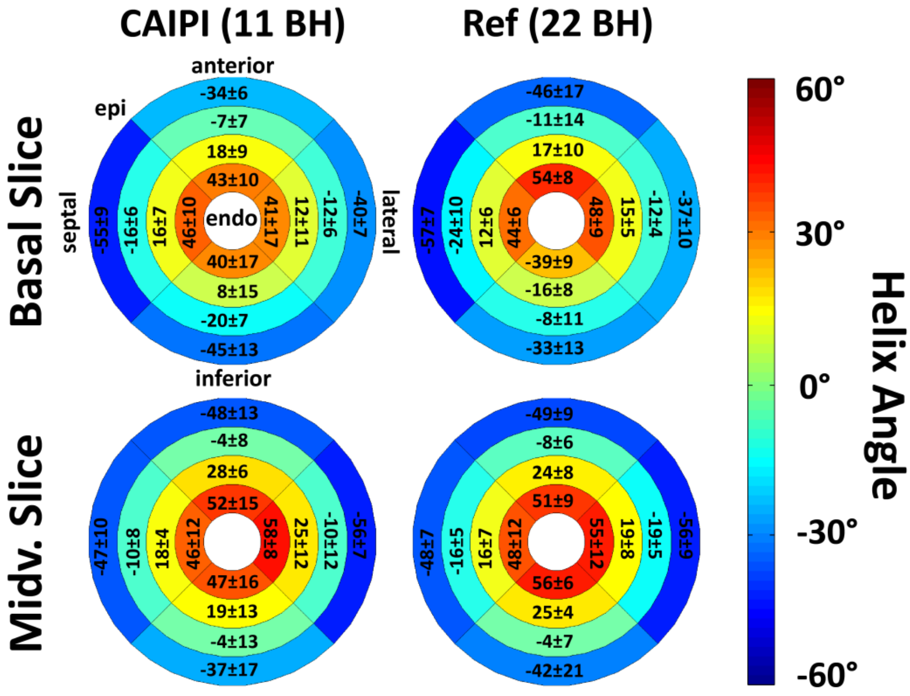

Figure 7.6 Helix angle plots along 4 transmural layers and 4 sectors for CAIPI and reference DTI data. Reported values are mean and standard deviation across the study population. BH: breath hold.

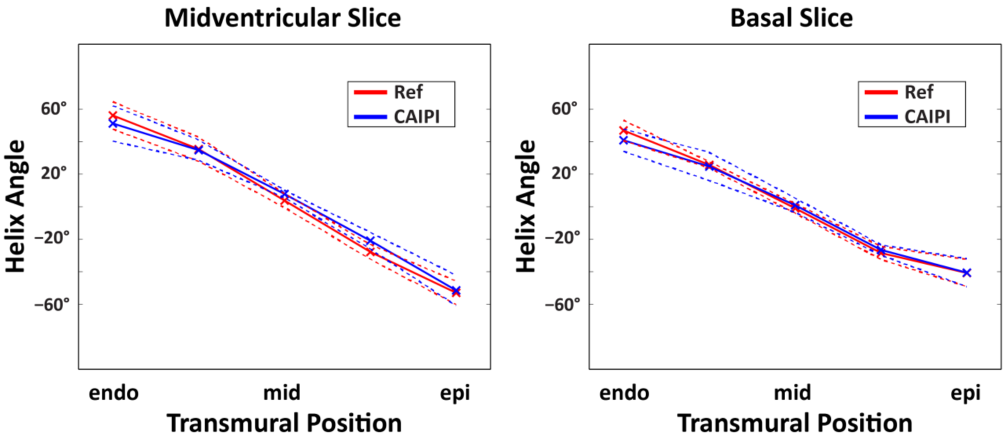

Figure 7.7 Linear transmural course of HA. Solid and dashed lines represent mean and standard deviation of HA across all subjects.

	Midv. Slice			Basal Slice		
	CAIPI	Ref	P	CAIPI	Ref	p
HA-Slope [°/%depth]	-1.06±0.18	-1.16±0.17	0.22	-0.94±0.19	-1.01±0.09	0.28
HA_{endo} [°]	41±9	44±10	0.60	29±8	33±3	0.30
HA_{epi} [°]	-35±8	-38±6	0.29	-34±7	-37±7	0.46
TA_{mean} [°]	0±3	-1±2	0.37	1±3	-1±2	0.06
TA_{std} [°]	19±4	18±2	0.46	20±5	20±4	0.86
MD [$x10^{-3}$ mm^2/s]	0.99±0.06	0.98±0.10	0.85	0.99±0.12	1.04±0.11	0.18
FA	0.58±0.03	0.59±0.05	0.62	0.59±0.04	0.58±0.04	0.17

Table 7.1 Statistical analysis on diffusion tensor metrics for SMS and reference measurements

7.4 Discussion

Cardiac DTI using the STEAM approach is an inherently slow acquisition method requiring several breath holds or dedicated navigator gating strategies (37). Hence, a high degree of patient cooperation is required.

In this work, a single-shot dual-slice diffusion encoding sequence has been presented increasing scan efficiency of cardiac STEAM DTI by a factor of two. To the author's knowledge, this is the first implementation of SMS imaging for *in vivo* cardiac DTI and a significant step towards whole-heart DTI coverage in a clinically acceptable scan time. The extension of the dual-band approach to three concurrently acquired slices was later shown by Lau et al. (227). More recently, the feasibility of free-breathing SMS imaging using respiratory navigator gating has been demonstrated (228), potentially further improving the clinical applicability of cardiac DTI.

A good agreement between accelerated and conventional single-slice DTI metrics was observed: No statistical differences were found for helix and transverse angles between SMS and reference data. HA followed a linear decrease from endo- to epicardium as shown in previous studies (37,38,81,159). A reduced longitudinal alignment of helix angles at basal level compared to midventricular level confirms the results of Stoeck et al. (38). Transverse angles are close to zero degrees indicating a coherent circumferential alignment of the myofibres. Differences of MD and FA between accelerated and conventional imaging were not statistically significant. Obtained results for MD and FA are in accordance with literature values of the *in vivo* human heart (37,38,79,162).

The theoretical SNR loss of the reconstructed SMS images relative to conventional imaging was found to be approximately 16% due to g-factor penalty. SNR efficiency (i.e. SNR per unit time), however, increased by $\sqrt{2}-1\sim$ 41% yielding a net gain in SNR efficiency of 19% relative to sequential single-slice imaging.

The 90° dual-band RF pulses in this study were designed utilising the Shinnar-Le Roux algorithm (226). Due to B_1 limitations, spin echo based SMS imaging may require dedicated methods to reduce maximum RF amplitudes. The Variable Rate Selective Excitation (VERSE) technique can be employed for this purpose, however, this potentially increases off-resonance sensitivity (186) of the excitation slice profile.

Successful parallel image reconstruction requires an accurate determination of the surface coil sensitivities. To this end, reference images without diffusion weighting and similar imaging properties as the diffusion scans were acquired. In particular, image distortions due to the EPI readout were consistent between sensitivity and SMS scans. Solely the slice thickness was increased from 8mm to 16mm to improve SNR and therefore reliability of the reconstruction process. The phase encoding direction was selected parallel to the chest wall to exploit coil sensitivity variations of the cardiac receiver array and reduce g-factor penalty. This geometry is additionally favorable as no high signal intensity from the chest wall folds into the myocardium when performing SMS in conjunction with CAIPIRINHA. Finally, B_0 homogeneity by shimming needs to be ensured over a larger volume as compared to single-slice acquisition.

7.5 Conclusion

SMS imaging can be employed to accelerate *in vivo* cardiac DTI by a factor of two relative to conventional single-slice acquisition. Obtained DTI metrics were comparable between accelerated and non-accelerated measurements. The proposed method allows increased spatial coverage of the heart and potentially improves acceptance of *in vivo* cardiac DTI in a clinical setting.

Chapter 8

Verification of the Intra-Voxel Incoherent Motion (IVIM) Model in the Porcine Heart*

8.1 Introduction

Magnetic resonance diffusion-weighted imaging relies on the signal attenuation due to random motion of water molecules in the presence of diffusion encoding gradients. Additionally, microvascular perfusion can contribute to the signal loss as described by the intra-voxel incoherent motion (IVIM) model (115). According to Le Bihan et al. (115), perfusion can be modeled as pseudo diffusion on a macroscopic scale, assuming a random orientation of the capillary network and blood flow in the tissue of interest. Consequently, the signal intensity can be described by a bi-exponential signal decay as a function of the diffusion encoding strength (b-value). As the IVIM method is an endogenous contrast technique, its application is particularly suited for perfusion measurements where contrast agent administration is contraindicated. In recent years this technique has gained significant momentum with successful applications in various types of healthy and diseased organs (229–233).

---

* Based on: Constantin von Deuster, Christian T. Stoeck, Lukas Wissmann, Georg Spinner, Thea Fleischmann, Maximilian Y. Emmert, Nikola Cesarovic, Sebastian Kozerke. "Verification of the intra-voxel incoherent motion (IVIM) model in the porcine heart", Proceedings of the 23rd Meeting of ISMRM, Toronto, Canada, 2015

Cardiac IVIM requires reliable *in vivo* diffusion-weighted imaging methods. By means of diffusion tensor imaging (DTI), the tissue microstructure can be probed by employing diffusion-weighted single-shot spin echo (SE) (33–35,154) or Stimulated Echo Acquisition Mode (STEAM) (31,37,38,79,87,162) techniques. A number of cardiac DTI studies have shown that the myocardium consists of a highly organized muscular structure forming a double helical pattern from endo- to epicardium (18,37,38,79). Infarcted and ischemic areas can be delineated with low b-value diffusion-weighted SE imaging in good agreement with late-gadolinium enhanced imaging (234,235). *In vivo* cardiac diffusion-weighted imaging, however, still remains very challenging due to cardiac and respiratory motion. Additionally, low signal-to-noise ratio (SNR) and long scan times are major impediments to a wide acceptance in clinical settings. Motion induced signal loss in SE based IVIM has been addressed by diastolic triggering and dedicated post-processing using Principal Component Analysis (PCA) filtering in combination with temporal maximum intensity projection (PCATMIP) (40,119,120,133). Alternatively, diffusion encoding during systole has been performed using motion-compensated diffusion gradient waveforms (33–35,154,155,158). *In vivo* cardiac DTI studies in humans (34) and animals (35) using second- and third- order motion-compensated diffusion imaging have been presented recently.

Cardiac IVIM parameters were initially reported for the *in vivo* canine heart by Callot et al. (183). The measured diffusion-weighted signal agreed well with the bi-exponential model of the IVIM theory with reduced signal decay in the absence of perfusion post mortem. The employed STEAM sequence, however, allows blood circulation during the long mixing time (~1-R-R interval) potentially biasing sensitivity to perfusion and thereby compromising the resulting IVIM metrics. A significant reduction in diffusivity by 29% was reported between *in vivo* and post mortem measurements (183).

The objective of the presented work is to validate *in vivo* IVIM measurements in a pig model of myocardial infarction. *In vivo* measurements during systolic contraction were obtained using a second-order motion-compensated single-shot spin echo sequence. IVIM parameters were derived to evaluate the contribution of microvascular perfusion to the diffusion-weighted signal. Additional post mortem IVIM measurements were performed as a reference without motion and perfusion effects.

8.2 Methods

Animal Preparation and Control

Five female pigs (weight 51±23kg, heart rate 69±7beats/min) were anesthetized by a constant intravenous dose of Propofol (1.0ml/kg/min) during surgery and *in vivo* MRI measurements. An acute myocardial infarction in the apical septum was induced by permanent distal ligation of the left anterior descending coronary artery (LAD). The time delay between occlusion and *in vivo* imaging was approximately 2-3 hours. During the *in vivo* measurements, the animals were intubated and ventilated. A femoral vein catheter was used for drug delivery. Heart rate and pO_2 were recorded continuously by electrocardiogram and a peripheral pulse unit, respectively. Respiration was monitored by a breathing belt and continuous measurements of exhaled CO_2. Upon completion of *in vivo* scanning, the pigs were euthanized by an overdosed potassium chloride injection inside the MR scanner bore and the imaging protocol was repeated thereafter. Post mortem diffusion scans were finished within 45 minutes of death as control reference for the IVIM model. The animal experiments were performed in adherence to the Swiss law of Animal Protection and approved by the Zurich cantonal veterinary office.

Study Protocol

Cardiac SE diffusion-weighted imaging was implemented on a 1.5T Philips Achieva System (Philips Healthcare, Best, The Netherlands) with gradients delivering 80mT/m maximum strength at a slew rate of 100mT/m/ms per physical axis. Signal was received with a 5-channel cardiac receiver array. Prior to diffusion imaging, cine data with a temporal resolution of 10ms were acquired in two-chamber and short-axis view orientations.

Diffusion Imaging

Diffusion-weighted imaging was performed during free breathing in short-axis view orientation with a reduced field-of-view (FOV) technique (185) (**Figure 8.1**). The single-shot spin echo sequence with second-order motion-compensated diffusion encoding

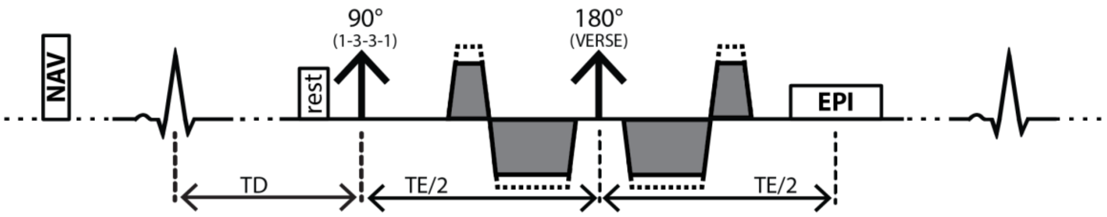

Figure 8.1 Second-order motion-compensated diffusion-weighted imaging sequence. Dashed lines indicate the variation of gradients to achieve different diffusion encoding strengths (b-values) whilst keeping the duration of the gradients constant. Fat suppression is achieved by a binomial excitation pulse. The trigger delay (TD) was set to mid systole.

gradients (34,35) was ECG triggered to mid systole (50% time to peak contraction). To avoid aliasing from residual excitation along the phase encoding direction, non-coplanar excitation (236) in conjunction with saturation slabs orthogonal to the imaging plane were played out prior to the RF excitation pulse. Fat suppression was achieved by a 1-3-3-1 binomial spatial-spectral excitation (141). The duration of the 180° refocusing pulse was minimized using variable rate selective excitation (VERSE) (186). Two slices (**Figure 8.2**) in healthy and ischemic region (midventricular and apical area, respectively) were acquired. The imaging parameters were as follows: spatial resolution: 2.4×2.4mm^2, slice thickness: 10mm, field-of-view (FOV): 230×100-120mm^2, TR/TE: 2R-R/87-94ms, 8 signal averages. Data were acquired along six diffusion encoding directions (97) for 16 b-values in the range of 0 to 880s/mm^2. The b-value distribution was taken from the literature (237). Using Monte Carlo simulations and employing the IVIM fit error as optimization criterion, an optimal b-value distribution can be determined as described by Lemke et al. (237). The duration of diffusion encoding gradients for the different diffusion weightings, and hence the echo time, was kept the same and differences in b-values were achieved by scaling the gradient strength.

Dynamic Contrast Enhanced (DCE) Imaging

As reference method for ischemia detection, 2D first-pass contrast-enhanced perfusion imaging was performed in short-axis view orientation upon diffusion imaging. Perfusion and diffusion imaging was carried out at the same slice locations. A saturation-recovery single-shot gradient echo sequence triggered to mid-systole was

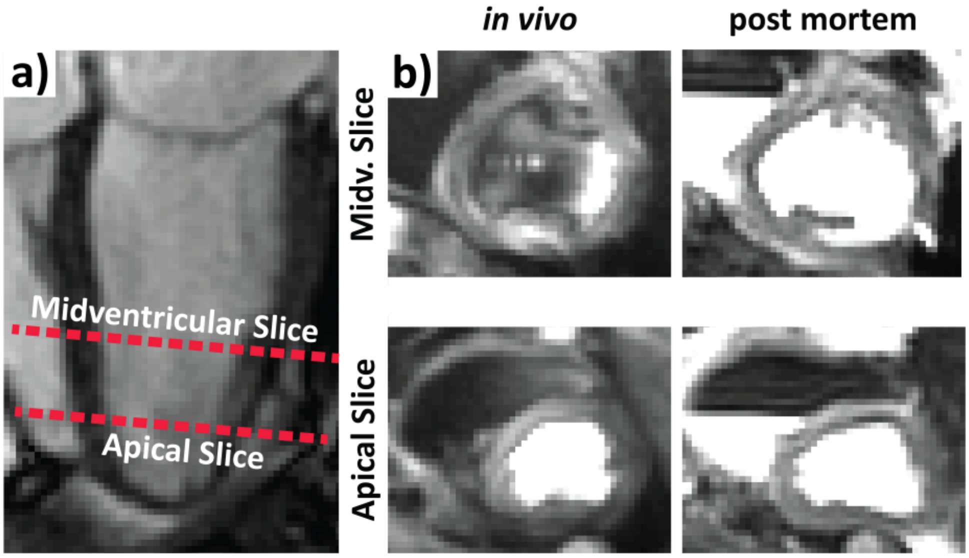

Figure 8.2 a) Slice locations of apical and midventricular slice with corresponding short-axis views (b). Apparent blood sedimentation can be seen post mortem.

employed (238,239). The imaging parameters read: spatial resolution: 1.5x1.5mm^2, slice thickness: 10mm, FOV: 360x360mm^2, flip angle: 15°, TR/TE: 2.7/1.3ms, 5x k-t acceleration, saturation delay: 215ms. An intravenous bolus of 0.05mmol/kg gadolinium based contrast agent (Gadovist, Bayer Schering, Germany) was injected at a rate of 3ml/s followed by 30ml flush of saline solution at the same rate.

Data Post processing

Signal intensities S(b) were derived from trace diffusion-weighted images for each b-value and fitted to the mono- and bi-exponential signal models:

$$\frac{S(b)}{S_0} = \mathrm{e}^{-bD} \tag{8.1}$$

$$\frac{S(b)}{S_0} = f \cdot \mathrm{e}^{-bD^*} + (1-f) \cdot \mathrm{e}^{-bD} \tag{8.2}$$

using the constrained Levenberg-Marquardt algorithm of the Matlab fitting toolbox (MathWorks, Natick, MA). S(b) describes the measured signal as function of b-value, S_0 the signal without diffusion weighting (b=0s/mm^2), f the perfusion fraction, D the diffusion constant and D* the pseudo-diffusion constant. Least squares fitting was performed on a pixel-by-pixel basis in the left ventricular myocardium. In the bi-exponential case, a segmented approach as described in (183,232) was used assuming pure diffusion for b-values above 350s/mm^2. The starting values for signal fitting were: f=0.5, D=1.0x10^{-3}mm^2/s and D*=10x10^{-3}mm^2/s.

Different relaxation terms of the perfusion and diffusion compartments can be incorporated into the IVIM model as proposed by Lemke et al (118). As the transverse relaxation times of blood and myocardium are very similar (~50-52 ms (139,142)), it is sufficient to extend eq. (8.2) for T1 terms only:

$$\frac{S(b)}{S_0}=\frac{f\cdot \mathrm{e}^{-bD^*}\cdot(1-\mathrm{e}^{-TR/T1_{blood}})+(1-f)\cdot \mathrm{e}^{-bD}(1-\mathrm{e}^{-TR/T1_{myo}})}{f\cdot(1-\mathrm{e}^{-TR/T1_{blood}})+(1-f)\cdot(1-\mathrm{e}^{-TR/T1_{myo}})} \qquad (8.3)$$

IVIM parameters derived by eq. (8.2) were corrected for T1 relaxation based on eq. (8.3). T1 values for blood ($T1_{blood}$) and myocardium ($T1_{myo}$) were taken from literature: 1500 ms and 1030 ms, respectively (143,240). The repetition time TR was determined by the heart rate: $TR=2\cdot 1000\cdot\frac{60[\mathrm{bpm}]}{HR[\mathrm{bpm}]}[\mathrm{ms}]$.

Data Analysis

In each subject, a Region-of-Interest (ROI) was manually drawn to define the left ventricle (LV) *in vivo* and post mortem. Voxels at the epi- and endocardial borders were excluded from data analysis to avoid partial voluming effects. For the midventricular slice without infarction, median IVIM parameters were derived across the left ventricle on a per subject basis. The results of the IVIM metrics are reported as mean ± one standard deviation across all pigs. Pre and post mortem IVIM parameter comparison was performed using a two-tailed paired t-test. The agreement of the mean diffusion-weighted signal with the mono- (eq. (8.1)) and bi-exponential model (eq. (8.2)) was evaluated by the root mean squared fitting error (RMSE).

Infarcted and healthy tissue in the apical slice was classified in six circumferential sectors based on the signal intensity of the DCE measurements: First, the signal range between infarcted and healthy tissue was determined within a timeframe of approximately 30s after bolus injection. If more than 50% of the area within a sector had a signal level increase of at least 50% of the calculated signal range, the sector was considered as healthy, otherwise as infarcted. For each sector, median IVIM parameters were calculated. Statistical significance of the differences in f, D and D* between in-vivo/post-mortem measurements and infarcted/healthy sectors were determined by a Wilcoxon signed-rank test and an unpaired Mann-Whitney-U test, respectively. A p-value less than 0.05 was considered statistically significant.

8.3 Results

The total acquisition time of the diffusion weighted scans was 30:50±3:07 min:sec. **Figure 8.3** shows a selection of DW trace images for the *in vivo* and post mortem case at apical and midventricular level. *In vivo* signal intensities of the left ventricle are statistically significant lower ($p<0.01$) for high diffusion weightings ($b>450s/mm^2$) compared to the corresponding post mortem signal levels. Signal hyper intensity can be observed in the septal region of the *in vivo* apical slice as indicated by the red arrow. The corresponding mean signal intensities across the midventricular LV *in vivo* and post mortem are shown in **Figure 8.4**. Logarithmic representation of the signal curves presents bi- and mono-exponential decays, respectively. The bi-exponential model (eq.(8.2)) showed a significantly ($p<0.05$) better agreement with the *in vivo* results ($RMSE_{bi}$: 0.014±0.006) than the mono-exponential model (eq. (8.1)) ($RMSE_{mono}$: 0.034±0.014). The mono-exponential model overestimates the diffusion constant D by 40% (D_{mono}: $1.8\pm0.4x10^{-3}mm^2/s$ versus D_{bi}: $1.3\pm0.1x10^{-3}mm^2/s$, $p<0.05$). For the post mortem measurements, both signal models had similar fitting errors ($RMSE_{mono}$: 0.018±0.007 versus $RMSE_{bi}$: 0.019±0.013, $p=0.69$) and estimates for D (D_{mono}: $1.2\pm0.1x10^{-3}mm^2/s$ versus D_{bi}: $1.2\pm0.1x10^{-3}mm^2/s$, $p=0.22$).

Acutely infarcted area in the apical septum is clearly visible in the DCE measurement (**Figure 8.5 a)**). Signal time curves for two ROIs in healthy and infarcted myocardium show signal increase and baseline level upon bolus injection, respectively. Ischemic myocardium was not present in the midventricular slice in the example data set. Perfusion fraction f and pseudo diffusion D* in the infarcted zone are markedly reduced compared to surrounding tissue (**Figure 8.5 b)**). A subtle increase in D is noticeable between healthy and infarcted area, however spatial parameter variations

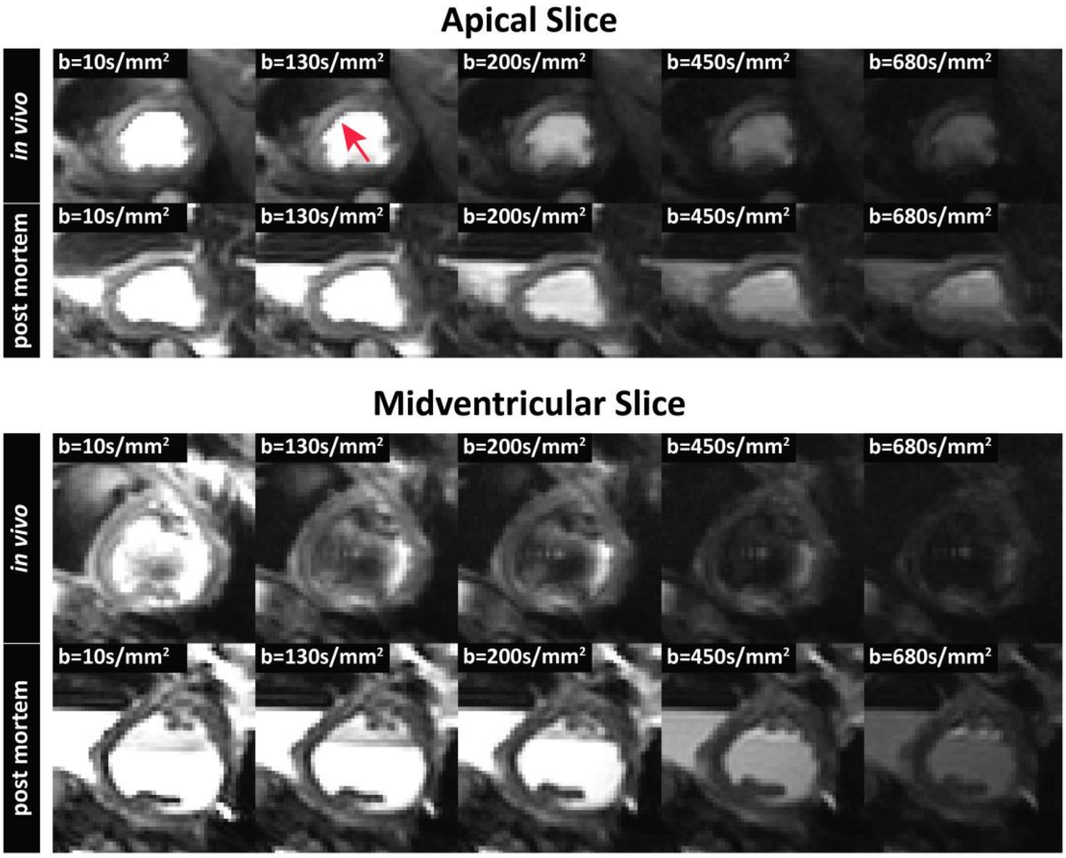

Figure 8.3 *A selection of in vivo and post mortem trace images at apical and mid-ventricular level. Signal hyper intensity is observed in the septum of the apical slice (red arrow). Post mortem signal intensities are significantly increased for high b-values ($b>450$ s/mm^2) compared to corresponding in vivo signal levels.*

are less distinct compared to f and D*. For the midventricular slice, f and D* decreased significantly from *in vivo* to post mortem measurements ($f_{in\ vivo}$: 0.21±0.13 versus $f_{post\ mortem}$: 0.01±0.01, $p<0.05$, $D^*_{in\ vivo}$: 9.0±1.1x10^{-3}mm^2/s versus $D^*_{post\ mortem}$: 4.3±2.7x10^{-3}mm^2/s, $p<0.05$). No statistically significant differences were found for $D_{in\ vivo}$: 1.3±0.1x10^{-3}mm^2/s versus $D_{post\ mortem}$: 1.1±0.1x10^{-3}mm^2/s, p=0.10. A high variability in D* maps can be seen in both slices post mortem. **Table 8.1** lists IVIM parameters with additional T1 correction. The results for D remain unchanged, whereas f is increased with T1 correction and the values for D* are reduced compared to the uncorrected values.

	T1 corr.	In vivo	Post mortem	p
f	No	0.21±0.13	0.01±0.01	<0.05
	Yes	0.25±0.16	0.02±0.02	<0.05
D [$\times 10^{-3}$ mm^2/s]	No	1.3±0.1	1.1±0.1	0.10
	Yes	1.3±0.1	1.1±0.1	0.10
D* [$\times 10^{-3}$ mm^2/s]	No	9.0±1.1	4.3±2.7	<0.05
	Yes	4.2±0.5	2.8±2.1	0.08

Table 8.1 *Statistical analysis on IVIM parameters with and without T1 correction.*

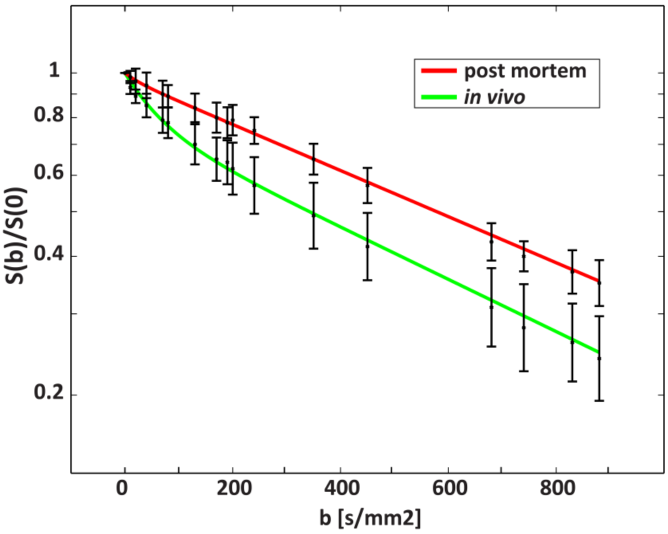

Figure 8.4 *Logarithmic signal decay curves for in vivo and post mortem diffusion imaging. In vivo and post mortem signals follow a bi- and mono-exponential decay, respectively. Signal slopes are comparable between both measurements for high b-values (b>450 s/mm^2).*

At least two out of the six sectors of each apical slice were ischemic according to DCE imaging. In all subjects, the septal area was infarcted, whereas the lateral region remained healthy. The sector classifications and corresponding results for f are shown in **Figure 8.6 a)**. The numbers indicate the fraction of infarcted sectors across all pigs (N=5). In the infarcted sectors, f is reduced by more than 50% relative to the healthy region. In one dataset, myocardial infarction extended to the septal region in the midventricular slice. It was taken into account as sixth dataset and combined with the five apical slices to compute the f value distribution in healthy and infarcted sectors. The corresponding box plots are shown in **Figure 8.6 b)**. The solid boxes and error bars correspond to 50% and 90% percentiles of the perfusion fraction distributions. The reduction in f between healthy and infarcted tissue was found to be statistically significant (median $f_{infarct}$: 0.05 versus median $f_{healthy}$: 0.16, $p<0.01$). Diffusivity was increased in infarcted tissue compared to healthy myocardium (median $D_{infarct}$: $1.34 \times 10^{-3} mm^2/s$ versus median $D_{healthy}$: $1.27 \times 10^{-3} mm^2/s$, $p=0.19$). Pseudo-diffusion was reduced in the infarcted region relative to healthy tissue (median $D^*_{infarct}$: $6.27 \times 10^{-3} mm^2/s$ versus median $D^*_{healthy}$: $8.10 \times 10^{-3} mm^2/s$, $p=0.14$). **Table 8.2** lists the median IVIM parameters with additional T1 correction.

	T1 corr.	Infarct region	Healthy region	p
f	No	0.05	0.16	<0.01
	Yes	0.04	0.20	<0.01
D [$\times 10^{-3}$ mm^2/s]	No	1.34	1.27	0.19
	Yes	1.34	1.27	0.19
D* [$\times 10^{-3}$ mm^2/s]	No	6.27	8.10	0.14
	Yes	3.24	4.14	0.26

Table 8.2 Median IVIM parameters with and without T1 correction.

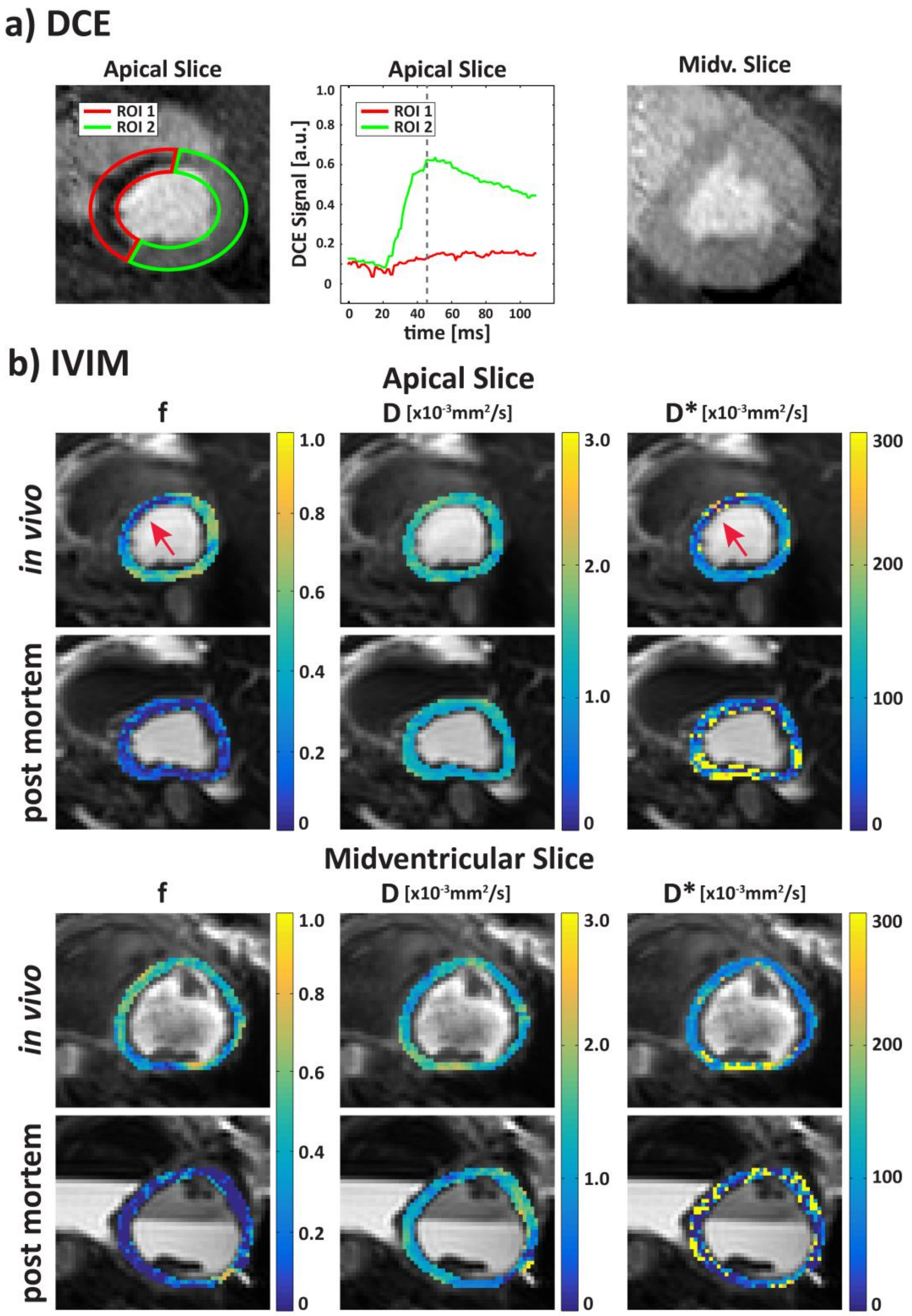

Figure 8.5 a) Dynamic contrast enhanced (DCE) first pass perfusion imaging showing infarcted area in septum. DCE signal time curves for two ROIs in infarcted (ROI 1) and healthy (ROI 2) regions show baseline level and signal increase upon bolus injection, respectively. No infarcted area can be seen in the midventricular slice. The dashed grey line indicates the time point of the DCE images. b) In vivo and post mortem IVIM parameter maps at apical and midventricular level: The infarcted area correlates with a reduced perfusion fraction (f) and pseudodiffusion (D). f reduces close to zero from in vivo to post mortem measurements. No significant change can be observed for D between pre and post mortem imaging. Post mortem D* maps show increased variabilty compared to in vivo D* maps.*

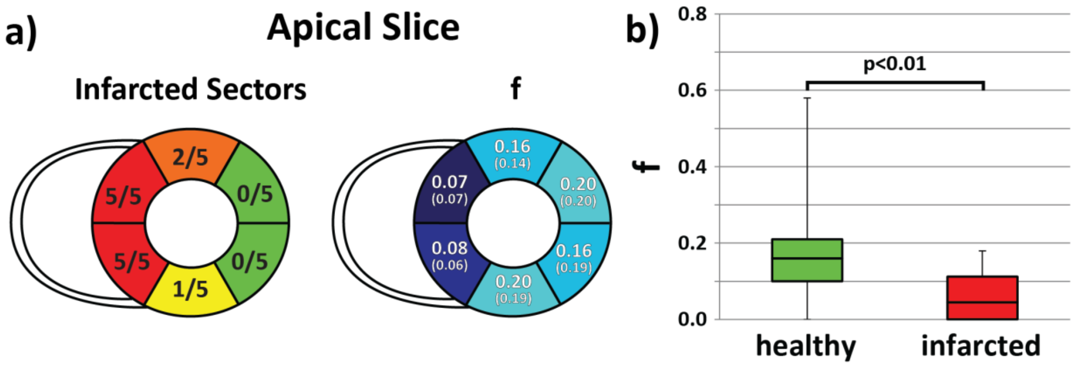

Figure 8.6 a) Infarct classification map for six sectors of the apical slice: the numbers indicate the fraction of infarcted sectors across all pigs (N=5). The septal area was found to be infarcted in all animals, whereas the lateral region was classified as healthy. Perfusion fraction in the septal region was reduced by more than 50% relative to the healthy myocardium. The results for f are reported as mean (top) and standard deviation (below) across all animals. b) The differences in f between infarcted and healthy sectors were found to be statistically significant (p<0.01).

8.4 Discussion

Myocardial perfusion measurements are of high clinical relevance and are performed using contrast agent based imaging techniques. However, one out of three cardiovascular patients suffers from renal insufficiency (8) making contrast agent free perfusion measurements highly attractive. Tissue perfusion adds to the diffusion induced signal decay and its contribution can be described by the IVIM model. Cardiac IVIM requires reliable diffusion-weighted imaging sequences and a dedicated management of physiological motion. Whereas respiratory motion was less critical in this study compared to human applications due to the porcine anatomy, cardiac contraction needed to be addressed by second-order motion-compensated gradient waveforms (34,35). This requires high performance gradient hardware, but allows mid systolic triggering which is more robust against heart rate variations than diastolic imaging.

In this study, the IVIM model has been validated in porcine hearts using SE *in vivo* cardiac diffusion-weighted imaging. To obtain a reference model without motion and perfusion effects, the pigs were euthanatized within the scanner bore and diffusion imaging was repeated. *In vivo* values for perfusion fractions were significantly reduced to near zero post mortem in agreement with previous results obtained from dog hearts (183). *In vivo* diffusion-weighted signal decay was significantly better described by a bi-exponential model compared to a mono-exponential model. The minor reduction in D between *in vivo* and post mortem was statistically not significant, which attests good motion compensation of the employed gradient waveform designs (34,35). Obtained results for f were slightly increased when T1 relaxation effects were taken into account, whereas the pseudo diffusion constant D* is overestimated without T1 correction.

Moulin et al. (119) obtained a similar diffusion constant, but lower perfusion fraction ($f=0.12\pm0.01$, $D=1.4\pm0.1\times10^{-3}mm^2/s$, $D^*=44\pm9\times10^{-3}mm^2/s$) in the healthy human heart. In contrast to our work, imaging was performed with unipolar diffusion encoding gradients (119) during diastole in combination with PCATMIP filtering to mitigate motion induced signal loss (40,133). Delattre et al. (120) reported an increased D using a bipolar diffusion encoding sequence: $f=0.15\pm0.05$, $D=2.4\pm1.0\times10^{-3}mm^2/s$, $D^*=76\times10^{-3}mm^2/s$. PCATMIP reconstruction relies on the existence of motion unbiased signal for at least one trigger delay. Scott et al. (159) performed cardiac IVIM using the STEAM method: The obtained values for f and D were lower compared to our findings: $f=0.06$, $D=0.86\times10^{-3}mm^2/s$, $D^*=17\times10^{-3}mm^2/s$. Comparable results were obtained by Callot et al. (183): $f=0.08\pm0.01$, $D=1.3\pm0.1\times10^{-3}mm^2/s$, $D^*=13\pm3\times10^{-3}mm^2/s$. Due to the different diffusion encoding times of SE and STEAM based diffusion sequences, motional narrowing (146) and water exchange effects (183) can bias diffusion results and affect IVIM parameters. Besides variations in acquisition techniques and trigger point in the cardiac cycle, different data processing procedures can explain differences relative to and among literature values: Signal fitting has been performed on mean signal within a ROI (159,183), on a pixel-by-pixel basis (119) or a combination of both (120) for different IVIM parameters. Fitting D* is inherently badly conditioned and highly sensitive to low SNR resulting in large variations within and across IVIM studies

(237). In our study, the lack of perfusion post mortem translates into increased D* variability as seen in the D* parameter maps.

The proposed IVIM method allowed delineation of the infarcted area by low f values in good spatial agreement with dynamic contrast-enhanced myocardial perfusion imaging. Statistical analysis showed that the perfusion fraction is significantly reduced in the infarcted area when compared to healthy myocardium. Hence, reduced f and D* can be associated with a lack of microvascular perfusion, potentially leading to reversible or irreversible ischemia with myocardial necrosis. Physiologically this may result in local cardiac dysfunction with reduced mobility and contractility. Similar to previous DTI studies (18,31,51,54), an increase in diffusivity was found in the infarcted myocardium.

Study Limitations:

The obtained IVIM parameters in this study show (in parts) a high variability. This can be explained by the relatively critical state of the animals due to the acute myocardial infarct which causes reduced ECG signal quality. Potential miss-triggering of the imaging sequence may result in incorrect cardiac phases and/or signal voids. In addition, imaging was performed during mid systole when perfusion is physiologically reduced compared to diastole (40,119,133) which lowers perfusion measurement precision. Due to the small sample size (N=5) and low spatial resolution, statistical analysis needed to be performed on a sector and per subject basis. For the same reason and the fact that DCE images are primarily qualitative, first pass perfusion measurements were evaluated in the proposed binary scheme (infarcted vs healthy). Whereas infarcted regions and remote myocardium can be correctly described by the binary approach, perfusion integrity in adjacent myocardium is insufficiently reflected by this method. A higher number of animals and a quantitative analysis of DCE perfusion imaging (including arterial input function measurements) may allow for a more differentiated picture of IVIM-DCE imaging correlations.

In summary, cardiac IVIM has the potential to improve current methods of myocardial tissue characterisation by mapping myocardial perfusion. This endogenous technique is particularly appealing in clinical settings where contrast agent administration is contraindicated. Diffusion-weighted imaging employing second-order motion-compensated gradients, however, requires high performance gradient hardware. This prerequisite is expected to be fulfilled in the near future with the recent developments in MR gradient hardware.

8.5 Conclusion

Myocardial perfusion contributes significantly to cardiac diffusion-weighted imaging signals at low b-values. IVIM parameter mapping allows characterisation of perfusion fractions in good spatial agreement with dynamic contrast-enhanced imaging.

Chapter 9

Bayesian Intravoxel Incoherent Motion Imaging to Map Perfusion in the Human Heart[*‡]

9.1 Introduction

The concept of Intravoxel Incoherent Motion (IVIM) (115) for perfusion measurement in the heart has gained significant interest in recent years (119,120). However, low signal-to-noise ratio, partial voluming, cardiac and respiratory motion render IVIM acquisition and parameter mapping of the heart very challenging. The objective of the present work was to implement cardiac IVIM using a second-order motion-compensated diffusion-weighted spin echo approach in conjunction with Bayesian processing to permit perfusion and diffusion parameter mapping of the heart during cardiac contraction.

---

[*] Based on: Georg Spinner[†], Constantin von Deuster[†], Christian T. Stoeck, Sebastian Kozerke. "Bayesian Intravoxel Incoherent Motion Imaging to Map Perfusion in the Human Heart", Proceedings of the 24th Meeting of ISMRM, Singapore, 2016

† equal contributors

[‡] Methodology, data post processing and data analysis was performed by Georg Spinner.

9.2 Methods

A second-order motion-compensated diffusion-weighted spin echo EPI sequence (**Figure 9.1**) (34) was implemented on a 1.5T Philips Achieva system (Philips Healthcare, Best, The Netherlands) equipped with a 5-channel cardiac receiver coil array and a gradient system delivering 80mT/m at 100 mT/m/ms. Data from five healthy volunteers (3 female, weight 64±11kg, age 25±3years, heart rate 70±4beats/min, min/max heart rates: 65/78beats/min) were acquired upon obtaining written informed consent according to institutional guidelines.

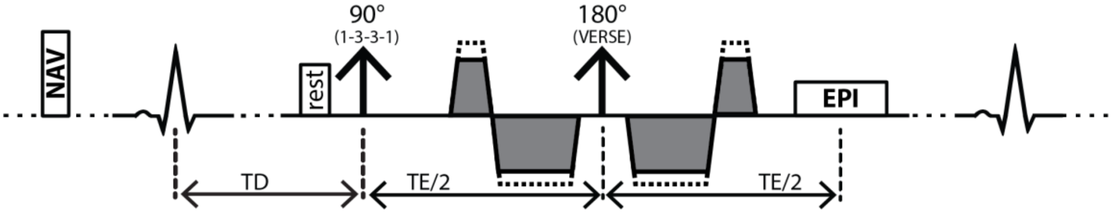

***Figure 9.1** Second-order motion-compensated diffusion-weighted imaging sequence. Dashed lines indicate the variation of gradients to achieve different diffusion encoding strengths (b-values) whilst keeping the duration of the gradients constant. Fat suppression is achieved by a binomial excitation pulse. The trigger delay (TD) was set to mid systole.*

Prior to diffusion imaging, cine data with a temporal resolution of 10ms were acquired in two-chamber and short-axis view orientations. According to the cine images, systolic quiescent time points were determined for each subject. Two short-axis slices at mid-ventricular and apical level were prescribed and diffusion images were obtained with following parameters: spatial resolution: 2.4×2.4mm^2, slice thickness: 10mm, reduced field-of-view (FOV): 230×105mm^2, TR/TE: 2R-R/72ms, 8 signal averages, spectral-spatial water-only excitation (141). Determination of perfusion related parameters is more challenging compared to diffusion metrics (237). To improve IVIM parameter fitting accuracy, b-values were more densely sampled in the perfusion regime, i.e. for b-values below 150s/mm^2, compared to the diffusion regime. Diffusion encoding was performed using 20 b-values (0, 5, 15, 30, 45, 60, 75, 90, 105, 120, 135, 150, 200, 250, 300, 350, 400, 450, 500, 550s/mm^2) acquired during cardiac contraction (50% end systole). Diffusion encoding was along three orthogonal diffusion directions maximizing gradient strength utilisation. Each diffusion direction and b-value was acquired during respiratory navigated breath holding (acceptance window: 5mm).

In post-processing, affine image registration of diffusion-weighted images and averages was performed using elastix (147) to correct for residual respiratory motion induced geometrical inconsistency. In addition, image intensities were corrected to account for variations of the effective repetition time TR as a result of varying heart rate. Thereupon, the signal S(b) was fitted using the IVIM model (115):

$$\frac{S(b)}{S_0} = f \cdot \mathrm{e}^{-bD^*} + (1-f) \cdot \mathrm{e}^{-bD} \tag{9.1}$$

with reference intensity S_0, diffusion encoding strength b, diffusion coefficient D, perfusion fraction f and pseudo-diffusion coefficient D*. For model fitting, a Bayesian shrinkage prior (BSP) inference approach (241) was implemented to estimate the parameters of the IVIM model. The shrinkage prior was a multivariate Gaussian distribution of the log/logit-transformed IVIM parameters:

$$\begin{aligned} d &= \log(D) \\ f &= \operatorname{logit}(F) = \log(F) - \log(1-F) \\ d^* &= \log(D^*) \end{aligned} \tag{9.2}$$

The mean across the region-of-interest (ROI) of the parameter $\boldsymbol{\theta}_i = [d_i, f_i, {d^*}_i]$ of voxel i is $\boldsymbol{\mu} = [\mu_d, \mu_f, \mu_{d^*}]$ and correlations between the parameters are described by the covariance matrix Σ_μ. A Jeffrey's prior (242) is used for the hyper-parameters $\boldsymbol{\mu}$ and Σ_μ:

$$p(\boldsymbol{\mu}, \Sigma_\mu) = \left| I(\Sigma_\mu) \right|^{1/2} = \left| \Sigma_\mu \right|^{-1/2} \tag{9.3}$$

This prior leads to maximization of the Fisher Information $I(\Sigma_\mu)$ and to a minimization of the (co-)variance of the parameters in the ROI. Hence a "shrinking" of the posterior distribution can typically be observed.

Expectation values under the posterior can be computed numerically using the Markov Chain Monte Carlo implementation as proposed by Orton et al. To this end, $1.0\text{x}10^4$ samples were used for a burn-in phase and $2.0\text{x}10^4$for the actual sampling. Further details can be found in the Appendix of Orton et al. (241). For comparison, a standard segmented least squares (LSQ) fit was used (243). Both the LSQ and the BSP method were implemented in Matlab (The Mathworks, Natick, MA) as part of the overall processing chain. In data analysis, mean and standard deviation of f, D and D* across the myocardium and slices was compared for BSP vs. LSQ. Obtained values are reported for each subject of the study population and differences between LSQ and BSP were determined by a Wilcoxon signed-rank test. P values below 0.05 were considered statistically significant.

9.3 Results

Systolic IVIM data were successfully acquired in all subjects (**Figure 9.2**) within 27:40±1:35 min:sec. BSP processing resulted in reduced variability in f, D and D* maps across the myocardium when compared to the LSQ results (**Figure 9.3**). Corresponding histograms of the IVIM parameters show a clearly narrower distribution for BSP compared to LSQ. This translates to reduced standard deviations for all BSP IVIM parameters relative to LSQ, which was found to be statistically significant ($p<0.05$) in case of D: $D_{LSQ}=1.38\pm0.23\text{x}10^{-3}\text{mm}^2/\text{s}$ vs. $D_{BSP}= 1.34\pm0.13\text{x}10^{-3}\text{mm}^2/\text{s}$. No significant difference between LSQ and BSP was observed for the average D. In particular, high bin counts of the LSQ fitting boundaries of f and D* vanish for BSP, such that changes in average f and D* were found to be statistically significant ($p<0.05$), but not the corresponding standard deviations: $f_{LSQ}=0.094\pm0.078$ vs. $f_{BSP}=0.153\pm0.066$ and $D^*_{LSQ}=29.1\pm44.5\text{x}10^{-3}\text{mm}^2/\text{s}$ vs. $D^*_{BSP}=16.2\pm25.9\text{x}10^{-3}\text{mm}^2/\text{s}$. **Table 9.1** lists obtained IVIM parameters for LSQ and BSP on a per subject basis.

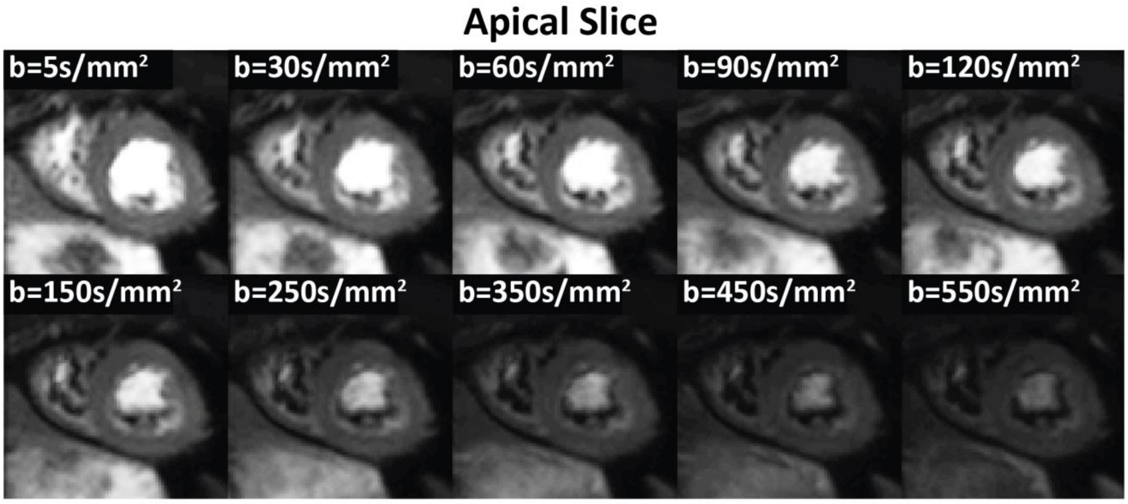

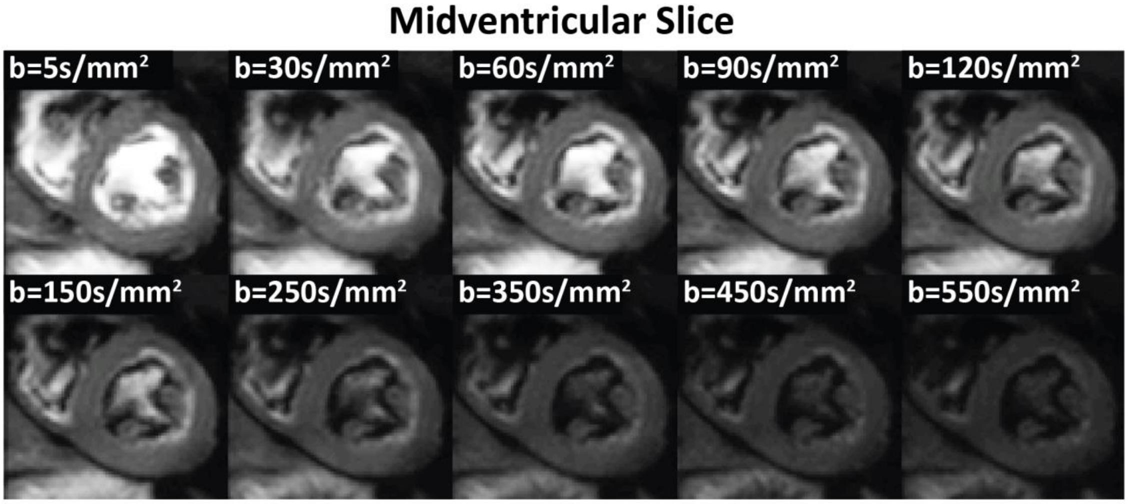

Figure 9.2 Selection of trace images obtained for an apical and mid-ventricular slice.

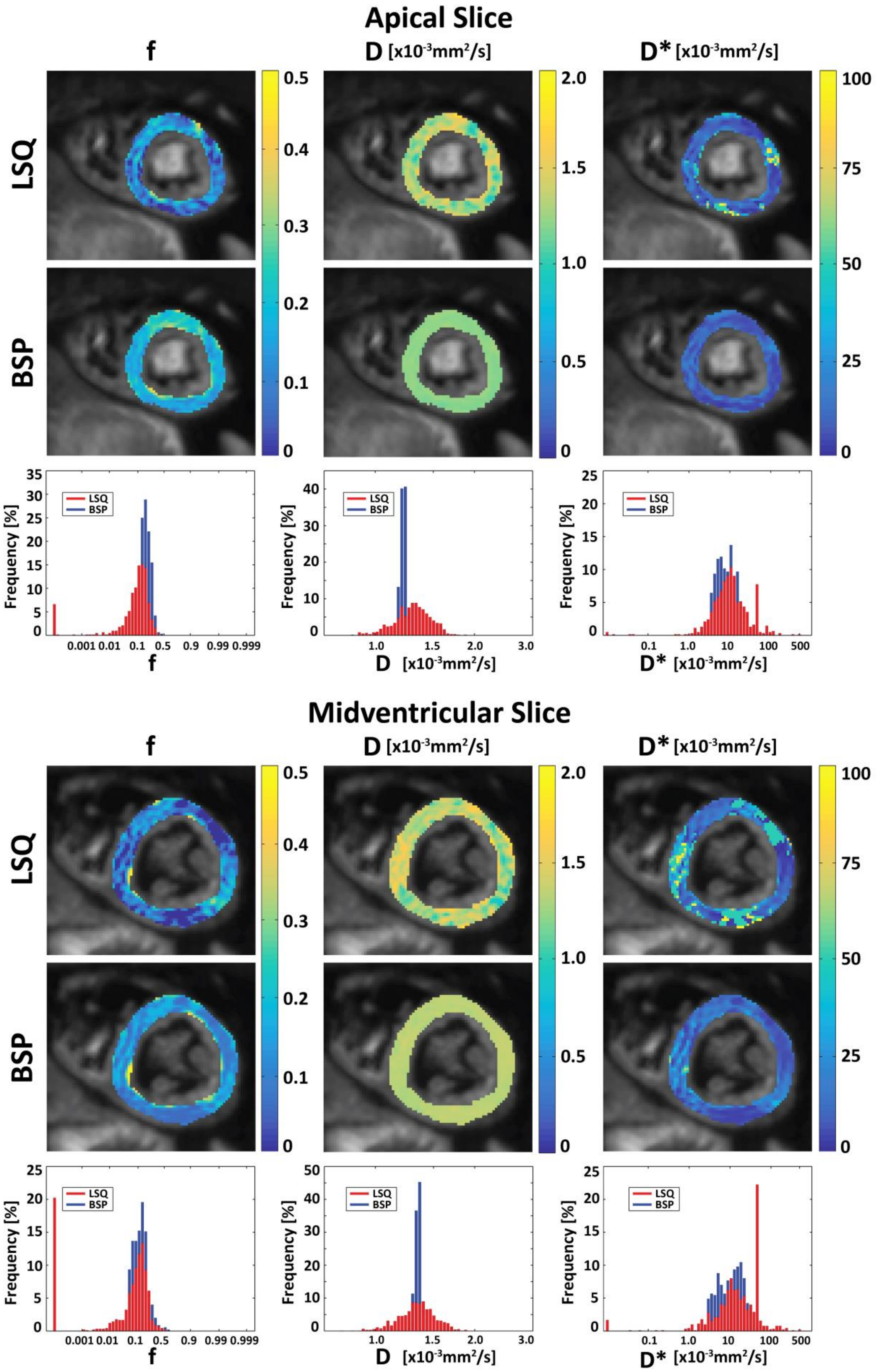

Figure 9.3 Example IVIM parameter maps comparing least squares (LSQ) and Bayesian Shrinkage Prior (BSP) based results. Variability in IVIM parameters is considerably reduced for BSP relative to LSQ.

		f		D [10^{-3}mm^2/s]		D* [10^{-3}mm^2/s]	
Vol.	Slice	LSQ	BSP	LSQ	BSP	LSQ	BSP
1	1	0.12±0.07	0.14±0.07	1.45±0.20	1.44±0.17	22.5±45.7	18.5±11.7
1	2	0.10±0.07	0.15±0.06	1.48±0.19	1.47±0.07	29.9±47.5	25.4±32.0
2	1	0.11±0.06	0.17±0.05	1.40±0.22	1.27±0.18	18.8±13.1	11.1±4.1
2	2	0.09±0.07	0.17±0.07	1.40±0.19	1.27±0.07	21.0±17.4	9.1±3.2
3	1	0.04±0.06	0.11±0.05	1.33±0.34	1.35±0.30	43.7±71.5	24.7±89.2
3	2	0.07±0.09	0.13±0.11	1.38±0.22	1.38±0.13	47.4±60.5	33.2±88.4
4	1	0.13±0.07	0.20±0.05	1.27±0.18	1.18±0.07	15.8±23.8	8.8±4.2
4	2	0.10±0.08	0.14±0.06	1.32±0.17	1.32±0.02	23.5±35.0	11.6±7.2
5	1	0.08±0.08	0.15±0.06	1.41±0.29	1.35±0.21	35.0±72.2	12.3±13.1
5	2	0.10±0.13	0.17±0.08	1.33±0.29	1.32±0.04	33.4±57.8	7.2±5.8
Mean		**0.094±0.078**	**0.153*±0.066**	**1.38±0.23**	**1.34±0.13***	**29.1±44.5**	**16.2*±25.9**

*Table 9.1 LSQ and BSP IVIM parameters across all volunteers. *significance for LSQ vs BSP ($p<0.05$).*

9.4 Discussion

Second-order motion-compensated diffusion-weighted imaging in combination with Bayesian shrinkage prior inference allows to map the perfusion fraction of the human heart during systolic contraction. Imaging in systole reduces partial volume effects due to a more favorable ratio of voxel size to myocardial thickness when compared to imaging in diastole. In addition, systolic time points are more reproducible in the presence of heart rate variations thereby improving the consistency of the data. In combination with Bayesian processing, perfusion maps with reduced noise are obtained when compared to standard segmented least squares fitting.

9.5 Conclusion

Bayesian Intravoxel Incoherent Motion mapping is considered a promising approach to map myocardial perfusion fractions without the need for contrast agent administration. Further work is warranted to study local perfusion changes during both rest and pharmacologically induced stress in ischemic patients.

Chapter 10

Discussion and Outlook

10.1 Discussion

In this work, two sequence designs for *in vivo* cardiac DTI, the Stimulated Echo Acquisition Mode (STEAM) and Spin Echo (SE) imaging, have been implemented, validated and applied to study left ventricular tissue properties in healthy and diseased hearts. It has been demonstrated, that under *in vivo* conditions, SE based diffusion imaging using second-order motion-compensated diffusion gradients yields a 2.3-2.9 increase in SNR efficiency relative to STEAM. This SNR gain translates into improved accuracy of diffusion tensor metrics. For multi-slice imaging, SNR can be further increased by a slice-interleaved acquisition scheme with reduced signal saturation due to longer TR. As the SE approach requires one R-R interval to acquire one diffusion-weighted image (in contrast to two R-R-intervals for STEAM), an increase in scan efficiency during free-breathing acquisition of 30% relative to STEAM could be demonstrated (244). Statistically significant differences for mean diffusivity (MD) and fractional anisotropy (FA) were found between both sequences *in vivo*. These observations could be explained by motional narrowing effects due to different diffusion encoding times of SE (~25ms) versus STEAM (~1000ms), however further investigations on this discrepancy of apparent tissue property are warranted.

The STEAM technique was subsequently employed to study dynamic fibre reorientation between heart phases in patients with dilated cardiomyopathy (DCM). Elevation of myofibre helix angles was observed during contraction in the control group of healthy volunteers, which is assumed to generate myocardial twist and optimize cardiac pumping efficiency. In addition, a tendency towards a more radial sheetlet orientation in systole was identified based on the secondary eigenvector component, while diastolic data showed a more longitudinal sheetlet orientation relative to the short-axis normal. In contrast, helix and sheetlet angles in the DCM patients did not change significantly between heart phases and diastolic fibre orientations were more longitudinal compared to healthy controls. In particular, a subgroup of DCM patients with low ejection fraction (EF: 15-35%) showed remarkably increased helix angles compared to patients with higher EF and the controls. The reduced dynamic fibre reorientation between cardiac phases was accompanied by reduced cardiac strain rates and torsion. These findings provide new insights into structural alterations in the living heart in DCM.

The intrinsic low scan efficiency of cardiac DTI has been addressed by simultaneous multi-slice imaging. A dual-band excitation pulse and a dedicated parallel image reconstruction were implemented and applied to STEAM based diffusion imaging. A scan acceleration factor of two relative to conventional sequential single-slice imaging has been shown. No statistically significant differences were found between accelerated and non-accelerated DTI results. An extension of the approach to more than two concurrently excited slices was demonstrated recently (227). Successful image reconstruction requires dedicated surface coil arrays to provide sufficient coil sensitivity variation. Furthermore B_0 homogeneity needs to be guaranteed over a larger volume as compared to single slice acquisition. Potential image distortions due to off-resonance effects, however, can be addressed by dedicated post-processing methods incorporating B_0 field maps as shown in Chapter 4.1.1.

The contribution of microvascular perfusion to the diffusion-weighted signal at low b-values was investigated in a model of myocardial infarction in pigs. As proposed by the Intravoxel Incoherent Motion (IVIM) theory, a bi-exponential signal decay model allows to accurately fit the *in vivo* data. Low perfusion fractions were found in the infarcted area and the absence of perfusion post mortem was correctly described. Importantly, no statistically significant differences were found between *in vivo* and post mortem diffusion components which attest a sufficient insensitivity to bulk motion of the SE sequence. The statistical power of this study, however, was limited by the relatively small number of subjects (N=5).

The inherent sensitivity to low SNR in IVIM parameter estimation has been addressed by using Bayesian inference for parameter mapping. The proposed technique allows a reduction in parameter variation compared to least squares regression. Future work should investigate potential data reduction to shorten current measurement times to clinically acceptable durations. Particularly in case of renal insufficiency, IVIM is an appealing method to map myocardial perfusion without contrast agent administration.

10.2 Outlook

With recent developments in magnetic resonance hardware, sufficiently short echo times (TE<70ms) for higher-order motion-compensated SE (34,35) can be realised. Improvements in gradient hardware performance allow a considerable reduction in TE, as the b-value has a quadratic gradient strength dependency (eq. 3.18). The feasibility to design gradient hardware delivering 300mT/m at a slew rate of 200mT/m/ms has been shown in the Human Connectome Project (245). While the Connectome gradient system requires dedicated gradient amplifiers and hence considerable cost is added to MRI system installation and maintenance, geometric scaling of gradient coils may be pursued as an alternative option in the future. To this end, a reduction of gradient coil diameter from 70 to 60cm would provide an increase in gradient performance from 40 to 90mT/m with standard gradient amplifiers. At these high gradient amplitudes, mechanical gradient oscillations and eddy currents induced by gradient coil activity need to be addressed. Consequently, magnetic field monitoring as described in Chapter 4.1. should be used alongside advanced image reconstruction approaches to correct for system imperfections produced by these systems.

Another fundamental consideration relates to baseline SNR and, accordingly, to static magnetic field strength. A 1.5T system was used for most of the work described in the present thesis. Higher static field strengths allow to elevate baseline SNR but dedicated measures to counteract increased B_0 inhomogeneity need to be fully implemented as outlined in Chapter 4.1.

The SNR gain may be utilised to increase spatial resolution and hence reduce partial voluming of current DTI protocols. Performing *in vivo* imaging with voxel sizes smaller than 1.9x1.9mm^2 (246) should be approached. In addition, higher angular resolution including Q-Ball imaging (105) or model-free diffusion spectrum imaging (102) are potential objectives for future work.

Current whole heart 3D fibre reconstructions are based on multi-slice two-dimensional data acquisitions and optional data extrapolation methods (154). Three-dimensional data acquisition with segmented multi-shot readouts may be performed if motion induced phases inconsistencies between k-space segments are adequately addressed. This can be achieved by higher-order motion-compensated diffusion encoding gradients (34,35) in combination with phase navigators (247). Alternatively, Nguyen et al. (36) proposed a diffusion-weighted preparation sequence which can be combined with multi-shot 3D image readouts (Cartesian, Spiral). The feasibility of 3D multi-shot diffusion-weighted imaging has been shown for carotid vessel wall imaging (248) with sub-millimetre resolution. With the MUSE ("multiplexed sensitivity-encoding") (128) approach, phase errors in interleaved diffusion-weighted images are measured and corrected for during image reconstruction. All multi-shot approaches circumvent the downsides of single-shot EPI (Chapter 4.1) translating to improved spatial resolution and reduced off-resonance sensitivity. Future work should explore 3D multi-shot acquisition for cardiac DTI as an alternative to the established 2D single-shot EPI readout.

In a number of studies on diseased hearts, cardiac DTI has been able to detect myofibre reorientation, myocardial degeneration and accumulation of fibrosis - potential hallmarks of heart failure (27–32). Hence, *in vivo* cardiac diffusion-weighted imaging has the potential to extend current diagnostic tools to characterise and assess myocardial tissue structure and integrity. The technique is expected to play an important role in monitoring and guiding a range of therapeutic approaches. In particular, longitudinal studies of regenerative treatment strategies are foreseen as a promising avenue. Moreover, personalisation of data-driven *in silico* models of the heart to gain mechanistic insights are important targets.

In particular, patient-specific microstructural information may allow enhancing models simulating disease progression and potential treatment responses prior to intervention in the patient (172,249). Possible applications of predictive modelling also include radio-frequency ablation and cardiac resynchronisation therapy (250–253).

Abbreviations

ADC	Apparent Diffusion Coefficient
BPM	Beats Per Minute
BW	Bandwidth
CVD	Cardiovascular Disease
b100	Image with b-value of 100s/mm^2
B_0	Main magnetic field
B_1	RF excitation field
BSA	Body Surface Area
CSPAMM	Complementary Spatial Modulation of Magnetization
DCM	Dilated Cardiomyopathy
DSI	Diffusion Spectrum Imaging
DTI	Diffusion Tensor Imaging
DWI	Diffusion Weighted Imaging
ECG	Electrocardiography
ECV	Extra Cellular Volume
EDV	End Diastolic Volume
ESV	End Systolic Volume
EF	Ejection Fraction
EPI	Echo Planar Imaging
FA	Fractional Anisotropy
FID	Free Induction Decay
FOV	Field Of View
Gd	Gadolinium
HA	Helix Angle
HCM	Hypertrophic Cardiomyopathy
HR	Heart Rate
IVIM	Intravoxel Incoherent Motion
LGE	Late Gadolinium Enhancement

LV	Left Ventricle
M	Measurement encoding direction
MD	Mean Diffusivity
MI	Myocardial Infarction
MRI	Magnetic Resonance Imaging
NMR	Nuclear Magnetic Resonance
ODF	Orientation Distribution Function
P	Phase encoding direction
p	Statistics: value of significance
PCA	Principal Component Analysis
PDF	Probability Density Function
QSI	Q-Space Imaging
RF	Radio Frequency
RV	Right Ventricle
S	Slice encoding direction
SD	Standard Deviation
SE	Spin Echo
SS	Single-Shot
SINMOD	Sine Wave Modeling
SNR	Signal-to-Noise Ratio
STEAM	Stimulated Echo Acquisition Mode
TA	Transverse Angle
TE	Echo Time
TM	Mixing Time
TMIP	Temporal Maximum Intensity Projection
TR	Repetition Time

Bibliography

1. Mendis S, Pekka P, Norrving B. Global Atlas on cardiovascular disease prevention and control. Organization 2011:156.

2. WHO. The top 10 causes of death. 2012.

3. Dayer M, Cowie MR. Heart failure: Diagnosis and healthcare burden. Clin. Med. (Northfield. Il). 2004;4:13–18.

4. Mcmurray JJ V, Adamopoulos S, Anker SD, et al. ESC Guidelines for the diagnosis and treatment of acute and chronic heart failure 2012. Eur. J. Heart Fail. 2012;14:803–869.

5. Chambers J. Echocardiography in Clinical Practice. 2002.

6. Moon JC, Messroghli DR, Kellman P, et al. Myocardial T1 mapping and extracellular volume quantification: a Society for Cardiovascular Magnetic Resonance (SCMR) and CMR Working Group of the European Society of Cardiology consensus statement. J. Cardiovasc. Magn. Reson. 2013;15:1.

7. Kellman P, Wilson JR, Xue H, Ugander M, Arai AE. Extracellular volume fraction mapping in the myocardium, part 1: evaluation of an automated method. J. Cardiovasc. Magn. Reson. 2012;14:64.

8. Foley RN. Clinical epidemiology of cardiovascular disease in chronic kidney disease. J. Ren. Care 2010;36:4–8.

9. Kali A, Cokic I, Tang RLQ, Yang H-J, Sharif B, Marbán E, Li D, Berman DS, Dharmakumar R. Determination of location, size, and transmurality of chronic myocardial infarction without exogenous contrast media by using cardiac magnetic resonance imaging at 3 T. Circ. Cardiovasc. Imaging 2014;7:471–81.

10. Kali A, Cokic I, Tang R, Yang H-J, Sharif B, Marbán E, Li D, Berman DS, Dharmakumar R. Contrast-free T1 mapping at 3T can characterize chronic myocardial infarctions with high diagnostic accuracy. J. Cardiovasc. Magn. Reson. 2014;16:P205.

11. Van Oorschot JW, El Aidi H, Jansen Of Lorkeers SJ, et al. Endogenous assessment of chronic myocardial infarction with T1ρ-mapping in patients. J. Cardiovasc. Magn. Reson. 2014;16:104.

12. Witschey WR, Zsido G a, Koomalsingh K, et al. In vivo chronic myocardial infarction characterization by spin locked cardiovascular magnetic resonance. J. Cardiovasc. Magn. Reson. 2012;14:37.

13. Spiewak M, Malek L a., Misko J, Chojnowska L, Milosz B, Klopotowski M, Petryka J, Dabrowski M, Kepka C, Ruzyllo W. Comparison of different quantification methods of late gadolinium enhancement in patients with hypertrophic cardiomyopathy. Eur. J. Radiol. 2010;74:e149–e153.

14. Schulz-Menger J. Myocardial edema in acute ischemic injury. JACC Cardiovasc. Imaging 2011;4:279–281.

15. Xia R, Lu X, Zhang B, Wang Y, Liao J, Zheng J, Gao F. Early reperfusion can reduce infarction size but not salvaged myocardial size in acute myocardial infarction rats. JACC Cardiovasc. Imaging 2015;8:616–617.

16. Nguyen CT, Lu M, Bi X, Kellman P, Li D, Zhao S. In vivo diffusion-weighted MRI detection of myocardial fibrosis in hypertrophic cardiomyopathy patients. J. Cardiovasc. Magn. Reson. 2015;17:P34.

17. Abdullah OM, Drakos SG, Diakos N a, et al. Characterization of diffuse fibrosis in the failing human heart via diffusion tensor imaging and quantitative histological validation. NMR Biomed. 2014;27:1378–86.

18. Wu MT, Tseng WY, Su MY, Liu CP, Chiou KR, Wedeen VJ, Reese TG, Yang CF. Diffusion tensor magnetic resonance imaging mapping the fiber architecture remodeling in human myocardium after infarction: correlation with viability and wall motion. Circulation 2006;114:1036–1045.

19. Pop M, Ghugre NR, Ramanan V, Morikawa L, Stanisz G, Dick AJ, Wright G a. Quantification of fibrosis in infarcted swine hearts by ex vivo late gadolinium-enhancement and diffusion-weighted MRI methods. Phys. Med. Biol. 2013;58:5009–28.

20. Edelman RR, Gaa J, Wedeen VJ, Loh E, Hare JM, Prasad P, Li W. In vivo measurement of water diffusion in the human heart. Magn Reson Med 1994;32:423–428.

21. Stejskal EO, Tanner JE. Spin diffusion measurements: spin echoes in the presence of a time-dependant field gradient. J. Chem. Phys. 1965;42:5.

22. Scollan DF, Holmes A, Winslow R, Forder J. Histological validation of myocardial microstructure obtained from diffusion tensor magnetic resonance imaging. Am J Physiol 1998;275:H2308–18.

23. Sosnovik DE, Mekkaoui C, Huang S, et al. Microstructural impact of ischemia and bone marrow-derived cell therapy revealed with diffusion tensor magnetic resonance imaging tractography of the heart in vivo. Circulation 2014;129:1731–1741.

24. Hsu EW, Muzikant AL, Matulevicius SA, Penland RC, Henriquez CS. Magnetic resonance myocardial fiber-orientation mapping with direct histological correlation. Am J Physiol 1998;274:H1627–34.

25. Kung GL, Nguyen TC, Itoh A, Skare S, Ingels Jr. NB, Miller DC, Ennis DB. The presence of two local myocardial sheet populations confirmed by diffusion tensor MRI and histological validation. J Magn Reson Imaging 2011;34:1080–1091.

26. Geerts L, Bovendeerd P, Nicolay K, Arts T. Characterization of the normal cardiac myofiber field in goat measured with MR-diffusion tensor imaging. Am J Physiol Hear. Circ Physiol 2002;283:H139–45.

27. Li W, Lu M, Banerjee S, Zhong J, Ye A, Molter J, Yu X. Ex vivo diffusion tensor MRI reflects microscopic structural remodeling associated with aging and disease progression in normal and cardiomyopathic Syrian hamsters. NMR Biomed. 2009;22:819–25.

28. Helm P a., Younes L, Beg MF, Ennis DB, Leclercq C, Faris OP, McVeigh E, Kass D, Miller MI, Winslow RL. Evidence of structural remodeling in the dyssynchronous failing heart. Circ. Res. 2006;98:125–132.

29. McGill LA, Ismail TF, Nielles-Vallespin S, et al. Reproducibility of in-vivo diffusion tensor cardiovascular magnetic resonance in hypertrophic cardiomyopathy. J Cardiovasc Magn Reson 2012;14:86.

30. Ferreira P, Kilner PJ, McGill L-A, et al. In vivo cardiovascular magnetic resonance diffusion tensor imaging shows evidence of abnormal myocardial laminar orientations and mobility in hypertrophic cardiomyopathy. J. Cardiovasc. Magn. Reson. 2014;16:P338.

31. Wu M-T, Su M-YM, Huang Y-L, Chiou K-R, Yang P, Pan H-B, Reese TG, Wedeen VJ, Tseng W-YI. Sequential changes of myocardial microstructure in patients postmyocardial infarction by diffusion-

tensor cardiac MR: correlation with left ventricular structure and function. Circ. Cardiovasc. Imaging 2009;2:32–40, 6 p following 40.

32. Wu Y, Tse HF, Wu EX. Diffusion tensor MRI study of myocardium structural remodeling after infarction in porcine model. Conf Proc IEEE Eng Med Biol Soc 2006;1:1069–1072.

33. Gamper U, Boesiger P, Kozerke S. Diffusion imaging of the in vivo heart using spin echoes--considerations on bulk motion sensitivity. Magn Reson Med 2007;57:331–337.

34. Stoeck CT, von Deuster C, Genet M, Atkinson D, Kozerke S. Second Order Motion Compensated Spin-Echo Diffusion Tensor Imaging of the Human Heart. Magn Reson Med 2015. doi: 10.1002/mrm.25784.

35. Welsh C, Di Bella E, Hsu E. Higher-Order Motion-Compensation for In Vivo Cardiac Diffusion Tensor Imaging in Rats. IEEE Trans Med Imaging 2015. doi: 10.1109/TMI.2015.2411571.

36. Nguyen C, Fan Z, Sharif B, He Y, Dharmakumar R, Berman DS, Li D. In vivo three-dimensional high resolution cardiac diffusion-weighted MRI: A motion compensated diffusion-prepared balanced steady-state free precession approach. Magn. Reson. Med. 2014;72:1257–1267.

37. Nielles-Vallespin S, Mekkaoui C, Gatehouse P, Reese TG, Keegan J, Ferreira PF, Collins S, Speier P, Feiweier T, Silva R. In vivo diffusion tensor MRI of the human heart: Reproducibility of breath-hold and navigator-based approaches. Magn. Reson. Med. 2013;70:454–465.

38. Stoeck CT, Kalinowska A, von Deuster C, et al. Dual-phase cardiac diffusion tensor imaging with strain correction. PLoS One 2014;9:e107159.

39. Tseng WY, Reese TG, Weisskoff RM, Wedeen VJ. Cardiac diffusion tensor MRI in vivo without strain correction. Magn Reson Med 1999;42:393–403.

40. Pai VM, Rapacchi S, Kellman P, Croisille P, Wen H. PCATMIP: enhancing signal intensity in diffusion-weighted magnetic resonance imaging. Magn Reson Med 2011;65:1611–1619.

41. Le Bihan D. Diffusion and Perfusion Magnetic Resonance Imaging. Raven Press; 1995.

42. Anderson RH, Ho SY, Redmann K, Sanchez-Quintana D, Lunkenheimer PP. The anatomical arrangement of the myocardial cells making up the ventricular mass. Eur. J. Cardio-Thoracic Surg. 2005;28:517–525.

43. Sonnenblick EH, Ross J, Covell JW, Spotnitz HM, Spiro D. The Ultrastructure of the Heart in Systole and Diastole. Changes In Sarcomere Length. Circ. Res. 1967;21:423–431.

44. Spotnitz HM, Spotnitz WD, Cottrell TS, Spiro D, Sonnenblick EH. Cellular basis for volume related wall thickness changes in the rat left ventricle. J Mol Cell Cardiol 1974;6:317–331.

45. Greenbaum RA, Ho SY, Gibson DG, Becker AE, Anderson RH. Left ventricular fibre architecture in man. Br Hear. J 1981;45:248–263.

46. Streeter Jr. DD, Spotnitz HM, Patel DP, Ross Jr. J, Sonnenblick EH. Fiber orientation in the canine left ventricle during diastole and systole. Circ Res 1969;24:339–347.

47. Mekkaoui C, Huang S, Chen HH, et al. Fiber architecture in remodeled myocardium revealed with a quantitative diffusion CMR tractography framework and histological validation. J Cardiovasc Magn Reson 2012;14:70.

48. Sosnovik DE, Wang R, Dai G, Wang T, Aikawa E, Novikov M, Rosenzweig A, Gilbert RJ, Wedeen VJ. Diffusion spectrum MRI tractography reveals the presence of a complex network of residual myofibers in infarcted myocardium. Circ. Cardiovasc. Imaging 2009;2:206–12.

49. Tseng WY, Wedeen VJ, Reese TG, Smith RN, Halpern EF. Diffusion tensor MRI of myocardial fibers and sheets: correspondence with visible cut-face texture. J Magn Reson Imaging 2003;17:31–42.

50. Strijkers GJ, Bouts A, Blankesteijn WM, Peeters THJM, Vilanova A, van Prooijen MC, Sanders HMHF, Heijman E, Nicolay K. Diffusion tensor imaging of left ventricular remodeling in response to myocardial infarction in the mouse. NMR Biomed. 2009;22:182–90.

51. Chen J, Song SK, Liu W, McLean M, Allen JS, Tan J, Wickline SA, Yu X. Remodeling of cardiac fiber structure after infarction in rats quantified with diffusion tensor MRI. Am J Physiol Hear. Circ Physiol 2003;285:H946–54.

52. Holmes JW, Takayama Y, LeGrice I, Covell JW. Depressed regional deformation near anterior papillary muscle. Am J Physiol 1995;269:H262–70.

53. Smerup M, Agger P, Nielsen EA, Ringgaard S, Pedersen M, Niederer P, Anderson RH, Lunkenheimer PP. Regional and epi- to endocardial differences in transmural angles of left ventricular cardiomyocytes measured in ex vivo pig hearts: functional implications. Anat Rec 2013;296:1724–1734.

54. Wu EX, Wu Y, Nicholls JM, Wang J, Liao S, Zhu S, Lau CP, Tse HF. MR diffusion tensor imaging study of postinfarct myocardium structural remodeling in a porcine model. Magn Reson Med 2007;58:687–695.

55. Lombaert H, Peyrat JM, Croisille P, Rapacchi S, Fanton L, Cheriet F, Clarysse P, Magnin I, Delingette H, Ayache N. Human atlas of the cardiac fiber architecture: study on a healthy population. IEEE Trans Med Imaging 2012;31:1436–1447.

56. Wei H, Viallon M, Delattre B, Moulin K, Yang F, Croisille P, Zhu Y. Free-Breathing Diffusion Tensor Imaging and Tractography of the Human Heart in Healthy Volunteers Using Wavelet-Based Image Fusion. IEEE Trans Med Imaging 2015;34:306–316.

57. Tezuka F. Muscle fiber orientation in normal and hypertrophied hearts. Tohoku J. Exp. Med. 1975;948025:289–297.

58. Lombaert H, Peyrat JM. Joint statistics on cardiac shape and fiber architecture. Med Image Comput Comput Assist Interv 2013;16:492–500.

59. Helm P, Beg MF, Miller MI, Winslow RL. Measuring and mapping cardiac fiber and laminar architecture using diffusion tensor MR imaging. Ann N Y Acad Sci 2005;1047:296–307.

60. Gerdes AM, Moore JA, Hines JM, Kirkland PA, Bishop SP. Regional differences in myocyte size in normal rat heart. Anat Rec 1986;215:420–426.

61. LeGrice IJ, Smaill BH, Chai LZ, Edgar SG, Gavin JB, Hunter PJ. Laminar structure of the heart: ventricular myocyte arrangement and connective tissue architecture in the dog. Am J Physiol 1995;269:H571–82.

62. Hales PW, Schneider JE, Burton RA, Wright BJ, Bollensdorff C, Kohl P. Histo-anatomical structure of the living isolated rat heart in two contraction states assessed by diffusion tensor MRI. Prog Biophys Mol Biol 2012;110:319–330.

63. Pope AJ, Sands GB, Smaill BH, LeGrice IJ. Three-dimensional transmural organization of perimysial collagen in the heart. Am J Physiol Hear. Circ Physiol 2008;295:H1243–H1252.

64. Gilbert SH, Benson AP, Li P, V. Holden A. Visualisation of Dog Myocardial Structure from Diffusion Tensor Magnetic Resonance Imaging: The Paradox of Uniformity and Variability. FIMH 2007 2007:403–412.

65. Harrington KB, Rodriguez F, Cheng A, Langer F, Ashikaga H, Daughters GT, Criscione JC, Ingels NB, Miller DC. Direct measurement of transmural laminar architecture in the anterolateral wall of the ovine left ventricle: new implications for wall thickening mechanics. Am. J. Physiol. Heart Circ. Physiol. 2005;288:H1324–30.

66. Helm PA, Tseng H, Younes L, McVeigh ER, Winslow RL. Ex vivo 3D diffusion tensor imaging and quantification of cardiac laminar structure. Magn. Reson. Med. 2005;54:850–859.

67. Mekkaoui C, Porayette P, Jackowski MP, Kostis WJ, Dai G, Sanders S, Sosnovik DE. Diffusion MRI tractography of the developing human fetal heart. PLoS One 2013;8:e72795.

68. Tobita K, Garrison JB, Liu LJ, Tinney JP, Keller BB. Three-dimensional myofiber architecture of the embryonic left ventricle during normal development and altered mechanical loads. Anat. Rec. - Part A Discov. Mol. Cell. Evol. Biol. 2005;283:193–201.

69. Jeung M-Y, Germain P, Croisille P, Ghannudi S El, Roy C, Gangi A. Myocardial Tagging with MR Imaging: Overview of Normal and Pathologic Findings. RadioGraphics 2012;32:1381–1398.

70. Pflugfelder PW, Higgins B. Systolic Wall Thickening Was 43% ± 31%.

71. Sandstede J, Lipke C, Beer M, Hofmann S, Pabst T, Kenn W, Neubauer S, Hahn D. Age- and gender-specific differences in left and right ventricular cardiac function and mass determined by cine magnetic resonance imaging. Eur. Radiol. 2000;10:438–442. doi: 10.1007/s003300050072.

72. LeGrice IJ, Takayama Y, Covell JW. Transverse shear along myocardial cleavage planes provides a mechanism for normal systolic wall thickening. Circ Res 1995;77:182–193.

73. Dou J, Tseng WYI, Reese TG, Wedeen VJ. Combined diffusion and strain MRI reveals structure and function of human myocardial laminar sheets in vivo. Magn. Reson. Med. 2003;50:107–113.

74. Cheng YJ, Lang D, Caruthers SD, Efimov IR, Chen J, Wickline SA. Focal but reversible diastolic sheet dysfunction reflects regional calcium mishandling in dystrophic mdx mouse hearts. Am J Physiol Hear. Circ Physiol 2012;303:H559–68.

75. Stuber M, Scheidegger M, Fischer SE, Nagel E, Steinemann F, Hess O, Boesiger P. Alterations in the local myocardial motion pattern in patients suffering from pressure overload due to aortic stenosis. Circ Res 1999;100:361–8.

76. Smerup M, Partridge J, Agger P, Ringgaard S, Pedersen M, Petersen S, Hasenkam JM, Niederer P, Lunkenheimer PP, Anderson RH. A mathematical model of the mechanical link between shortening of the cardiomyocytes and systolic deformation of the left ventricular myocardium. Technol. Heal. Care 2013;21:63–79.

77. Taber L a., Yang M, Podszus WW. Mechanics of ventricular torsion. J. Biomech. 1996;29:745–752.

78. Maceiraa A, Prasada S, Khanb M, Pennella D. Normalized Left Ventricular Systolic and Diastolic Function by Steady State Free Precession Cardiovascular Magnetic Resonance. J. Cardiovasc. Magn. Reson. 2006;8:417–426.

79. Dou J, Reese TG, Tseng WY, Wedeen VJ. Cardiac diffusion MRI without motion effects. Magn Reson Med 2002;48:105–114.

80. Chen J, Liu W, Zhang H. Regional ventricular wall thickening reflects changes in cardiac fiber and sheet structure during contraction: quantification with diffusion tensor MRI. Am. J. Physiol. Hear. Circ. Physiol. 2005;289:1898–1907.

81. McGill L-A, Ferreira P, Scott AD, Nielles-Vallespin S, Silva R, Kilner PJ, Firmin D, Pennell D. Comparison of cardiac DTI parameters between systole and diastole. J. Cardiovasc. Magn. Reson. 2014;16:P39.

82. Ashikaga H, Criscione JC, Omens JH, Covell JW, Ingels NB. Transmural left ventricular mechanics underlying torsional recoil during relaxation. Am. J. Physiol. Heart Circ. Physiol. 2004;286:H640–7. doi: 10.1152/ajpheart.00575.2003.

83. Sano T, Takayama N, Shimamoto T. Directional difference of conduction velocity in the cardiac ventricular syncytium studied by microelectrodes. Circ Res 1959;7:262–267.

84. Mekkaoui C, Jackowski MP, Stoeck CT, Thiagalingam A, Kostis WJ, Ruskin JN, Reese TG, Kozerke S, Sosnovik DE. Detection of Infarcted and Arrhythmogenic Myocardium with DTI Tractography and Electroanatomical Voltage Mapping. 2014;22:2014.

85. Kanzaki H, Nakatani S, Yamada N, Urayama SI, Miyatake K, Kitakaze M. Impaired Systolic torsion in dilated cardiomyopathy: Reversal of apical rotation at mid-systole characterized with magnetic resonance tagging method. Basic Res. Cardiol. 2006;101:465–470.

86. Kar J, Knutsen AK, Cupps BP, Zhong X, Pasque MK. Three-dimensional regional strain computation method with displacement encoding with stimulated echoes (DENSE) in non-ischemic, non-valvular dilated cardiomyopathy patients and healthy subjects validated by tagged MRI. J. Magn. Reson. Imaging 2014;396:112804.

87. Tseng WY, Dou J, Reese TG, Wedeen VJ. Imaging myocardial fiber disarray and intramural strain hypokinesis in hypertrophic cardiomyopathy with MRI. J Magn Reson Imaging 2006;23:1–8.

88. Gilbert SH, Benson AP, Li P, Holden A V. Regional localisation of left ventricular sheet structure: integration with current models of cardiac fibre, sheet and band structure. Eur. J. Cardiothorac. Surg. 2007;32:231–49.

89. Torrent-Guasp F, Ballester M, Buckberg GD, Carreras F, Flotats A, Carrió I, Ferreira A, Samuels LE, Narula J. Spatial orientation of the ventricular muscle band: Physiologic contribution and surgical implications. J. Thorac. Cardiovasc. Surg. 2001;122:389–392.

90. Dorri F, Niederer PF, Lunkenheimer PP, Anderson RH. The architecture of the left ventricular myocytes relative to left ventricular systolic function. Eur. J. Cardiothorac. Surg. 2010;37:384–92.

91. Fick A. Ueber Diffusion. Ann. Phys. 1855;170:59–86.

92. Einstein A. Ueber die von der molekularkinetischen Theorie der Wärme geforderte Bewegung von in ruhenden Flüssigkeiten suspendierten Teilchen. Ann. Phys. 1905;322:549–560.

93. Carr HY, Purcell EM. Effects of diffusion on free precession in nuclear magnetic resonance experiments. Phys. Rev. 1954;94:630–638.

94. Bloch F. Nuclear induction. Phys. Rev. 1946;70:460–474.

95. Torrey H. Bloch Equations with Diffusion Terms. Phys. Rev. 1956;104:563–565.

96. Basser PJ. Inferring microstructural features and the physiological state of tissues from diffusion-weighted images. NMR Biomed 1995;8:333–344.

97. Jones DK, Horsfield MA, Simmons A. Optimal strategies for measuring diffusion in anisotropic systems by magnetic resonance imaging. Magn Reson Med 1999;42:515–525.

98. Skare S, Hedehus M, Moseley ME, Li TQ. Condition number as a measure of noise performance of diffusion tensor data acquisition schemes with MRI. J. Magn. Reson. 2000;147:340–52.

99. Papadakis N, Xing D, Huang C, Hall L, Carpenter T. A Comparative Study of Acquisition Schemes for Diffusion Tensor Imaging Using MRI. J. Magn. Reson. 1999;137:67–82.

100. Batchelor PG, Atkinson D, Hill DLG, Calamante F, Connelly A. Anisotropic noise propagation in diffusion tensor MRI sampling schemes. Magn. Reson. Med. 2003;49:1143–1151.

101. Ennis DB, Kindlman G, Rodriguez I, Helm PA, McVeigh ER. Visualization of tensor fields using superquadric glyphs. Magn Reson Med 2005;53:169–176.

102. Wedeen VJ, Hagmann P, Tseng W-YI, Reese TG, Weisskoff RM. Mapping complex tissue architecture with diffusion spectrum magnetic resonance imaging. Magn. Reson. Med. 2005;54:1377–1386.

103. Callaghan PT, Eccles CD, Xia Y. NMR microscopy of dynamic displacements: k-space and q-space imaging. J. Phys. E. 2000;21:820–822.

104. Tuch DS, Reese TG, Wiegell MR, Wedeen VJ. Diffusion MRI of Complex Neural Architecture. Neuron 2003;40:885–895.

105. Tuch DS. Q-ball imaging. Magn. Reson. Med. 2004;52:1358–1372.

106. Tournier J-D, Calamante F, Gadian DG, Connelly A. Direct estimation of the fiber orientation density function from diffusion-weighted MRI data using spherical deconvolution. Neuroimage 2004;23:1176–1185.

107. Inglis B a., Bossart EL, Buckley DL, Wirth ED, Mareci TH. Visualization of neural tissue water compartments using biexponential diffusion tensor MRI. Magn. Reson. Med. 2001;45:580–587.

108. Tuch DS, Reese TG, Wiegell MR, Makris N, Belliveau JW, Wedeen VJ. High angular resolution diffusion imaging reveals intravoxel white matter fiber heterogeneity. Magn. Reson. Med. 2002;48:577–582.

109. De Santis S, Assaf Y, Evans CJ, Jones DK. Improved precision in CHARMED assessment of white matter through sampling scheme optimization and model parsimony testing. Magn. Reson. Med. 2014;71:661–671.

110. Assaf Y, Basser PJ. Composite hindered and restricted model of diffusion (CHARMED) MR imaging of the human brain. Neuroimage 2005;27:48–58.

111. Jensen JH, Helpern J a., Ramani A, Lu H, Kaczynski K. Diffusional kurtosis imaging: The quantification of non-gaussian water diffusion by means of magnetic resonance imaging. Magn. Reson. Med. 2005;53:1432–1440.

112. Jensen JH, Chandra R. Weak-Diffusion Theory of NMR Signal in Magnetically Heterogeneous Media. J. Magn. Reson. 1997;126:193–199.

113. Menzel MI, Tan ET, Khare K, Sperl JI, King KF, Tao X, Hardy CJ, Marinelli L. Accelerated diffusion spectrum imaging in the human brain using compressed sensing. Magn Reson Med 2011;66:1226–1233.

114. Mazzoli V, Froeling M, Nederveen AJ, Nicolay K, Strijkers GJ. Cardiac diffusion MRI beyond DTI. In: 22nd Annual Meeting of ISMRM. Milan, Italy; 2014. p. 2560.

115. Le Bihan D, Breton E, Lallemand D, Aubin ML, Vignaud J, Laval-Jeantet M. Separation of diffusion and perfusion in intravoxel incoherent motion MR imaging. Radiology 1988;168:497–505.

116. Le Bihan D. Diffusion and IVIM. Radiology 1988:566–567.

117. Le Bihan D. Diffusion, confusion and functional MRI. Neuroimage 2012;62:1131–1136.

118. Lemke A, Laun FB, Simon D, Stieltjes B, Schad LR. An in vivo verification of the intravoxel incoherent motion effect in diffusion-weighted imaging of the abdomen. Magn. Reson. Med. 2010;64:1580–1585.

119. Moulin K, Croisille P, Feiweier T, Delattre BM a, Wei H, Robert B, Beuf O, Viallon M. In-vivo free-breathing DTI & IVIM of the whole human heart using a real-time slice-followed SE-EPI navigator-based sequence : a reproducibility study in healthy volunteers. Magn Reson Med 2015. doi: 10.1002/mrm.25852.

120. Delattre BM, Viallon M, Wei H, Zhu YM, Feiweier T, Pai VM, Wen H, Croisille P. In vivo cardiac diffusion-weighted magnetic resonance imaging: quantification of normal perfusion and diffusion coefficients with intravoxel incoherent motion imaging. Invest Radiol 2012;47:662–670.

121. Schar M, Kozerke S, Fischer SE, Boesiger P. Cardiac SSFP imaging at 3 Tesla. Magn Reson Med 2004;51:799–806.

122. Jezzard P, Balaban RS. Correction for geometric distortion in echo planar images from B0 field variations. Magn. Reson. Med. 1995;34:65–73.

123. Sutton BP, Noll DC, Fessler J a. Fast, iterative image reconstruction for MRI in the presence of field inhomogeneities. IEEE Trans Med Imagingaging 2003;22:178–188.

124. Harmer J., Chan RW, Stoeck C. ., v. Deuster C, Atkinson D, Kozerke S. Correction of Off-resonance Distortions in In-vivo Cardiac Diffusion Tensor Imaging. In: ISMRM, 2014; Milan, Italy. ; 2014.

125. Pruessmann KP, Weiger M, Scheidegger MB, Boesiger P. SENSE: Sensitivity encoding for fast MRI. Magn. Reson. Med. 1999;42:952–962.

126. Griswold M a., Jakob PM, Heidemann RM, Nittka M, Jellus V, Wang J, Kiefer B, Haase A. Generalized autocalibrating partially parallel acquisitions (GRAPPA). Magn. Reson. Med. 2002;47:1202–1210.

127. Miller KL, Pauly JM. Nonlinear phase correction for navigated diffusion imaging. Magn. Reson. Med. 2003;50:343–353.

128. Chen NK, Guidon A, Chang HC, Song AW. A robust multi-shot scan strategy for high-resolution diffusion weighted MRI enabled by multiplexed sensitivity-encoding (MUSE). Neuroimage 2013;72:41–47.

129. Chan RW, von Deuster C, Giese D, Stoeck CT, Harmer J, Aitken AP, Atkinson D, Kozerke S. Characterization and correction of eddy-current artifacts in unipolar and bipolar diffusion sequences using magnetic field monitoring. J Magn Reson 2014;244:74–84.

130. Mansfield P, Chapman B. Active magnetic screening of coils for static and time-dependent magnetic field generation in NMR imaging. J. Phys. E. 2000;19:540–545.

131. Boesch C, Gruetter R, Martin E. Temporal and spatial analysis of fields generated by eddy currents in superconducting magnets: optimization of corrections and quantitative characterization of magnet/gradient systems. Magn. Reson. Med. 1991;20:268–84.

132. Reese TG, Heid O, Weisskoff RM, Wedeen VJ. Reduction of eddy-current-induced distortion in diffusion MRI using a twice-refocused spin echo. Magn. Reson. Med. 2003;49:177–182.

133. Rapacchi S, Wen H, Viallon M, Grenier D, Kellman P, Croisille P, Pai VM. Low b-value diffusion-weighted cardiac magnetic resonance imaging: initial results in humans using an optimal time-window imaging approach. Invest Radiol 2011;46:751–758.

134. Barmet C, De Zanche N, Pruessmann KP. Spatiotemporal magnetic field monitoring for MR. Magn. Reson. Med. 2008;60:187–197.

135. Wilm BJ, Barmet C, Pavan M, Pruessmann KP. Higher order reconstruction for MRI in the presence of spatiotemporal field perturbations. Magn. Reson. Med. 2011;65:1690–1701.

136. Giese D, Haeberlin M, Barmet C, Pruessmann KP, Schaeffter T, Kozerke S. Analysis and correction of background velocity offsets in phase-contrast flow measurements using magnetic field monitoring. Magn. Reson. Med. 2012;67:1294–1302.

137. Bernstein M a., Zhou XJ, Polzin J a., King KF, Ganin A, Pelc NJ, Glover GH. Concomitant gradient terms in phase contrast MR: Analysis and correction. Magn. Reson. Med. 1998;39:300–308.

138. King KF, Ganin A, Zhou XJ, Bernstein M a. Concomitant gradient field effects in spiral scans. Magn. Reson. Med. 1999;41:103–112.

139. Bernstein M, King K, Zhou X. Handbook of MRI Pulse Sequences. 2004.

140. Stoeck CT, von Deuster C, Toussaint N, Kozerke S. High-resolution single-shot DTI of the in-vivo human heart using asymmetric diffusion encoding. In: 21st Annual Meeting of ISMRM. Salt Lake City, Utah, USA; 2013. p. 480.

141. Meyer CH, Pauly JM, Macovski A, Nishimura DG. Simultaneous spatial and spectral selective excitation. Magn. Reson. Med. 1990;15:287–304.

142. Montant P, Sigovan M, Revel D, Douek P. MR imaging assessment of myocardial edema with T2 mapping. Diagn Interv Imaging 2015.

143. Germain P, El Ghannudi S, Jeung MY, Ohlmann P, Epailly E, Roy C, Gangi A. Native T1 mapping of the heart - a pictorial review. Clin Med Insights Cardiol 2014;8:1–11.

144. Cheng HM, Marie P. 3D Myocardial T 1 Mapping at 3T Using Variable Flip Angle Method : Pilot Study. 2014;829:823–829.

145. Ding H, Fernandez-de-Manuel L, Schär M, Schuleri KH, Halperin H, He L, Muz Zviman M, Beinart R, Herzka D a. Three-dimensional whole-heart T2 mapping at 3T. Magn. Reson. Med. 2014;00:1–14.

146. Von Deuster C, Stoeck CT, Genet M, Atkinson D, Kozerke S. Spin echo versus stimulated echo diffusion tensor imaging of the in vivo human heart. Magn. Reson. Med. 2015;00:n/a–n/a. doi: 10.1002/mrm.25998.

147. Klein S, Staring M, Murphy K, Viergever M a, Pluim JPW. Elastix: a Toolbox for Intensity-Based Medical Image Registration. IEEE Trans. Med. Imaging 2010;29:196–205.

148. Moore CC, Lugo-Olivieri CH, McVeigh ER, Zerhouni E a. Three-dimensional systolic strain patterns in the normal human left ventricle: characterization with tagged MR imaging. Radiology 2000;214:453–66. doi: 10.1148/radiology.214.2.r00fe17453.

149. Kuijer JPA, Marcus JT, Götte MJW, van Rossum AC, Heethaar RM. Three-Dimensional Myocardial Strains at End-Systole and During Diastole in the Left Ventricle of Normal Humans. J. Cardiovasc. Magn. Reson. 2002;4:341–351.

150. Littmann L, Symanski J. Hemodynamic implications of left bundle branch block. Res. Technol. Transf. Comput. Electrocardiol. 2000;33:115–121.

151. Ennis DB, Epstein FH, Kellman P, Fananapazir L, McVeigh ER, Arai AE. Assessment of regional systolic and diastolic dysfunction in familial hypertrophic cardiomyopathy using MR tagging. Magn. Reson. Med. 2003;50:638–642. doi: 10.1002/mrm.10543.

152. Young A a., Dokos S, Powell K a., Sturm B, McCulloch AD, Starling RC, McCarthy PM, White RD. Regional heterogeneity of function in nonischemic dilated cardiomyopathy. Cardiovasc. Res. 2001;49:308–318. doi: 10.1016/S0008-6363(00)00248-0.

153. McKay R, Pfeffer M, Pasternak R, Markis J, Come PC, Nakao S, Alderman JD, Ferguson JJ, Safian RD, Grossmann W. Left ventricular remodeling after myocardial infarction : a corollary to infarct expansion. Circulation 1986;74:693–702. doi: 10.1161/01.CIR.74.4.693.

154. Toussaint N, Stoeck CT, Schaeffter T, Kozerke S, Sermesant M, Batchelor PG. In vivo human cardiac fibre architecture estimation using shape-based diffusion tensor processing. Med. Image Anal. 2013;17:1243–55.

155. Froeling M, Strijkers GJ, Nederveen AJ, Chamuleau S a, Luijten PR. Feasibility of in vivo whole heart DTI and IVIM with a 15 minute acquisition protocol. J. Cardiovasc. Magn. Reson. 2014;16:O15.

156. Wedeen VJ, Weisskoff RM, Poncelet BP. MRI signal void due to in-plane motion is all-or-none. Magn. Reson. Med. 1994;32:116–120.

157. Scott AD, Nielles-Vallespin S, Pennell DJ, Firmin D. Improving the accuracy of cardiac DTI by averaging the complex data. In: 18th Annual SCMR Scientific Sessions. Nice, France; 2015.

158. Toussaint N, Sermesant M, Stoeck CT, Kozerke S, Batchelor PG. In vivo human 3D cardiac fibre architecture: reconstruction using curvilinear interpolation of diffusion tensor images. Med Image Comput Comput Assist Interv 2010;13:418–425.

159. Scott AD, Ferreira PF, Nielles S, Gatehouse P, McGill LA, Kilner P, Pennell DJ, Firmin DN. Optimal diffusion weighting for in vivo cardiac diffusion tensor imaging. Magn Reson Med 2014.

160. McGill L a., Ferreira PF, Scott AD, Nielles-Vallespin S, Giannakidis A, Kilner PJ, Gatehouse PD, de Silva R, Firmin DN, Pennell DJ. Relationship between cardiac diffusion tensor imaging parameters and anthropometrics in healthy volunteers. J. Cardiovasc. Magn. Reson. 2015;18:2.

161. Froeling M, Strijkers G, Nederveen AJ, Chamuleau SA, Luijten PR. Diffusion Tensor MRI of the Heart – In Vivo Imaging of Myocardial Fiber Architecture. Curr. Cardiovasc. Imaging Rep. 2014;7:9276:1–11.

162. Reese TG, Weisskoff RM, Smith RN, Rosen BR, Dinsmore RE, Wedeen VJ. Imaging myocardial fiber architecture in vivo with magnetic resonance. Magn Reson Med 1995;34:786–791.

163. Reese TG, Wedeen VJ, Weisskoff RM. Measuring Diffusion in the Presence of Material Strain. J. Magn. Reson. Ser. B 1996;112:253–258.

164. Cory DG, Garroway a. N. Measurement of translational displacement probabilities by NMR: An indicator of compartmentation. Magn. Reson. Med. 1990;14:435–444.

165. Tseng WY, Reese TG, Weisskoff RM, Brady TJ, Wedeen VJ. Myocardial fiber shortening in humans: initial results of MR imaging. Radiology 2000;216:128–139.

166. Hess AT, Zhong X, Spottiswoode BS, Epstein FH, Meintjes EM. Myocardial 3D strain calculation by combining cine displacement encoding with stimulated echoes (DENSE) and cine strain encoding (SENC) imaging. Magn Reson Med 2009;62:77–84.

167. Wang H, Stoeck C, Kozerke S, Amini A. Analysis of 3D cardiac deformations with 3D SinMod. IEEE EMBS 2013:4386–4389.

168. Lam F, Babacan SD, Haldar JP, Weiner MW, Schuff N, Liang ZP. Denoising diffusion-weighted magnitude MR images using rank and edge constraints. Magn Reson Med 2013. doi: 10.1002/mrm.24728.

169. Myronenko A, Song X. Point set registration: coherent point drift. IEEE Trans Pattern Anal Mach Intell 2010;32:2262–2275.

170. Tseng WI, Reese TG, Weisskoff RM, Wedeen VJ. Cardiac diffusion tensor MRI in vivo without strain correction. Magn. Reson. Med. 1999;42:393–403.

171. Vadakkumpadan F, Arevalo H, Ceritoglu C, Miller M, Trayanova N. Image-based estimation of ventricular fiber orientations for personalized modeling of cardiac electrophysiology. IEEE Trans Med Imaging 2012;31:1051–1060.

172. Lee LC, Genet M, Dang AB, Ge L, Guccione JM, Ratcliffe MB. Applications of computational modeling in cardiac surgery. J. Card. Surg. 2014;29:293–302.

173. Genet M, Lee LC, Nguyen R, Haraldsson H, Acevedo-Bolton G, Zhang Z, Ge L, Ordovas K, Kozerke S, Guccione JM. Distribution of normal human left ventricular myofiber stress at end diastole and end systole: a target for in silico design of heart failure treatments. J. Appl. Physiol. 2014;117:142–52.

174. Young AA, Legrice IJ, Young MA, Smaill BH. Extended confocal microscopy of myocardial laminae and collagen network. J Microsc 1998;192:139–150.

175. Costa KD, Takayama Y, McCulloch AD, Covell JW. Laminar fiber architecture and three-dimensional systolic mechanics in canine ventricular myocardium. Am J Physiol 1999;276:H595–607.

176. Schmid P, Jaermann T, Boesiger P, Niederer PF, Lunkenheimer PP, Cryer CW, Anderson RH. Ventricular myocardial architecture as visualised in postmortem swine hearts using magnetic resonance diffusion tensor imaging. Eur. J. cardio-thoracic Surg. 2005;27:468–472.

177. Wei H, Viallon M, Delattre BM, Wang L, Pai VM, Wen H, Xue H, Guetter C, Croisille P, Zhu Y. Assessment of cardiac motion effects on the fiber architecture of the human heart in vivo. IEEE Trans Med Imaging 2013;32:1928–1938.

178. Stoeck CT, Toussaint N, Boesiger P, Batchelor PG, Kozerke S. Sequence timing optimization in multi-slice diffusion tensor imaging of the beating heart . In: 19th Annual Meeting of ISMRM. Montréal, Canada; 2011. p. 282.

179. Nakamura T, Shibukawa S, Muro I, Kajihara N, Nishio H, Ogini T, Niwa T, Imai Y. Improvement of visualization of cardiac wall in diffusion-weighted imaging using cardiac triggering and acceleration motion correction. In: 22nd Annual Meeting of ISMRM. Milan, Italy; 2014. p. 2417.

180. Nguyen C, Fan Z, Xie Y, Dawkins J, Tseliou E, Bi X, Sharif B, Dharmakumar R, Marbán E, Li D. In vivo contrast free chronic myocardial infarction characterization using diffusion-weighted cardiovascular magnetic resonance. J. Cardiovasc. Magn. Reson. 2014;16:1–10.

181. Cuppen JJM. RLSQ: T1, T2, and ρ calculations, combining ratios and least squares. Magn. Reson. Med. 1987;5:513–524.

182. Reischauer C, Staempfli P, Jaermann T, Boesiger P. Construction of a temperature-controlled diffusion phantom for quality control of diffusion measurements. J Magn Reson Imaging 2009;29:692–698.

183. Callot V, Bennett E, Decking UKM, Balaban RS, Wen H. In vivo study of microcirculation in canine myocardium using the IVIM method. Magn. Reson. Med. 2003;50:531–540.

184. Froeling M, Nederveen AJ, Nicolay K, Strijkers GJ. DTI of human skeletal muscle: the effects of diffusion encoding parameters, signal-to-noise ratio and T2 on tensor indices and fiber tracts. NMR Biomed 2013;26:1339–1352.

185. Feinberg DA, Setsompop K. Ultra-fast MRI of the human brain with simultaneous multi-slice imaging. J Magn Reson 2013;229:90–100.

186. Hargreaves BA, Cunningham CH, Nishimura DG, Conolly SM. Variable-rate selective excitation for rapid MRI sequences. Magn. Reson. Med. 2004;52:590–597.

187. Bland JM, Altman DG. Statistical methods for assessing agreement between two methods of clinical measurement. Lancet 1986;1:307–310.

188. Noehren B, Andersen A, Feiweier T, Damon B, Hardy P. Comparison of twice refocused spin echo versus stimulated echo diffusion tensor imaging for tracking muscle fibers. J Magn Reson Imaging 2015;41:624–632.

189. Froeling M, Mazzoli V. Ex vivo cardiac DTI: on the effects of diffusion time and b-value. In: 17th Annual SCMR Scientific Sessions. Vol. 16. New Orleans; 2014. p. P77.

190. Taylor D, Edwards L, Boucek M, Trulock E, Aurora P, Christie J, Dobbels F, Rahmel A, Keck M, Hertz M. Registry of the International Society for Heart and Lung Transplantation: Twenty-fourth Official Adult Heart Transplant Report—2007. J. Hear. Lung Transplant. 2007;26:769–781.

191. Elliott P, Andersson B, Arbustini E, et al. Classification of the cardiomyopathies: a position statement from the european society of cardiology working group on myocardial and pericardial diseases. Eur. Heart J. 2007;29:270–276.

192. Maron BJ. Contemporary Definitions and Classification of the Cardiomyopathies: An American Heart Association Scientific Statement From the Council on Clinical Cardiology, Heart Failure and Transplantation Committee; Quality of Care and Outcomes Research and Functio. Circulation 2006;113:1807–1816.

193. Kasper EK, Agema WR, Hutchins GM, Deckers JW, Hare JM, Baughman KL. The causes of dilated cardiomyopathy: a clinicopathologic review of 673 consecutive patients. J. Am. Coll. Cardiol. 1994;23:586–590.

194. Unverferth D V, Fetters JK, Unverferth BJ, Leier C V, Magorien RD, Arn AR, Baker PB. Human myocardial histologic characteristics in congestive heart failure. Circulation 1983;68:1194–1200.

195. Wu A, Das S. Sudden death in idiopathic dilated cardiomyopathy. Am Hear. J 1992;124:1035–1045.

196. Tomaselli GF. What Causes Sudden Death in Heart Failure? Circ. Res. 2004;95:754–763.

197. Gerdes a M, Capasso JM. Structural remodeling and mechanical dysfunction of cardiac myocytes in heart failure. J. Mol. Cell. Cardiol. 1995;27:849–856.

198. Packer M. The neurohormonal hypothesis: a theory to explain the mechanism of disease progression in heart failure. J. Am. Coll. Cardiol. 1992:248–254.

199. Hales PW, Burton RA, Bollensdorff C, Mason F, Bishop M, Gavaghan D, Kohl P, Schneider JE. Progressive changes in T(1), T(2) and left-ventricular histo-architecture in the fixed and embedded rat heart. NMR Biomed 2011;24:836–843.

200. Eggen M, Swingen C, Iaizzo P. Ex vivo diffusion tensor MRI of human hearts: Relative effects of specimen decomposition. Magn. Reson. Med. 2012;67:1703–9.

201. Feinberg DA, Hoenninger JC, Crooks LE, Kaufman L, Watts JC, Arakawa M. Inner volume MR imaging: technical concepts and their application. Radiology 1985;156:743–747.

202. Rutz AK, Ryf S, Plein S, Boesiger P, Kozerke S. Accelerated whole-heart 3D CSPAMM for myocardial motion quantification. Magn. Reson. Med. 2008;59:755–63.

203. Nash MP, Hunter PJ. Computational Mechanics of the Heart. J. Elast. 2001;61:113–141.

204. Asner L, Hadjicharalambous M, Chabiniok R, et al. Estimation of passive and active properties in the human heart using 3D tagged MRI. Biomech. Model. Mechanobiol. 2015.

205. Usyk TP, Mazhari R, Mcculloch a. D. Effect of laminar orthotropic myofiber architecture on regional stress and strain in the canine left ventricle. J. Elast. 2000;61:143–164.

206. Codd MB, Sugrue DD, Gersh BJ, Melton LJ. Epidemiology of idiopathic dilated and hypertrophic cardiomyopathy. A population-based study in Olmsted County, Minnesota, 1975-1984. Circulation 1989;80:564–572. doi: 10.1161/01.CIR.80.3.564.

207. Kawel-Boehm N, Maceira A, Valsangiacomo-Buechel ER, Vogel-Claussen J, Turkbey EB, Williams R, Plein S, Tee M, Eng J, Bluemke D a. Normal values for cardiovascular magnetic resonance in adults and children. J. Cardiovasc. Magn. Reson. 2015;17:29. doi: 10.1186/s12968-015-0111-7.

208. Song L-S, Sobie E a, McCulle S, Lederer WJ, Balke CW, Cheng H. Orphaned ryanodine receptors in the failing heart. Proc. Natl. Acad. Sci. U. S. A. 2006;103:4305–10.

209. Louch WE, Mørk HK, Sexton J, Strømme T a, Laake P, Sjaastad I, Sejersted OM. T-tubule disorganization and reduced synchrony of Ca2+ release in murine cardiomyocytes following myocardial infarction. J. Physiol. 2006;574:519–533.

210. Lyon AR, MacLeod KT, Zhang Y, Garcia E, Kanda GK, Lab MJ, Korchev YE, Harding SE, Gorelik J. Loss of T-tubules and other changes to surface topography in ventricular myocytes from failing human and rat heart. Proc. Natl. Acad. Sci. U. S. A. 2009;106:6854–6859.

211. Asner, L Hadjicharalambous, M Chabiniok R, Peressutti D, Sammut E, Wong J, Carr-White G, Lee J, King A, Smith N, Razavi R, Nordsletten D. Patient-specific modeling for left-ventricular mechanics using data-driven boundary energies. Comput. Method Appl. M. 2016;in review.

212. Bonet J, Wood R. Nonlinear continuum mechanics for finite element analysis. Cambridge University Press; 2008.

213. Holzapfel G a, Ogden RW. Constitutive modelling of passive myocardium: a structurally based framework for material characterization. Philos. Trans. A. Math. Phys. Eng. Sci. 2009;367:3445–75. doi: 10.1098/rsta.2009.0091.

214. Kerckhoffs RCP, Bovendeerd PHM, Prinzen FW, Smits K, Arts T. Intra- and interventricular asynchrony of electromechanics in the ventricularly paced heart. J. Eng. Math. 2003;47:201–216. doi: 10.1023/B:ENGI.0000007972.73874.da.

215. Niederer S a., Plank G, Chinchapatnam P, Ginks M, Lamata P, Rhode KS, Rinaldi C a., Razavi R, Smith NP. Length-dependent tension in the failing heart and the efficacy of cardiac resynchronization therapy. Cardiovasc. Res. 2011;89:336–343. doi: 10.1093/cvr/cvq318.

216. Usyk TP, LeGrice IJ, McCulloch AD. Computational model of three-dimensional cardiac electromechanics. Comput. Vis. Sci. 2002;4:249–257. doi: 10.1007/s00791-002-0081-9.

217. Lee J, Cookson A, Roy I, Kerfoot E, Asner L, Vigueras G. Multiphysics Computational Modeling in CHeart. 2016;38:150–178.

218. Paley MNJ, Lee KJ, Wild JM, Griffiths PD, Whitby EH. Simultaneous parallel inclined readout image technique. Magn. Reson. Imaging 2006;24:557–562.

219. Weaver JB. Simultaneous multislice acquisition of MR images. Magn. Reson. Med. 1988;8:275–284.

220. Feinberg D a., Reese TG, Wedeen VJ. Simultaneous echo refocusing in EPI. Magn. Reson. Med. 2002;48:1–5.

221. Reese TG, Benner T, Wang R, Feinberg D a., Van Wedeen J. Halving imaging time of whole brain diffusion spectrum imaging and diffusion tractography using simultaneous image refocusing in EPI. J. Magn. Reson. Imaging 2009;29:517–522.

222. Breuer FA, Blaimer M, Heidemann RM, Mueller MF, Griswold MA, Jakob PM. Controlled aliasing in parallel imaging results in higher acceleration (CAIPIRINHA) for multi-slice imaging. Magn Reson Med 2005;53:684–691.

223. Larkman DJ, Hajnal J V., Herlihy AH, Coutts G a., Young IR, Ehnholm G. Use of multicoil arrays for separation of signal from multiple slices simultaneously excited. J. Magn. Reson. Imaging 2001;13:313–317.

224. Nunes RG, Hajnal J V, Golay X, Larkman DJ. Simultaneous slice excitation and reconstruction for single shot EPI . Proc Intl Soc Mag Reson Med 2006;14:293.

225. Setsompop K, Gagoski BA, Polimeni JR, Witzel T, Wedeen VJ, Wald LL. Blipped-controlled aliasing in parallel imaging for simultaneous multislice echo planar imaging with reduced g-factor penalty. Magn Reson Med 2012;67:1210–1224.

226. Pauly J, Le Roux P, Nishimura D, Macovski A. Parameter relations for the Shinnar-Le Roux selective excitation pulse design algorithm [NMR imaging]. IEEE Trans Med Imaging 1991;10:53–65.

227. Lau AZ, Tunnicliffe EM, Frost R, Koopmans PJ, Tyler DJ, Robson MD. Accelerated human cardiac diffusion tensor imaging using simultaneous multislice imaging. Magn Reson Med 2014. doi: 10.1002/mrm.25200.

228. Von Deuster C, Stoeck CT, Buehrer M, Harmer J, Chan RW, Atkinson D, Kozerke S. Free-breathing cardiac DTI with simultaneous multi-slice excitation. In: 22nd Annual Meeting of ISMRM. Milan, Italy; 2104. p. 2808.

229. Yamada I, Aung W, Himeno Y, Nakagawa T, Shibuya H. Diffusion coefficients in abdominal organs and hepatic lesions: evaluation with intravoxel incoherent motion echo-planar MR imaging. Radiology 1999;210:617–623.

230. Chandarana H, Lee VS, Hecht E, Taouli B SE. Comparison of biexponential and monoexponential model of diffusion weighted imaging in evaluation of renal lesions: preliminary experience. Invest Radiol 2011;46:285–91.

231. Lemke A, Laun FB, Klauss M, Re TJ, Simon D, Delorme S, Schad LR SB. Differentiation of pancreas carcinoma from healthy pancreatic tissue using multiple b-values: comparison of apparent diffusion coefficient and intravoxel incoherent motion derived parameters. Invest Radiol 2009;44:769–75.

232. Luciani A, Vignaud A, Cavet M, NhieuJ T Van, Mallat A, Ruel L, Laurent A, Deux J, Brugieres P, Rahmouni A. Liver Cirrhosis : Intravoxel Incoherent Motion MR Imaging. Radiology 2008;249:891–899.

233. Patel J, Sigmund EE, Rusinek H, Oei M, Babb JS, Taouli B. Diagnosis of cirrhosis with intravoxel incoherent motion diffusion MRI and dynamic contrast-enhanced MRI alone and in combination: Preliminary experience. J. Magn. Reson. Imaging 2010;31:589–600.

234. Deux J-F, Maatouk M, Vignaud A, Luciani A, Lenczner G, Mayer J, Lim P, Dubois-Randé J-L, Kobeiter H, Rahmouni A. Diffusion-weighted echo planar imaging in patients with recent myocardial infarction. Eur. Radiol. 2011;21:46–53.

235. Laissy J-P, Gaxotte V, Pasi N, BenDriss A, Feldman L, Steg PG, Senior, Serfaty J-M. Cardiac diffusion-weighted MR imaging in recent, subacute and chronic myocardial infarction: a pilot study. 2011;13:O46.

236. Reischauer C, Wilm BJ, Froehlich JM, Gutzeit A, Prikler L, Gablinger R, Boesiger P, Wentz KU. High-resolution diffusion tensor imaging of prostate cancer using a reduced FOV technique. Eur J Radiol 2011;80:e34–41.

237. Lemke A, Stieltjes B, Schad LR, Laun FB. Toward an optimal distribution of b values for intravoxel incoherent motion imaging. Magn Reson Imaging 2011;29:766–776.

238. Ogg RJ, Kingsley PB, Taylor JS. WET, a T1- and B1-insensitive water-suppression method for in vivo localized 1H NMR spectroscopy. J Magn Reson B 1994;104:1–10.

239. Plein S, Ryf S, Schwitter J, Radjenovic A, Boesiger P, Kozerke S. Dynamic contrast-enhanced myocardial perfusion MRI accelerated with k-t SENSE. Magn. Reson. Med. 2007;58:777–785.

240. Zhang X, Petersen ET, Ghariq E, De Vis JB, Webb a. G, Teeuwisse WM, Hendrikse J, Van Osch MJP. In vivo blood T1 measurements at 1.5 T, 3 T, and 7 T. Magn. Reson. Med. 2013;70:1082–1086. doi: 10.1002/mrm.24550.

241. Orton MR, Collins DJ, Koh D-M, Leach MO. Improved intravoxel incoherent motion analysis of diffusion weighted imaging by data driven Bayesian modeling. Magn. Reson. Med. 2014;71:411–20.

242. Jeffreys H. An Invariant Form for the Prior Probability in Estimation Problems. Proc. R. Soc. London A Math. Phys. Eng. Sci. 1946;186:453–461.

243. Notohamiprodjo M, Chandarana H, Mikheev A, Rusinek H, Grinstead J, Feiweier T, Raya JG, Lee VS, Sigmund EE. Combined intravoxel incoherent motion and diffusion tensor imaging of renal diffusion and flow anisotropy. Magn. Reson. Med. 2014;00:1–7.

244. Von Deuster C, Stoeck C. ., Genet M, Atkinson D, Kozerke S. Free-breathing Diffusion Tensor Imaging of the In Vivo Human Heart - Stimulated Echo vs. Spin Echo Acquisition. In: Proceedings of the International Society for Magnetic Resonance in Medicine. Singapore; 2016.

245. McNab J a., Edlow BL, Witzel T, et al. The Human Connectome Project and beyond: Initial applications of 300mT/m gradients. Neuroimage 2013;80:234–245.

246. McGill LA, Scott AD, Ferreira PF, et al. Heterogeneity of fractional anisotropy and mean diffusivity measurements by in vivo diffusion tensor imaging in normal human hearts. PLoS One 2015;10:1–17.

247. Liu C, Moseley ME, Bammer R. Simultaneous phase correction and SENSE reconstruction for navigated multi-shot DWI with non-cartesian k-space sampling. Magn. Reson. Med. 2005;54:1412–1422.

248. Xie Y, Yu W, Fan Z, Nguyen C, An J, Zhang Z, Debiao L. High Resolution 3D Diffusion MRI: Detection of lipi-rich necrotic core in plaques without contrast media. 2014;22:2014.

249. Wenk JF, Wall ST, Peterson RC, Helgerson SL, Sabbah HN, Burger M, Stander N, Ratcliffe MB, Guccione JM. A method for automatically optimizing medical devices for treating heart failure: designing polymeric injection patterns. J. Biomech. Eng. 2009;131:121011.

250. Trayanova NA. Computational cardiology: the heart of the matter. ISRN Cardiol 2012:269680. doi: 10.5402/2012/269680.

251. Sermesant M, Chabiniok R, Chinchapatnam P, et al. Patient-specific electromechanical models of the heart for the prediction of pacing acute effects in CRT: a preliminary clinical validation. Med Image Anal 2012;16:201–215.

252. Reumann Gurev, V. and Rice, J. J. M. Computational modeling of cardiac disease: potential for personalized medicine. Per. Med. 2009;6:45–66.

253. Relan J, Chinchapatnam P, Sermesant M, Rhode K, Ginks M, Delingette H, Rinaldi CA, Razavi R, Ayache N. Coupled personalization of cardiac electrophysiology models for prediction of ischaemic ventricular tachycardia. Interface Focus 2011;1:396–407.

List of Publications

Journal Articles

2016 **C. von Deuster**, E. Sammut, C. T. Stoeck, R. Razavi, S. Kozerke
"Mapping Dynamic Myocardial Fibre Reorientation in Dilated Cardiomyopathy using Dual-Phase In-Vivo Cardiac Diffusion Tensor Imaging"
In preparation

2015 **C. von Deuster**, C. T. Stoeck, M. Genet, D. Atkinson, S. Kozerke
"Spin Echo versus Stimulated Echo Diffusion Tensor Imaging of the in vivo Human Heart"
Magn Reson Med., DOI 10.1002/mrm.25998

2015 F. Hennel, M. Buehrer, **C. von Deuster**, A. Seuven, K. P. Pruessmann
"SENSE Reconstruction for Multiband EPI Including Slice-Dependent N/2 Ghost Correction"
Magn Reson Med., DOI 10.1002/mrm.25915

2015 C. T. Stoeck, **C. von Deuster**, M. Genet, D. Atkinson, S. Kozerke
"Second-Order Motion-Compensated Spin Echo Diffusion Tensor Imaging of the Human Heart"
Magn Reson Med., DOI 10.1002/mrm.25784

2015	S. Bosshard, F. Stuker, **C. von Deuster,** A. Schroeter, M. Rudin *“BOLD fMRI of C-fiber Mediated Nociceptive Processing in Mouse Brain in Response to Thermal Stimulation of the Forepaws”* PLoS One. 2015 May 7;10(5):e0126513
2014	R. W. Chan, **C. von Deuster**, C. T. Stoeck, J. Harmer, S. Punwani, N. Ramachandran, S. Kozerke, D. Atkinson *“High-Resolution Diffusion Tensor Imaging (DTI) Of The Human Kidneys Using A Free-Breathing Multi-Slice Targeted-FOV Approach”* NMR Biomed. 2014 Nov;27(11):1300-12
2014	C. T. Stoeck, A. Kalinowska, **C. von Deuster**, J. Harmer, R. W. Chan, M. Niemann, R. Manka, D. Atkinson, D. Sosnovik, C. Mekkaoui, S. Kozerke *“Dual-Phase Cardiac Diffusion Tensor Imaging With Strain Correction”* PLoS One. 2014 Sep 5;9(9):e107159
2014	R. W. Chan, **C. von Deuster**, D. Giese, C. T. Stoeck, J. Harmer, A. P. Aitken, D. Atkinson, S. Kozerke *“Characterization and correction of eddy-current artifacts in unipolar and bipolar diffusion sequences using magnetic field monitoring”* J Magn Reson. 2014 Jul;244:74-84

Conference Abstracts and Proceedings

2016 **C. von Deuster**, C. T. Stoeck, M. Genet, D. Atkinson, S. Kozerke
“Free-breathing Diffusion Tensor Imaging of the In Vivo Human Heart - Stimulated Echo vs. Spin Echo Acquisition”
Proceedings of the 24th Meeting of ISMRM, Singapore, Singapore

2016 **C. von Deuster**, E. Sammut, C. T. Stoeck, R. Razavi, S. Kozerke
“Mapping Dynamic Myocardial Fibre Reorientation in Dilated Cardiomyopathy using Dual-Phase In-Vivo Cardiac Diffusion Tensor Imaging”
Proceedings of the 24th Meeting of ISMRM, Singapore, Singapore

2016 G. Spinner, **C. von Deuster**, C. T. Stoeck, S. Kozerke
“Bayesian Intravoxel Incoherent Motion Imaging to Map Perfusion in the Human Heart”
Proceedings of the 24th Meeting of ISMRM, Singapore, Singapore

2016 C. T. Stoeck, **C. von Deuster**, S. Kozerke
“Second order motion compensated spin echo diffusion tensor imaging of the in vivo human heart – considerations on gradient performance requirements”
Proceedings of the 24th Meeting of ISMRM, Singapore, Singapore

2016 M. Genet, C. T. Stoeck, **C. von Deuster**, L. C. Lee, J. M. Guccione, S. Kozerke
“Finite Element Digital Image Correlation for Cardiac Strain Analysis from 3D Whole-Heart Tagging”
Proceedings of the 24th Meeting of ISMRM, Singapore, Singapore

2016 M. Fuetterer, J. Busch, **C. von Deuster**, C. Binter, N. Cesarovic, M. Lipiski, C. T. Stoeck, S. Kozerke
„Velocity-Selective Tip-Back Excitation for Hyperpolarized [13C] Urea Cardiac Perfusion Imaging“
Proceedings of the 24th Meeting of ISMRM, Singapore, Singapore

2016 C. T. Stoeck, **C. von Deuster**, S. Kozerke
“Second order motion compensated spin echo cardiac DTI at different gradient strengths”
Proceedings of the 19th Meeting of SCMR, Los Angeles, USA

2015 **C. von Deuster**, C. T. Stoeck, M. Genet, D. Atkinson, S. Kozerke
“Comparison of Spin Echo versus Stimulated Echo Diffusion Tensor Imaging of the in vivo Human Heart”
Proceedings of the 32nd Meeting of ESMRMB, Edinburgh, Scotland

2015 **C. von Deuster**, C. T. Stoeck, M. Genet, N. Toussaint, D. Atkinson, S. Kozerke
“A reference dataset of in-vivo human left-ventricular fiber architecture in systole and diastole”
Proceedings of the 18th Meeting of SCMR, Nice, France

2015 **C. von Deuster**, C. T. Stoeck, L. Wissmann, G. Spinner, T. Fleischmann, M. Y. Emmert, N. Cesarovic, S. Kozerke
“Verification of the intra-voxel incoherent motion (IVIM) model in the porcine heart”
Proceedings of the 23rd Meeting of ISMRM, Toronto, Canada

2015 J. Busch, M. Fuetterer, **C. von Deuster**, N. Cesarovic, C. T. Stoeck, S. Kozerke
“Hyperpolarized [1-13C] Pyruvate Metabolic Magnetic Resonance Imaging in Pigs”
Proceedings of the 32nd Meeting of ESMRMB, Edinburgh, Scotland

2015 C. T. Stoeck, **C. von Deuster**, M. Genet, D. Atkinson, S. Kozerke
“First and Second Order Motion Compensated Spin-Echo Diffusion Tensor Imaging of the Human Heart”
Proceedings of the 23rd Meeting of ISMRM, Toronto, Canada

2015 F. Hennel, A. Seuwen, **C. von Deuster**, K. P. Pruessmann
“Ghost-Correcting SENSE Reconstrcution for mutli-band EPI“
Proceedings of the 23rd Meeting of ISMRM, Toronto, Canada

2015 C. T. Stoeck, **C. von Deuster**, M. Genet, D. Atkinson, S. Kozerke
“Second Order Motion Compensated Spin-Echo Diffusion Tensor Imaging of the Human Heart”
Proceedings of the 18th Meeting of SCMR, Nice, France

2015 C. T. Stoeck, **C. von Deuster**, N. Cesarovic, M. Genet, M. Y. Emmert, S. Kozerke
“Direct comparison of in-vivo and post-mortem spin-echo based diffusion tensor imaging in the porcine heart”
Proceedings of the 18th Meeting of SCMR, Nice, France

2014 **C. von Deuster**, C. T. Stoeck, M. Buehrer, J. Harmer, R. W. Chan, D. Atkinson, S. Kozerke
“Free-Breathing Cardiac DTI with Simultaneous Multi-Slice Excitation”
Proceedings of the 22nd Meeting of ISMRM, Milan, Italy

2014 C. T. Stoeck, A. Kalinowska, **C. von Deuster**, J. Harmer, S. Kozerke
“In-Vivo Dual-Phase Cardiac DTI with 3D Strain Correction”
Proceedings of the 22nd Meeting of ISMRM, Milan, Italy

2014 J. Harmer; R. W. Chan, C. T. Stoeck, **C. von Deuster**, D. Atkinson, S. Kozerke
“Correction of Off-Resonance Distortions in In-Vivo Cardiac Diffusion Tensor Imaging”
Proceedings of the 22nd Meeting of ISMRM, Milan, Italy

2014 R. W. Chan, **C. von Deuster**, C. T. Stoeck, J. Harmer, S. Kozerke, D. Atkinson
“High-Resolution Diffusion Tensor Imaging (DTI) of the Human Kidneys Using a Free-Breathing Multi-Slice Targeted-FOV Approach”
Proceedings of the 22nd Meeting of ISMRM, Milan, Italy

2013 **C. von Deuster**, C. T. Stoeck; D. Giese, J. Harmer, R.W. Chan,
D. Atkinson, S. Kozerke
"Concurrent Dual-Slice Cardiac DTI of the in-vivo Human Heart"
Proceedings of the 21st Meeting of ISMRM, Salt Lake City, USA

2013 D. Giese, M. Buehrer, **C. von Deuster**, T. Schaeffter, S. Kozerke
"Multi-Slice Free Breathing Liver Imaging Using a 2D CAIPIRINHA Navigator"
Proceedings of the 21st Meeting of ISMRM, Salt Lake City, USA

2013 R. W. Chan, S. Kozerke, D. Giese, J. Harmer, C. T. Stoeck, **C. von Deuster**, A. Aitken, D. Atkinson
"Characterization and Correction of Eddy-Current Artifacts in Unipolar and Bipolar Diffusion Sequences Using a Field-Monitoring Approach: Application to Renal Diffusion Tensor Imaging (DTI)"
Proceedings of the 21st Meeting of ISMRM, Salt Lake City, USA

2013 C. T. Stoeck, **C. von Deuster**, N. Toussaint, S. Kozerke
"High-Resolution Single-Shot DTI of the in-vivo Human Heart Using Asymmetric Diffusion Encoding"
Proceedings of the 21st Meeting of ISMRM, Salt Lake City, USA

2013 J. Harmer, C. T. Stoeck, R. W. Chan, N. Toussaint, **C. von Deuster**,
D. Atkinson, S. Kozerke
"In-vivo High Resolution Diffusion Tensor Imaging of the Human Heart at 3T: Fat Suppression in the Presence of B0 Field Inhomogeneities"
Proceedings of the 21st Meeting of ISMRM, Salt Lake City, USA

2011 S. C. Bosshard, F. Stuker, **C. von Deuster**, M. Rudin
"TRPV1-mediated entry of QX-314 leads to inhibition of nociceptive input as measured by BOLD fMRI in mice using thermal stimulation"
Proceedings of the 19th Meeting of ISMRM, Montréal, Canada

Acknowledgements

Firstly, I would like to thank Prof. Dr. Sebastian Kozerke for offering me a PhD position to explore the exciting field of cardiac diffusion MRI. I highly appreciated his ideas and continuous guidance during my PhD study. Without his constant support and the great research environment, it would not have been possible to conduct this research. I would like to thank Dr. Claudia Prieto as my second supervisor and Dr. David Atkinson as external supervisor. Thanks to Prof. Dr. Reza Razavi for supporting the joint research collaborations between Zurich and London.

I am very grateful to the referees Prof. Dr. P. Croisille and Prof. Dr. J. Wild for having agreed to review and examine this work.

Thanks to all the friends and colleagues I met during my time at IBT. Thanks to Niklaus, Lukas, Johannes, Julia, Claudio, Christian B., Christian G, Alex F., Alex G., Alex P., Jonas S., Jonas R., Jonas W., Giorgos, Matteo, Simon, Beni, Thomas, Andi, Nicole, Max, Kerem, Patrick, Sophie, Zsofia, Robbert, Adrian, Josip, Vlad, Dian, Martin G., Martin B., Gérard, Rudi and Verena. Thanks to Georg for the joint perfusion project and, of course, many thanks to my diffusion mentor Chris Stoeck.

Thanks to Eva Sammut for applying the DTI work in clinical practice and acquiring the DCM patient data. I also would like to thank David and Liya for the corresponding cardiac modeling. I am grateful for my funding source from the UK (The Engineering and Physical Sciences Research Council - EPSRC) and the repeated financial support by the International Society of Magnetic Resonance in Medicine (ISMRM).

Finally, I would like to express my great gratitude to my family for their unconditional support in all situations and their infinite patience.

Curriculum Vitae

Personal Information

Name	Constantin von Deuster
Date of birth	15 January 1986
Citizenship	German

Education

4/2012 – 3/2016 **PhD Candidate**

Thesis *"Towards Reliable Diffusion MRI of the In Vivo Human Heart"* supervised by Prof. Dr. Sebastian Kozerke and Dr. Claudia Prieto.

Division of Imaging Sciences and Biomedical Engineering, School of Medicine, King's College London, England, Institute for Biomedical Engineering (IBT), ETH and University of Zurich, Switzerland

3/2010 – 4/2012 **M.Sc. in Physics**

Master thesis *"Parallel slice encoding in MR diffusion tensor imaging"* supervised by Prof. Dr. Sebastian Kozerke and Dr. Philip Batchelor.

Division of Imaging Sciences and Biomedical Engineering, School of Medicine, King's College London, England, Institute for Biomedical Engineering (IBT), ETH and University of Zurich, Switzerland

3/2008 – 3/2010 **B.Sc. in Physics**

Swiss Federal Institute of Technology (ETH Zurich), Switzerland

8/2005 – 2/2008	**Undergraduate studies in “Nanostrukturtechnik“** University of Würzburg, Germany
6/2005	**High School** Röntgen-Gymnasium Würzburg, Germany